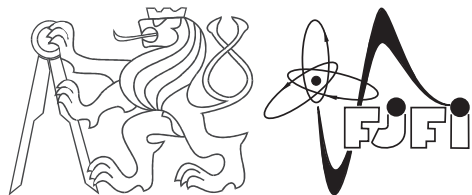


CZECH TECHNICAL UNIVERSITY IN PRAGUE
FACULTY OF NUCLEAR SCIENCES AND PHYSICAL
ENGINEERING
DEPARTMENT OF PHYSICS

Programme: Mathematical Engineering
Branch of Study: Mathematical Physics



High p_T jets in Run II of the ATLAS Experiment

MASTER'S DEGREE PROJECT

Author: Jan Lochman
Supervisor: Ing. Zdeněk Hubáček, Ph.D.
Submitted in: May 2015

Zadani prace

Statement

This thesis is the result of my own work, except where explicit reference is made to the work of others, and has not been submitted for another qualification to this or any other university.

In Prague on
.....

Jan Lochman

Acknowledgment

There are many people to whom I am indebted. First and the most important of these, is my supervisor, Ing. Zdeněk Hubáček, Ph.D. Two years ago, he threw me into the unknown world of particle physics. With his help, I learned not to be frightened from the unknown. He taught me, how to use knowledge, I have obtained at the university, to shed some light into the darkness. With his help, the beautiful world of particle physics has revealed to me.

I deeply appreciate a support from my Faculty, when I was sent after my supervisor at CERN. The leading support, which allowed this to happen, came from Prof. Ing. Igor Jex, DrSc., to whom I would like to thank. It was an astounding feeling, to be part of one of the leading experiments in particle physics, and the satisfaction, when I found out, I can make some contribution to it - indescribable.

Next thanks to my family for their support during my studies.

And thank to You, Flying Spaghetti Monster, for creating such a beautiful Universe, in which the physics reality extends far beyond the frontiers of human imagination, that it is never going to let me relax.

Jan Lochman

Název práce:

Jety s vysokou příčnou hybností v Run II experimentu ATLAS

Autor: Jan Lochman

Obor: Matematické Inženýrství

Druh práce: Diplomová práce

Vedoucí práce: Ing. Zdeněk Hubáček, Ph.D.

CERN

Abstrakt: Diplomová práce se zabývá měřením dvojitého diferenciálního účinného průřezu inkluzivních jetů v p_T a rapiditě v proton-protonových srážkách při $\sqrt{s} = 13 \text{ TeV}$ na detektoru ATLAS. Práce používá data nasimulovaná pomocí Monte Carlo generátoru PYTHIA8 s jety zrekonstruovanými na částicové a detektorové úrovni pomocí anti- k_t jetového algoritmu s parametrem $R = 0,4$. Diferenciální účinný průřez získán z detektorové úrovni je unfoldován na částicovou úroveň a porovnán s partonovou předpovědí získanou z poruchových next-to-leading order výpočtů kvantové chromodynamiky. Jsou použity dvě metody unfoldingu, označené jako simple a 2D, a výsledky z obou metod jsou vzájemně porovnány. Obě metody mohou být použity k unfoldování diferenciálního účinného průřezu inkluzivních jetů měřených v Run II experimentu ATLAS, který by měl začít v létě 2015.

Klíčová slova: Kvantová Chromodynamika, Jety, Unfolding

Title:

High p_T jets in Run II of the ATLAS Experiment

Author: Jan Lochman

Abstract: This thesis deals with the measurement of the inclusive jets double differential cross section in p_T and rapidity in proton-proton collisions at $\sqrt{s} = 13 \text{ TeV}$ with the ATLAS detector. The thesis uses the PYTHIA8 Monte Carlo simulated events and anti- k_t jets with parameter $R = 0.4$ reconstructed at particle and detector level. Differential cross section obtained from the detector level is unfolded to the particle level and compared with the parton level differential cross section prediction of the next-to-leading perturbative Chromodynamics. Two different approaches of unfolding, denoted as the simple and 2D unfolding, are implemented and results of these two approaches are compared. Both of these approaches can be applied to unfold differential cross section of inclusive jets measured by the ATLAS detector in LHC Run II, which will start in early summer 2015.

Key words: Quantum Chromodynamics, Jets, Unfolding

Contents

List of Tables	iii
List of Figures	iv
Introduction	1
1 QCD	5
1.1 Theoretical Ansatz	7
1.2 Experimental Ground	11
1.2.1 Scattering Reactions	11
1.2.2 Number of Colors	14
1.3 QCD as a Gauge Theory	15
1.4 Perturbative QCD	17
1.5 Non-Perturbative QCD	20
2 Experimental Framework	23
2.1 The Large Hadron Collider and The ATLAS Detector	24
2.1.1 The Large Hadron Collider	24
2.1.2 The ATLAS Detector	25
2.2 Hadron Collision at the LHC	27
2.3 Jet Algorithms	29
2.3.1 Cone algorithms	29
2.3.2 k_t algorithms	30
2.3.3 Recombination	32
2.3.4 Calorimeter jets	32
2.4 Jet corrections	34
2.4.1 Jet Energy Scale Calibration	35
2.4.2 Theory of Unfolding	36

3 Data Analysis	39
3.1 Data Characteristics	40
3.2 Event Selection	41
3.2.1 Jet Cuts	41
3.2.2 Jet Matching	42
3.3 Unfolding	43
3.4 Comparison with NLO Prediction	49
Conclusion	55
Appendices	59
A Cut and Match Results	61
A.1 Cut Results	62
A.2 Match Results	63
A.3 Truth and Reco p_T Spectra	64
B Unfolding Results	67
B.1 Matching Efficiencies	68
B.2 Slices in Unfolding Matrix	71
B.3 Unfolding of p_T Spectra	75
B.4 Simple and 2D Unfolding	77
C Next-to-Leading Order QCD Predictions	79
C.1 Predictions for Run I and Run II	80
C.2 Prediction Uncertainties	83
C.3 Pythia and Next-to-Leading Order	85
Bibliography	86

List of Tables

1.1	Quantum numbers of selected baryons known in 1950s. S strangeness, Y hypercharge, T isospin, T_3 third component of isospin, Q electrical charge.	8
1.2	Quantum numbers of three quarks which existence was predicted by Gell-Mann and Zweig in 1964.	10
3.1	The cross-sections (XS), filter efficiency (FE) and number of events for the JZXW samples, which differ in the leading truth jet p_T range.	40
A.1	Statistics for matching and cutting procedures described in Sections 3.2.1 and 3.2.2 displayed for all jets as well as for individual JZ samples, which are defined in Table 3.1. At the top, the numbers of initial reco and truth jets are shown respectively. For each cut, the number of jets, removed by it, is shown, including a relative number according to the original number of reco or truth jets respectively. The last two lines show the statistics for matching procedure including number of jets, which were (un)matched.	65

List of Figures

1	History of elementary particle physics.	2
1.1	The system of fundamental particles of the SM.	6
1.2	Eigenvalues of three-dimensional representation of $\mathfrak{su}(3)$ Lie Algebra.	9
1.3	Baryonic octuplet encapsulating baryons from Table 1.1. For baryons in this diagram, the relation $Y = S + 1$ holds.	10
1.4	Scattering reaction $e^- N \rightarrow e^- N$ with kinematics variables and vertex algebraic structures.	12
1.5	(a) $e^- e^+$ annihilation into the pair of fermion anti-fermion. Constants siting in both vertices are denoted, with α being the Fine Structure Constant and Q_f the charge of fermion f in units of positron charge. (b) π^0 meson decay into a pair of photons with closed fermion loop.	14
1.6	Leading order Feynmann diagrams in the scattering reaction $q\bar{q} \rightarrow q\bar{q}$ with denoted transferred momentum k	17
1.7	Perturbative corrections to the Feynmann diagram from Figure 1.6 representing the scattering reaction $q\bar{q} \rightarrow q\bar{q}$. Dashed line represents a scalar ghost particle.	18
1.8	Experimental measurements of running coupling constant $\alpha_S(Q)$ (solid line) and its uncertainty (yellow band). $Q = \sqrt{ k^2 }$ in comparison to (1.33).	19

2.1	Diagram showing the locations of the four main experiments (ALICE, ATLAS, CMS and LHCb) that take place at the LHC. Located between 50 m and 150 m underground, huge caverns have been excavated to house the giant detectors. The Super Proton Synchotron (SPS), the final link in the pre-acceleration chain, and its connection tunnels to the LHC, are also shown.	25
2.2	(a) An overview of the ATLAS detector (b) Detail on the inner detector and the calorimeters - the dominant sub-detector systems used in this thesis.	26
2.3	Schematic representation of an inelastic proton-proton collision.	28
2.4	Illustration of (a) infrared unsafety and (b) collinear unsafety of fixed cone jet algorithm.	31
2.5	Illustration of k_t (top) and anti- k_t (bottom) jet algorithms with $R = 1$ for calorimeter signal towers in azimuthal angle ϕ and pseudorapidity y . Towers of the same color were clustered into one jet.	33
2.6	Three levels of jet reconstruction.	35
3.1	Comparison of p_T spectra of reco and truth jets, after event selection, for selected $ y < 0.5$ rapidity bin. Each p_T bin was divided by its width, so y -axis has physical meaning of double differential cross section in p_T and y . Bottom graph contains the relative difference between reco and truth spectra.	43
3.2	Unfolding matrix for matched reco and truth jets with rapidity $ y < 0.5$, corresponding to one of eight transfer matrices used by the simple unfolding approach. Each cell is proportional to the number of jets with truth p_T in range determined by the x -axis, which were reconstructed to the reco jets with p_T determined by the y -axis. White space signalize no input.	45

3.3 Transfer matrix used by the 2D unfolding approach. Each cell is proportional to the number of jets with truth p_T and rapidity y determined by the x -axis, which were reconstructed to the reco jets with p_T and y determined by the y -axis. Marked square in $ y < 0.5$ region is the matrix shown in Figure 3.2. Projection of this matrix on the x and y -axis corresponds to the p_T spectrum of matched truth and reco jets for corresponding rapidity bin respectively. For better understanding of structure of this matrix, I have created some slices, which are shown in Appendix B.2.	46
3.4 Comparison of matching efficiencies of simple and 2D unfolding approaches for $ y < 0.5$ rapidity bin. Matching efficiencies are compared for both reco jets (left) and truth jets (right). Matching efficiencies for all rapidity bins are shown in Appendix B.1.	48
3.5 Comparison of p_T spectra of reco jets and the unfolded p_T spectra (2D unfolding approach) with the p_T spectra of truth jets on the left. The graph on the right shows the comparison of unfolded spectra, obtained by the 2D and simple unfolding approaches, with the p_T spectra of truth jets. Both graphs are for $ y < 0.5$ rapidity regions. Results for all rapidity bins are shown in Appendices B.3, B.4.	48
3.6 Comparison of next-to-leading order QCD predictions of double differential inclusive jet cross section (black) for proton-proton collisions at $\sqrt{s} = 13$ TeV (filled circles), corresponding to the LHC Run II, and $\sqrt{s} = 8$ TeV (empty circles), corresponding to the LHC Run I. The cross section is multiplied by integrated luminosities and bin width in p_T , to obtain the expected numbers of jets observed in each p_T bin (blue). Figure shows only $ y < 0.5$ rapidity bin, remaining rapidity bins are shown in Appendix C.1.	50
3.7 Theoretical uncertainties for next-to-leading order QCD predictions of inclusive jet double differential cross section for proton-proton collisions at $\sqrt{s} = 8$ TeV (top) and $\sqrt{s} = 13$ TeV (bottom) for $ y < 0.5$ rapidity bin. Uncertainties for other rapidity bins are shown in Appendix C.2.	51

3.8 Comparison of PYTHIA8 prediction with next-to-leading order QCD prediction of inclusive jet double differential cross section for $ y < 0.5$ rapidity bin, with uncertainties of next-to-leading order QCD predictions symbolized by the blue area. Comparisons for other rapidity bins are shown in Appendix C.3.	52
A.1 Impact of 4 cuts, defined in Section 3.2.1, on differential cross section in p_T of reco jets (top) and truth jets (bottom). Black crosses represent the original uncutted spectrum, green area then p_T spectra after event selection. Jets were identified with anti- k_t jet algorithm with $R = 0.4$	62
A.2 Results of matching procedure described in Section 3.2.2 demonstrated on differential cross section in p_T of reco (top) and truth (bottom) jets. Black crosses represent the original p_T spectrum before event selection. The contribution of matched and unmatched jets to green area is shown. Jets were identified with anti- k_t jet algorithm with $R = 0.4$	63
A.3 Double differential inclusive jet cross section of truth (top) and reco (bottom) jets in p_T and rapidity y . For the convenience the cross sections for different rapidity bins are multiplied by the factor indicated in the legend. Jets were identified with anti- k_t jet algorithm with $R = 0.4$	64
B.1 Comparison of matching efficiencies of simple and 2D unfolding approaches for $ y < 0.5$ (top), $0.5 \leq y < 1$ (middle) and $1 \leq y < 1.5$ (bottom) rapidity bins. Matching efficiencies are shown for reco (left) and truth jets (right) respectively.	68
B.2 Comparison of matching efficiencies of simple and 2D unfolding approaches for $1.5 \leq y < 2$ (top), $2 \leq y < 2.5$ (middle) and $2.5 \leq y < 3$ (bottom) rapidity bins. Matching efficiencies are shown for reco (left) and truth jets (right) respectively.	69
B.3 Comparison of matching efficiencies of simple and 2D unfolding approaches for $3 \leq y < 3.5$ (top) and $3.5 \leq y < 4$ (bottom) rapidity bins. Matching efficiencies are shown for reco (left) and truth jets (right) respectively.	70

B.4 Slices in the transfer matrix of 2D unfolding approach from Figure 3.3. Each histogram corresponds to the p_T spectrum of reco jets, which were matched with a truth jet with p_T and rapidity shown in the legend.	71
B.5 Slices in the transfer matrix of 2D unfolding approach from Figure 3.3. Each histogram corresponds to the p_T spectrum of reco jets, which were matched with a truth jet with p_T and rapidity shown in the legend.	72
B.6 Slices in the transfer matrix of 2D unfolding approach from Figure 3.3. Each histogram corresponds to the p_T spectrum of reco jets, which were matched with a truth jet with p_T and rapidity shown in the legend.	73
B.7 Slices in the transfer matrix of 2D unfolding approach from Figure 3.3. Each histogram corresponds to the p_T spectrum of reco jets, which were matched with a truth jet with p_T and rapidity shown in the legend.	74
B.8 Comparison of p_T spectra of reco jets (black) and the unfolded p_T spectra (using 2D unfolding approach, red) with the p_T spectra of the truth jets for the first four rapidity bins.	75
B.9 Comparison of p_T spectra of reco jets (black) and the unfolded p_T spectra (2D unfolding approach, red) with the p_T spectra of the truth jets for the last four rapidity bins.	76
B.10 Comparison of results obtained by two unfolding approaches, denoted as the simple and 2D unfold, with the p_T spectra of truth jets for the first four rapidity bins.	77
B.11 Comparison of results obtained by two unfolding approaches, denoted as the simple and 2D unfold, with the p_T spectra of truth jets for the last four rapidity bins.	78

C.1 Comparison of next-to-leading order QCD predictions of double differential inclusive jet cross section (black) in p_T and rapidity of proton-proton collisions at $\sqrt{s} = 13 \text{ TeV}$ (filled circles), corresponding to the LHC Run II, and $\sqrt{s} = 8 \text{ TeV}$ (empty circles), corresponding to the LHC Run I. The cross section is multiplied by integrated luminosities and p_T bin width to obtain expected number of jets observed in each p_T bin (blue). Figures show the comparison for $0.5 < y $ (top) and $0.5 \leq y < 1$ (bottom) rapidity bins.	80
C.2 Comparison of next-to-leading order QCD prediction of double differential inclusive jet cross section (black) in p_T and rapidity of proton-proton collisions at $\sqrt{s} = 13 \text{ TeV}$ (filled circles), corresponding to the LHC Run II and $\sqrt{s} = 8 \text{ TeV}$ (empty circles), corresponding to the LHC Run I. The cross section is multiplied by integrated luminosities and p_T bin width to obtain expected number of jets observed in each p_T bin (blue). Figures show the comparison for $1 \leq y < 1.5$ (top) and $1.5 \leq y < 2$ (bottom) rapidity bins.	81
C.3 Comparison of next-to-leading order QCD prediction of double differential inclusive jet cross section (black) in p_T and rapidity of proton-proton collisions at $\sqrt{s} = 13 \text{ TeV}$ (filled circles), corresponding to the LHC Run II and $\sqrt{s} = 8 \text{ TeV}$ (empty circles), corresponding to the LHC Run I. The cross section is multiplied by integrated luminosities and p_T bin width to obtain expected number of jets observed in each p_T bin (blue). Figures show the comparison for $2 \leq y < 2.5$ (top) and $2.5 \leq y < 3$ (bottom) rapidity bins.	82
C.4 Theoretical uncertainties for next-to-leading order QCD predictions of inclusive jet double differential cross section of proton-proton collisions at $\sqrt{s} = 8 \text{ TeV}$ (left) and $\sqrt{s} = 13 \text{ TeV}$ (right) for $ y < 0.5$ (top), $0.5 \leq y < 1$ (middle) and $1 \leq y < 1.5$ (bottom) rapidity bins.	83

C.5	Theoretical uncertainties for next-to-leading order QCD predictions of inclusive jet double differential cross section of proton-proton collisions at $\sqrt{s} = 8$ TeV (left) and $\sqrt{s} = 13$ TeV (right) for $1.5 \leq y < 2$ (top), $2 \leq y < 2.5$ (middle) and $2.5 \leq y < 3$ (bottom) rapidity bins.	84
C.6	Comparison of PYTHIA8 prediction with next-to-leading order QCD prediction of inclusive jet double differential cross section in p_T and rapidity for six different rapidity bins. Blue area represents the uncertainties of next-to-leading order QCD predictions, which are depicted in Appendix C.2 in detail. . .	85

Introduction

Search for the superior equation, which could explain all the physical universe we observe, sometimes called the Theory of Everything, led some of the physicists to the concept of elementary particles, some of which define the building blocks of our observable universe, whereas the remaining govern their interaction.

From the beginning of the twentieth century, the term elementary particle was redefined by a new generation of physicists, as illustrated in Figure 1. The latest reform was caused by quarks and the invention of Quantum Chromodynamics, describing its strong interaction which, apart from the electromagnetic and weak interactions, is encapsulated by the present theory of elementary particles called the Standard Model.

Although the Standard Model contains mechanism for assigning masses to elementary particles, gravity was not included in it up to date, because the current attempts to quantize and describe gravitation as an interaction mediated by the quanta of gravity, known as gravitons, led to unrenormalizable theories. There are other questions, unresolved by the Standard Model, such as the nature of the dark part of our Universe or the origin of the matter-antimatter asymmetry.

We know that the Standard Model is not the ultimate Theory of Everything, but it successfully stands against present results from particle physics experiments. Last discoveries of elementary particles, successfully predicted by the Standard Model, occurred on ~ 100 GeV energy scale with top quark discovery [2, 3] with mass 173.34 ± 0.98 GeV in 1995 at Tevatron and Higgs boson discovery [4] with mass 125.09 ± 0.32 GeV in 2012 at CERN. If there is a new physics beyond the Standard Model on \sim TeV scale, the LHC Run II could be the first to discover it [5].

This thesis deals with the measurement of the double differential inclusive

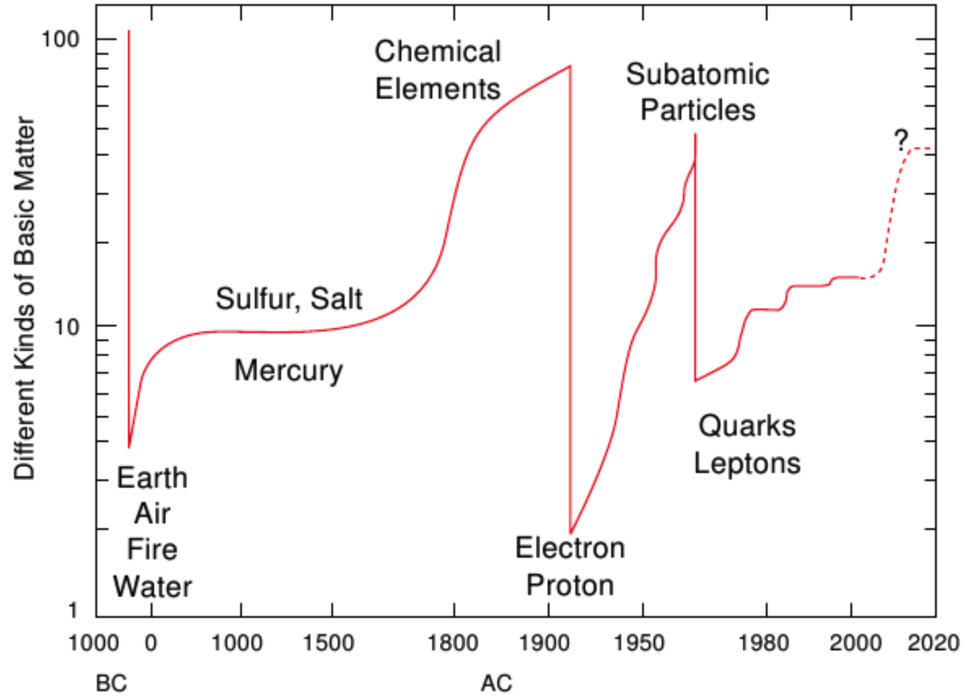


Figure 1: History of elementary particle physics. Figure taken from [1].

jet cross section in p_T and rapidity in proton-proton collisions at the ATLAS detector (inclusive means $pp \rightarrow \text{jet} + \text{anything}$). Jets are the dominant objects observed at inelastic collisions on hadron colliders and, covering a wide range of momentum transfers, they overshadow any other observable physics process in orders of magnitude. Inclusive jets measurements may therefore verify the ATLAS detector performance, as well as reveal some discrepancy in the Standard Model predictions.

First Chapter of this thesis discuss the Quantum Chromodynamics (QCD) and follows its historical development, including the experiments which led to the removal of the proton from the list of elementary particles, replacing it with the quarks. I will formulate the QCD as a quantum field theory and I will discuss the phenomenon known as a running coupling constant, so that the QCD can be divided into perturbative and non-perturbative regions.

The second Chapter concerns with the Large Hadron Collider along a detailed description of the ATLAS detector. I will use the basic features of the QCD, introduced in the previous Chapter, to define jets - objects predominantly observed at inelastic collisions on hadron colliders. At the

end of this Chapter, I will also present the jet reconstruction on ATLAS detector, including description of jet calibration and unfolding of observed spectra.

Third chapter describes the steps of the inclusive jet analysis, beginning with the characteristics of Monte Carlo data used, including event selection criteria. I use two approaches to unfold p_T spectra from detector level to particle level. In the end, I compare results obtained from both approaches and set them against the next-to-leading order perturbative QCD prediction on parton level.

Chapter 1

QCD

Is the purpose of theoretical physics to be no more than a cataloging of all the things that can happen when particles interact with each other and separate? Or is it to be an understanding at a deeper level in which there are things that are not directly observable (as the underlying quantized fields are) but in terms of which we shall have a more fundamental understanding?

Julian Schwinger

The theoretical framework of particle physics is called the Standard Model. The Standard Model describes the way how the fundamental components of matter interact through strong, weak and electromagnetic interactions. Mathematically, the Standard Model is a gauge theory with local internal symmetries of the direct product group $SU(3) \times SU(2) \times U(1)$. Gauge bosons, particles with integer spin, are assigned to generators of this symmetry - there are 8 massless gluons from $SU(3)$ and 3 massive W^\pm, Z bosons with 1 massless γ boson from electroweak $SU(2) \times U(1)$ sector. In the electroweak sector, the Higgs Mechanism is introduced to assign W^\pm, Z bosons masses and as a consequence, the new particle, Higgs boson, emerges in the Standard Model.

In addition to the bosons, the Standard Model introduces a spin-1/2 fermions, which are divided into three quark and three lepton families.

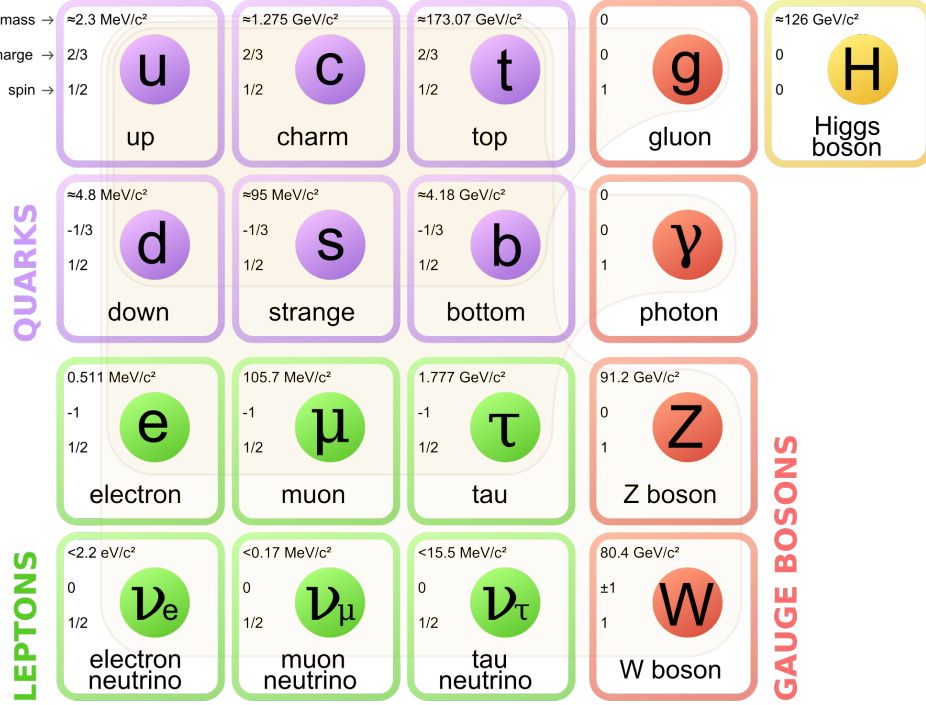


Figure 1.1: The system of fundamental particles of the SM. Figure taken from [6].

Fermions are assumed to be point-like, because there is no evidence for their internal structure to date. All fermions interact weakly, if they have electrical charge, they interact electromagnetically as well. Quarks are the only fundamental fermions which interact strongly. Figure 1.1 shows the system of fundamental particles of the Standard Model.

Quarks bind together to form hadrons and there are hundreds [7] of known hadrons up to date. Hadrons are divided into baryons (3 quarks) and mesons (quark and anti-quark pairs). A theory called Quantum Chromodynamics (QCD) describes the strong interaction between quarks. In this Chapter, I will discuss the key features of the QCD. I will give reasons for quark existence and for a description of their strong interaction as an $SU(3)$ gauge theory. After an introduction of a QCD Lagrangian, I will derive an expression for the running coupling constant, which will be used to split the QCD into perturbative and non-perturbative regions. In these regions, the QCD has to describe the strong interaction with the use of a different mathematical approaches. At the end of this Chapter, I will compare these two

approaches.

Most of the ideas, presented here, is overtaken from the textbook about the QCD [8]. The electroweak sector of the Standard Model is described in [9]. For more concise information about the Standard Model, the following textbooks can serve [10, 11].

1.1 Theoretical Ansatz

In 1950s, there had already been discovered tens of hadrons, thanks to new particle accelerators, and a lot of effort was exerted to categorize them. Each hadron obtained a series of quantum numbers including isospin T with its third component T_3 , hypercharge Y , electrical charge Q , strangeness S , baryon number B and others. Soon, people started to recognize some symmetries between these quantum numbers, like the famous Gell-Mann–Nishijima relation [12, 13]

$$Q = T_3 + 1/2Y \quad , \quad Y = B + S + \dots, \quad (1.1)$$

where dots denote charm, bottomness and topness, which were introduced after the work of Gell-Mann and Nishijima. Some of the baryons, known in 1950s, are, together with their quantum numbers, shown in Table 1.1. In 1960s, the known hadrons were successfully categorized with the theory called Eightfold Way, which was published independently by Murray Gell-Mann [14] and George Zweig [15] in 1964. The Eightfold Way successfully predicted the existence of a new particle Ω^- including its mass. In this Section, I present a basic ideas of the Eightfold Way.

The key feature of Eightfold Way is to understand hadron as a component of a representation of infinitesimal generators of $SU(3)$ flavor symmetry group. The infinitesimal generators of $SU(3)$ form a real eight-dimensional Lie Algebra $\mathfrak{su}(3)$, which fundamental representation is usually derived from Gell-Mann matrices

	S	Y	T	T_3	Q
p	0	1	1/2	1/2 -1/2	1 0
n					
Σ^+				1	1
Σ^0				0	0
Σ^-	-1	0	1	-1	-1
Λ			0	0	0
Ξ^0				1/2	0
Ξ^-	-2	-1	1/2	-1/2	-1

Table 1.1: Quantum numbers of selected baryons known in 1950s. S strangeness, Y hypercharge, T isospin, T_3 third component of isospin, Q electrical charge.

$$\begin{aligned} \lambda_1 &= \begin{pmatrix} 0 & 1 & 0 \\ 1 & 0 & 0 \\ 0 & 0 & 0 \end{pmatrix} & \lambda_2 &= \begin{pmatrix} 0 & -i & 0 \\ i & 0 & 0 \\ 0 & 0 & 0 \end{pmatrix} & \lambda_3 &= \begin{pmatrix} 1 & 0 & 0 \\ 0 & -1 & 0 \\ 0 & 0 & 0 \end{pmatrix}, \\ \lambda_4 &= \begin{pmatrix} 0 & 0 & 1 \\ 0 & 0 & 0 \\ 1 & 0 & 0 \end{pmatrix} & \lambda_5 &= \begin{pmatrix} 0 & 0 & -i \\ 0 & 0 & 0 \\ i & 0 & 0 \end{pmatrix}, & & & (1.2) \\ \lambda_6 &= \begin{pmatrix} 0 & 0 & 0 \\ 0 & 0 & 1 \\ 0 & 1 & 0 \end{pmatrix} & \lambda_7 &= \begin{pmatrix} 0 & 0 & 0 \\ 0 & 0 & -i \\ 0 & i & 0 \end{pmatrix} & \lambda_8 &= \frac{1}{\sqrt{3}} \begin{pmatrix} 1 & 0 & 0 \\ 0 & 1 & 0 \\ 0 & 0 & -2 \end{pmatrix}. \end{aligned}$$

The generators, which are usually chosen as $g_a = \frac{1}{2}\lambda_a$, obey the commutation relation $[g_a, g_b] = if_{abc}g_c$ with f_{abc} being structure constants. Cartan subalgebra of fundamental representation of $\mathfrak{su}(3)$ is generated by $H_1 = g_3$ and $H_2 = g_8$. The eigenstates of three-dimensional representation of $\mathfrak{su}(3)$ can be chosen as

$$u = \begin{pmatrix} 1 \\ 0 \\ 0 \end{pmatrix} \leftrightarrow \left(\frac{1}{2}, \frac{\sqrt{3}}{6} \right), \quad d = \begin{pmatrix} 0 \\ 1 \\ 0 \end{pmatrix} \leftrightarrow \left(-\frac{1}{2}, \frac{\sqrt{3}}{6} \right), \quad s = \begin{pmatrix} 0 \\ 0 \\ 1 \end{pmatrix} \leftrightarrow \left(0, -\frac{\sqrt{3}}{3} \right), \quad (1.3)$$

where I have assigned the eigenvalues to generators of the Cartan subalgebra $H_1 u = \frac{1}{2}u$, $H_2 u = \frac{\sqrt{3}}{6}u$ and similarly for d and s eigenstates. These eigenvalues are shown in Figure 1.2.

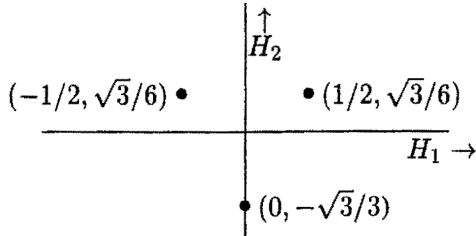


Figure 1.2: Eigenvalues of three-dimensional representation of $\mathfrak{su}(3)$ Lie Algebra. Figure taken from [16].

Next to the three-dimensional representation of $\mathfrak{su}(3)$, a eight-dimensional adjoint representation can be defined. This representation has the following eigenstates and eigenvalues

$$\begin{aligned} \frac{1}{\sqrt{2}} (g_1 \pm ig_2) &\leftrightarrow (\pm 1, 0), \\ \frac{1}{\sqrt{2}} (g_4 \pm ig_5) &\leftrightarrow \left(\pm \frac{1}{2}, \pm \frac{\sqrt{3}}{2} \right), \\ \frac{1}{\sqrt{2}} (g_6 \pm ig_7) &\leftrightarrow \left(\mp \frac{1}{2}, \pm \frac{\sqrt{3}}{2} \right), \end{aligned} \quad (1.4)$$

where again, when denoting $A = \frac{1}{\sqrt{2}}(g_1 + ig_2)$, then the upper sign of the first expression reads $[H_1, A] = A$, $[H_2, A] = 0$ and similarly for remaining 5 eigenstates. Defining

$$H_1 = T_3 \quad \text{and} \quad H_2 = \frac{\sqrt{3}}{2} Y, \quad (1.5)$$

one can easily assign hadrons from Table 1.1 to corresponding eigenvalues of the adjoint representation in (1.4), according to its third component of isospin T_3 and its hypercharge Y . This is depicted in Figure 1.3.

When the same redefinition is done to the eigenstates of the three-dimensional representation in (1.3), one can assign to u , d , s eigenstates the hypercharge Y and strangeness S as well. The concrete values for these states are shown in Table 1.2.

Another representations of $\mathfrak{su}(3)$ Lie Algebra can be constructed. The simplest way seems to be through the highest weight defining representation. From eigenvalues of adjoint representation (1.4) one can find simple roots $\alpha^1 = \left(\frac{1}{2}, \frac{\sqrt{3}}{2}\right)$, $\alpha^2 = \left(\frac{1}{2}, -\frac{\sqrt{3}}{2}\right)$, from which the highest weights follow $\mu^1 = \left(\frac{1}{2}, \frac{\sqrt{3}}{6}\right)$, $\mu^2 = \left(\frac{1}{2}, -\frac{\sqrt{3}}{6}\right)$. New representation of Lie Algebra can

	S	Y	T	T_3	Q
u	0	1/3	1/2	1/2	2/3
d	-1	-2/3	0	-1/2	-1/3
s				0	

Table 1.2: Quantum numbers of three quarks which existence was predicted by Gell-Mann and Zweig in 1964.

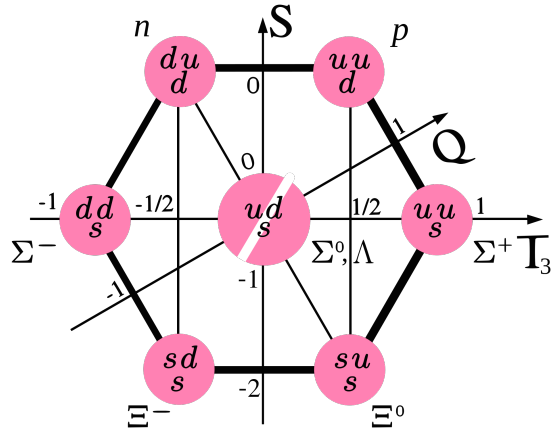


Figure 1.3: Baryonic octuplet encapsulating baryons from Table 1.1. For baryons in this diagram, the relation $Y = S + 1$ holds. Figure taken from [17].

be constructed from the highest weights. The whole procedure is described in [16] in detail.

Representations defined by the highest weight μ^1 and μ^2 respectively are called fundamental. Fundamental representation defined by μ^1 is usually denoted **3** and we have encounter it already by the expressions (1.3) and weight diagram in Figure 1.2. This representation corresponds to three different quark states. The second fundamental representation, defined by the highest weight μ^2 , corresponds to three anti-quark states and is usually denoted **3̄**. The adjoint representation, depicted in Figure 1.3 is defined by the highest weight $\mu^1 + \mu^2$.

Special interest is in representations with dimensions 10 and 8. These are present in decompositions $\mathbf{3} \otimes \mathbf{3} \otimes \mathbf{3} = \mathbf{10} \oplus \mathbf{8} \oplus \mathbf{8} \oplus \mathbf{1}$, which corresponds to the baryons composed of three quarks, and $\mathbf{3} \otimes \bar{\mathbf{3}} = \mathbf{8} \oplus \mathbf{1}$, corresponding to mesons composed of quark and anti-quark.

Important feature of quark model just presented is its capability to predict hadron masses. This is done using Gell-Mann–Okubo mass formula [18, 19]

$$M = a_0 + a_1 S + a_2 \left(T(T+1) - \frac{1}{4} S^2 \right), \quad (1.6)$$

where a_0 , a_1 and a_2 are free parameters, which are common for all hadrons in one multiplet.

In 1970, Sheldon Lee Glashow, John Iliopoulos and Luciano Maiani proposed [20] an extension to the Eightfold Way, which predicted the existence of a fourth flavor of quark - charm quark.

In 1973, Makoto Kobayashi and Toshihide Maskawa proposed [21], that the existence of 6 different quark flavors could explain the experimental observation of CP violation.

1.2 Experimental Ground

In the previous Section, I have shown, that the hadrons can be categorized by representations of $\mathfrak{su}(3)$ Lie Algebra. This lead to the model, where baryons were composed of three quarks and the mesons of quark and anti-quark. In this Section, I summarize some experimental arguments to support quark model. Firstly, I will show, that the results from the lepton scattering on nucleons can be explained by assumption, that nucleons are composed of point-like spin-1/2 particles. In the second part, I will encounter the question, why the group $SU(3)$ is connected to the theory of strong interaction.

1.2.1 Scattering Reactions

Inner structure of nucleon N can be investigated by one of the following scattering reactions

$$e^- (E \gg 1 \text{ GeV}) + N \rightarrow e^- + N, \quad (1.7)$$

$$\nu_e (E \gg 1 \text{ GeV}) + N \rightarrow \nu_e + N, \quad (1.8)$$

where I have explicitly written $E \gg 1 \text{ GeV}$ to ensure, the wavelength of lepton is $< 0.2 \text{ fm}$. By the first scattering reaction, the information about the electric charge distribution in nucleon can be extracted, whereas the second scattering reaction informs us about the weak charge distribution. From now on, I work only with scattering reaction (1.7), which was experimentally

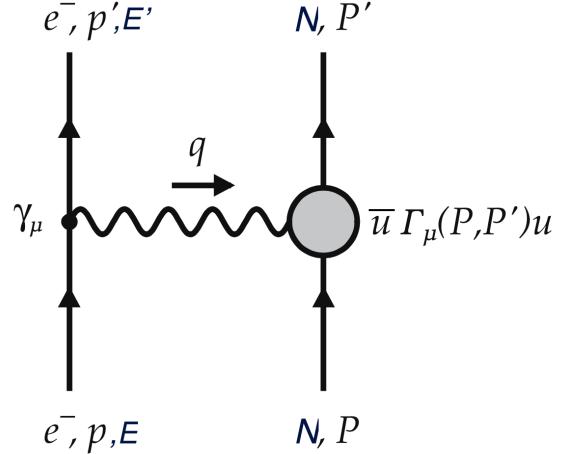


Figure 1.4: Scattering reaction $e^- N \rightarrow e^- N$ with kinematics variables and vertex algebraic structures. Figure taken from [8].

examined as the first. Feynmann diagram of this process is, together with kinematics variables and vertex algebraic structures, depicted in Figure 1.4.

Because of Lorentz-invariance of Quantum Electrodynamics, the matrix element of the nucleon vertex $\bar{u}(P', S')\Gamma_\mu u(P, S)$ has to be a Lorentz-vector. This restricts the possible form of Γ_μ to the following algebraic structure

$$\Gamma_\mu = A\gamma_\mu + BP'_\mu + CP_\mu + iDP'^\nu\sigma_{\mu\nu} + iEP^\nu\sigma_{\mu\nu}, \quad (1.9)$$

where A, \dots, E depend only on Lorentz-invariant quantities. Next condition, which has to be taken into account, is a gauge invariance of the matrix element, which can be written in the form

$$q^\mu \bar{u}(P', S')\Gamma_\mu u(P, S). \quad (1.10)$$

The further computation of cross section is straightforward and the result can be easily generalized to non-elastic scattering, by which the nucleon in final state decays. The result is usually written using inelasticity parameter $y = \frac{E-E'}{E}$, $0 \leq y \leq 1$, $y = 0$ corresponding to the elastic scattering, Bjorken variable $x = \frac{Q^2}{2P \cdot q}$, $0 < x \leq 1$, $x = 1$ denoting elastic scattering and finally, instead of negative value q^2 , the $Q^2 = -q^2$ is used. Final result can be than written in the form

$$\left. \frac{d^2\sigma}{dx dy} \right|_{eN} = \frac{8\pi M_N E \alpha^2}{Q^4} [xy^2 F_1^{eN}(Q^2, x) + (1-y) F_2^{eN}(Q^2, x)]. \quad (1.11)$$

The eN sub(super)script stresses the fact, we are dealing with scattering (1.7). F_1^{eN} and F_2^{eN} , called Structure Functions, are not determinable by the theory just presented - they have to be measured experimentally.

Structure Functions were first measured at eP scattering, at SLAC in 1968 [22], and have shown the following results

1. for $Q^2 \geq 1 \text{ GeV}$, there is no significant dependence of Structure Functions on Q^2 and
2. for $Q^2 \geq 1 \text{ GeV}$, $F_2 \approx 2x F_1$.

These results can be explained by assumption nucleon being composed of point-like spin-1/2 constituents, for which R. P. Feynmann used the term partons. In the following, I introduce the basic ideas of parton model.

To i th parton, we assign momentum $P_{i,\mu}$

$$P_{i,\mu} = \xi_i P_\mu + \Delta P_{i,\mu} \quad , \quad \max_{\mu}(\Delta P_\mu) \ll \max_{\mu} P_\mu, \quad (1.12)$$

where $\xi_i \in \langle 0, 1 \rangle$ and $\Delta P_{i,\mu}$ comes from the interaction between partons and we assume, the momentum coming from this interaction is much smaller than the total nucleon momentum P_μ . In addition, probabilities $f_i(\xi_i)$ that i th parton will carry ξ_i fraction of total momentum fulfilling

$$\int d\xi_i f_i(\xi_i) = 1 \quad (1.13)$$

must be defined. Then, for the scattering reaction (1.7) the formula for the cross section can be derived

$$\frac{d^2\sigma}{dxdy} \Big|_{eN} = \frac{4\pi M_N E \alpha^2}{Q^4} [y^2 + 2(1-y)] \sum_i f_i(x) q_i^2 x, \quad (1.14)$$

where for i th parton its electrical charge q_i was introduced. The last expression and expression (1.11) can be compared as polynomials in y resulting in

$$F_1^{eN}(x) = \frac{1}{2} \sum_i f_i(x) q_i^2 \quad , \quad F_2^{eN}(x) = \sum_i f_i(x) q_i^2 x. \quad (1.15)$$

It can be easily checked, that $F_2^{eN}(x) = 2x F_1^{eN}(x)$. Functions $f_i(x)$, just introduced, are called Parton Distribution Functions and their important role in QCD will be discussed in Section 3.4 in more details.

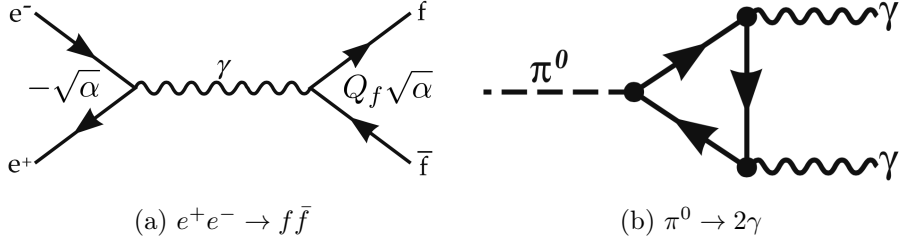


Figure 1.5: (a) e^-e^+ annihilation into the pair of fermion anti-fermion. Constants sitting in both vertices are denoted, with α being the Fine Structure Constant and Q_f the charge of fermion f in units of positron charge. (b) π^0 meson decay into a pair of photons with closed fermion loop.

The conclusion, which we should learn from this Section is, that the experimental results of scattering reactions can be explained by assumption nucleons being composed of spin-1/2 point-like partons, now called quarks.

1.2.2 Number of Colors

Despite the strong confidence in the parton model, a theory, which would describe the interaction between partons, was still missing. At the beginning of 1970s, there was no direct evidence on how the theory would look like. The theory of electroweak unification successfully suggested, that our Universe at a subatomical level, could be described by a gauge theories, but to construct a gauge theory of strong interaction, the number of colors first had to be known.

Number of colors N_C is the number of different kinds of quarks of the same flavor with respect to a new interaction. In this part, I present three arguments to demonstrate, that $N_C = 3$.

The first argument is the analysis of the electron-positron annihilation into the pair of fermion and anti-fermion

$$e^+ e^- \rightarrow f\bar{f}. \quad (1.16)$$

Feynmann diagram of this reaction is shown in Figure 1.5a, where constants sitting in two vertices are emphasized. α stands for Fine Structure Constant and Q_f for the charge of the fermion f in units of positron charge. The total cross section has to be proportional to

$$\sigma(e^-e^+ \rightarrow f\bar{f}) \sim Q_f^2 \alpha^2. \quad (1.17)$$

In the case fermion f being quark, there is new degeneracy coming from different colors of quark-antiquark pair in final state, and the total cross section has to be multiplied by factor N_C . Experimentally, the so called R -factor is measured

$$R = \frac{\sigma(e^+e^- \rightarrow \text{hadrons})}{\sigma(e^+e^- \rightarrow \mu^+\mu^-)} = \left(\sum_q Q_q^2 \right) N_C, \quad (1.18)$$

where the sum on the left hand side is over all possible quark flavors. When we use the quark model proposed by Gell-Mann a Zweig, and substitute the values from Table 1.2, then

$$R = \left[\left(\frac{2}{3} \right)^2 + \left(\frac{-1}{3} \right)^2 + \left(\frac{-1}{3} \right)^2 \right] N_C = \frac{2}{3} N_C. \quad (1.19)$$

Experimental results for R -ratio have shown [23], that $N_C = 3$.

The second argument, to support $N_C = 3$, is the measurement of the decay width of π_0 meson, which is depicted in Figure 1.5b. For decay width Γ it can be derived

$$\Gamma = 7.63 \left(\frac{N_C}{3} \right)^2 \text{ eV}, \quad (1.20)$$

which, compared to the experimental value $\Gamma = 7.57 \pm 0.32 \text{ eV}$ [23], leads again to $N_C = 3$.

The third argument is purely theoretical and states, that the Standard Model is internally consistent only, if there are three colors [8]. This indicates, there is some linking between electroweak and strong sectors of the Standard Model, and motivates the search for Grand Unified Theories.

1.3 QCD as a Gauge Theory

Putting arguments of the previous Section all together, there is the strong experimental evidence, that nucleons consist of point-like spin-1/2 particles, called quarks, and that quarks bring into the theory new degeneracy factor $N_C = 3$, which can be understood as three different strong charges. In this Section, I follow the Yang-Mills theory [24] and define the QCD Lagrangian.

Nowadays, the quark-quark strong interaction is understood as an $SU(3)$ gauge theory in a degree of freedom called color. The generators of $SU(3)$ are derived from Gell-Mann matrices (1.2) and act on quark color triplet wave functions.

$$\psi(x) = \begin{pmatrix} \psi_r(x) \\ \psi_g(x) \\ \psi_b(x) \end{pmatrix}. \quad (1.21)$$

Following the Yang-Mills theory, to each generator $\frac{\lambda^a}{2}$ a gluon field $A_\mu^a(x)$ and a gluon field strength tensor

$$F_{\mu\nu}^a = \left(\partial_\mu A_\nu^a - \partial_\nu A_\mu^a + g f^{abc} A_\mu^b A_\nu^c \right) \quad (1.22)$$

are assigned, where g denotes the coupling constant of strong interaction and f^{abc} structure constant defined in Section 1.1. QCD Lagrangian

$$\mathcal{L}_{\text{QCD}} = \bar{\psi} \left(-i\partial_\mu + g \frac{\lambda}{2} A_\mu^a(x) \right) \gamma^\mu \psi - \frac{1}{4} F_{\mu\nu}^a F_a^{\mu\nu} \quad (1.23)$$

is invariant under local transformation

$$\psi(x) \rightarrow \psi'(x) = e^{ig\Theta(x)} \psi(x), \quad (1.24)$$

$$A_\mu(x) \rightarrow e^{ig\Theta(x)} \left(A_\mu(x) + \frac{i}{g} \partial_\mu \right) e^{-ig\Theta(x)},$$

where

$$\Theta(x) = \frac{1}{2} \lambda^a \Theta^a(x) \quad , \quad A_\mu(x) = \frac{1}{2} \lambda^a A_\mu^a(x). \quad (1.25)$$

There is no mass term in Lagrangian (1.23), because mass term $m\bar{\psi}\psi$ vary under gauge transformation (1.24). To include quark mass term in QCD Lagrangian, the Higgs mechanism [25], which is explained in [9] in detail, has to be used.

QCD Lagrangian (1.23) together with gauge transformations (1.24) are sufficient for determination of Feynman rules - the key ingredient in the perturbative QCD, which we will, after one final remark, discuss in the next Section.

By derivation of a gluon propagator, the gauge-fixing term has to be

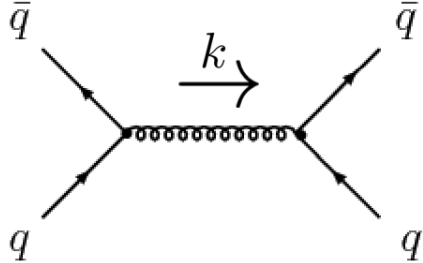


Figure 1.6: Leading order Feynmann diagrams in the scattering reaction $q\bar{q} \rightarrow q\bar{q}$ with denoted transferred momenta k .

added to the QCD Lagrangina.

$$\mathcal{L}_{\text{QCD}}^{\text{gauge-fixing}} = -\frac{1}{2\xi} (\partial_\mu A_a^\mu)^2. \quad (1.26)$$

This term confines the possible gauges to one class parametrized by real parameter ξ . In non-Abelian gauge theories this term must be supplemented by the so called ghost term, which brings into the theory a new unphysical scalar particle obeying fermionic statistic. More details on the Faddev-Popov ghost field can be found in [26].

1.4 Perturbative QCD

The Quantum Electrodynamics and The QCD are both the quantum field gauge theories, but they differ in one killing feature - the former is Abelian whereas the latter is not. The non-Abelian character of the QCD leads to new phenomenons of triple and quartic gluonic interactions, which have an origin in the QCD Lagrangian (1.23). In this Section, I discuss one remarkable consequence - the running coupling constant.

We start with the scattering process

$$q\bar{q} \rightarrow q\bar{q}, \quad (1.27)$$

which is depicted in the lowest order of perturbation theory by the Feynman graph in Figure 1.6. Except contribution of this graph to the scattering amplitude (which is the only contribution $\sim g^2$) there are 12 other Feynman diagrams with contributions $\sim g^4$. These are depicted in Figure 1.7.

The contributions from all the Feynman diagrams are calculated in [8] in detail. There is shown, that all these contributions together are logarithmically divergent. This divergence can be removed, when from the scattering amplitude for arbitrary momentum transfer k^2 the scattering amplitude for

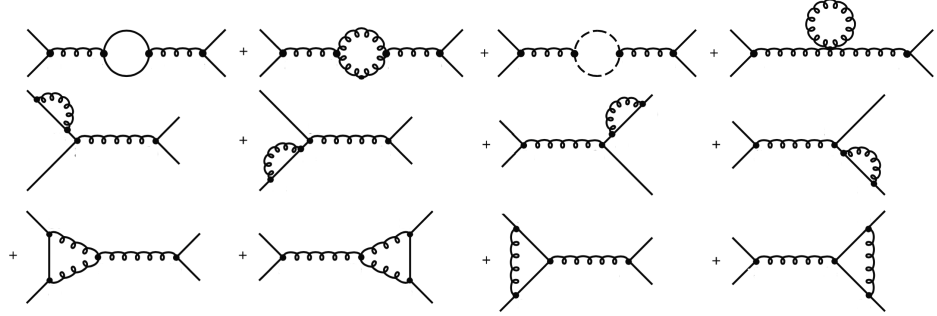


Figure 1.7: Perturbative corrections to the Feynmann diagram from Figure 1.6 representing the scattering reaction $q\bar{q} \rightarrow q\bar{q}$. Dashed line represents a scalar ghost particle.

fixed momentum transfer $k^2 = -M^2$ is subtracted. This is how the renormalized coupling constant g_R is obtained and here is its final expression

$$g_R = g_0 - \frac{g_0^3}{16\pi^2} \left(\frac{11}{2} - \frac{1}{3}N_F \right) \ln \left(\frac{-k^2}{M^2} \right) + \mathcal{O}(g_0^5). \quad (1.28)$$

Here g_0 stands for the coupling constant measured at the renormalization scale $k^2 = -M^2$ and N_F for the number of different quark flavors with mass $m^2 \ll |k^2|$. Dependence of g_R on transferred momentum k^2 is evident, but there are another two intertwined dependences - on renormalization scale M and on coupling constant at renormalization scale $g_0 = g_R|_{k^2=-M^2}$. For next purpose, it is convenient to use the dependence schema

$$g_R = g_R(-k^2, g_0(M)), \quad (1.29)$$

which allows us to use the advantages of a β -function. With the usage of the equation (1.28), the differential equation for $g_0(M)$ can be obtained

$$\beta(g_0) \equiv M \left(\frac{\partial g_R}{\partial M} \right)_{-k^2=M^2} = M \left(\frac{dg_0}{dM} \right)_{-k^2=M^2} \quad (1.30)$$

$$= -b_0 g_0^3 + \mathcal{O}(g_0^5), \quad b_0 = \frac{1}{16\pi^2} \left(11 - \frac{2N_F}{3} \right), \quad (1.31)$$

and solved directly to obtain coupling constant g_0 for arbitrary scale $-k^2$

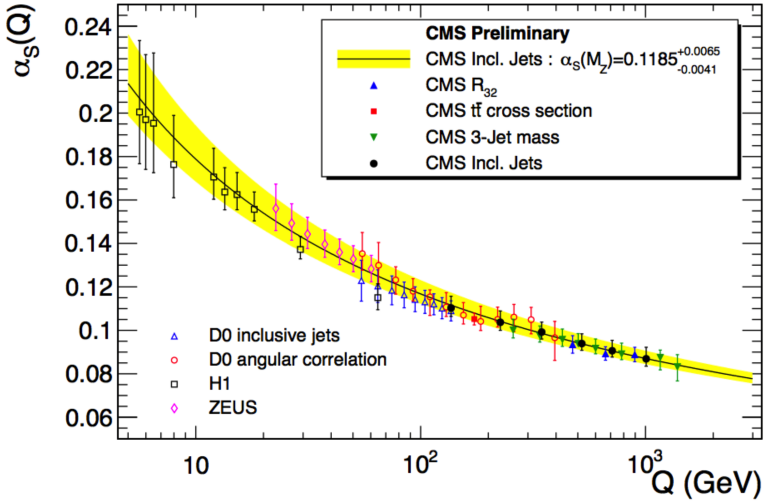


Figure 1.8: Experimental measurements of running coupling constant $\alpha_S(Q)$ (solid line) and its uncertainty (yellow band). $Q = \sqrt{|k^2|}$ in comparison to (1.33). Figure taken from [28].

$$\int_{g_0(M^2)}^{g_0(-k^2)} \frac{dg_0}{g_0^3} = -b_0 \int_{M^2}^{-k^2} \frac{dM}{M}, \quad (1.32)$$

with solution

$$\alpha_S(-k^2) = \frac{\alpha_S(M^2)}{1 + \frac{\alpha_S(M^2)}{4\pi} \left(11 - \frac{2N_F}{3} \right) \ln \left(\frac{-k^2}{M^2} \right)}, \quad g_0^2(-k^2) = 4\pi\alpha_S(-k^2), \quad (1.33)$$

which is the final expression for running coupling constant up to one-loop order. This dependence corresponds to experimental data, which are depicted in Figure 1.8. Coupling constant decreases with increasing momentum transfer allowing the use of the perturbation theory. This is known as the Principle of Asymptotic Freedom [27].

On the other hand, when the momentum transfer decreases, there is a special value $-k^2 = \Lambda^2$ for which the last expression diverges

$$-1 = \frac{\alpha_S(M^2)}{4\pi} \left(11 - \frac{2N_F}{3} \right) \ln \left(\frac{\Lambda^2}{M^2} \right). \quad (1.34)$$

Experimental value is $\Lambda = 213^{+38}_{-35}$ MeV [29] and demonstrates, that the per-

turbative QCD cannot be used at low energy transfers. In fact, the running coupling constant $\alpha_S(-k^2)$ reaches value ~ 1 on momenta transfers $\sqrt{|k^2|} \sim 500$ MeV.

The behavior of coupling constant at low energy transfers is not explainable in the language of the perturbative QCD just presented. It is non-perturbative effect known as the Principle of Color Confinement, which states, that quarks, when separate, the gluon force field between them becomes stronger instead of diminishing. The accumulated energy is consumed by the creation of quark anti-quark pair, until there is no free color charge left. This principle forbids us from observing free quarks.

To understand e.g. structure of proton with rest mass < 1 GeV, it is clear, the non-perturbative QCD has to be used. Basic ideas of the non-perturbative QCD are introduced in the next Section.

1.5 Non-Perturbative QCD

The most well established non-perturbative approach to the QCD is a Lattice QCD. In this Section, I discuss the basic features of the Lattice QCD. More information on this extended topic can be found in [8, 30].

Lattice QCD is the QCD formulated on a hypercubic equally spaced lattice in space and time, with a lattice parameter a denoting the distance between neighboring sites. Quark fields are placed on sites, whereas the gluon fields sit on the links between neighboring sites. From the QCD, the Lattice QCD inherits the gauge invariance, which has to be formulated on the lattice structure. For $a \rightarrow 0$ the Lattice QCD action coincides with that of QCD. The Lattice QCD contains 6 parameters - strong coupling constant and masses of 5 quarks (the top quark with lifetime $\sim 10^{-24}$ s is not assumed by the theory).

Unlike the perturbative expansions, used in perturbative QCD, the Lattice QCD uses a numerical evaluation of a path integral to perform non-perturbative calculations. Lattice QCD calculations are limited by the availability of computational resources and the efficiency of algorithms. The Lattice QCD suffers with both statistical and systematical errors, the former arising from the use of Monte-Carlo integration, the latter, e.g. from the use of non-zero values of a .

The current Lattice QCD calculations are made on supercomputers like

the QCDCQ supercomputer [31] with peak speed of 500 TFlops, using lattice spacing $a \sim 0.05 - 0.15$ fm in lattice volume $V \sim (2 - 6 \text{ fm})^3$.

The Importance of the Lattice QCD lies in its ability to predict masses of observed mesons and baryons, including quark masses itself, and in investigation of topological structure of a QCD vacuum. The Lattice QCD can be used to obtain Parton Distribution Functions (1.13), helping us to understand the structure of hadrons. Phenomenology of the Lattice QCD also explains the Principle of Color Confinement.

Chapter 2

Experimental Framework

*What we observe is not nature itself, but nature exposed to our method
of questioning.*

Werner Heisenberg

In the previous Chapter, I have introduced the key features of the QCD, today's theory of the strong interaction. A predictions of the QCD are tested at particle accelerators persistently, with no signs for a new physics so far. Large Hadron Collider, which will open energy regions not observed yet, can change this very soon.

The most prevailing objects, we observe at inelastic collisions on hadron colliders, are collimated particle showers, called jets. With energies covering a range from a few GeV to a few TeV, at the Large Hadron Collider, and with the direct connection to the QCD processes, occurring during the collision, the jets are a suitable candidates allowing testing the QCD up to its edges.

In this Chapter, I present the Large Hadron Collider and the ATLAS detector. With the use of the QCD, defined in the previous Chapter, I give reasons for the necessity of jets, and I define the jet algorithms allowing us to straightforwardly recombine a set of particles into jets. At the end of this Chapter, I describe the essential steps, which has to be taken, to correctly reconstruct jets on the ATLAS detector.

2.1 The Large Hadron Collider and The ATLAS Detector

CERN, the European Organization for Nuclear Research, is the largest particle physics laboratory in the world, located near Geneva, at the border between Switzerland and France. The current flagship project at CERN is a particle accelerator called the Large Hadron Collider, which, together with the ATLAS Detector, will be presented in this Section.

2.1.1 The Large Hadron Collider

The Large Hadron Collider (LHC) [32, 33] is a charged particle accelerator, which was built in the areas formerly used by the Large Electron-Positron Collider. The main accelerator ring, of 27 km circumference, is located around 100 m below the surface, with four main experiments located around the ring: A Large Ion Collider Experiment (ALICE), A Toroidal LHC ApparatuS (ATLAS), Compact Muon Solenoid (CMS) and Large Hadron Collider beauty (LHCb). The complete accelerator and detector system is shown in Figure 2.1.

After 20 years of design, development, construction and testing, the LHC has started to operate on November 23, 2009 and soon thereafter (March 30, 2010) the proton-proton collisions achieved the center-of-mass energy $\sqrt{s} = 7 \text{ TeV}$, which is a half of the design energy of the machine. On April 5, 2012, the machine started its successful $\sqrt{s} = 8 \text{ TeV}$ run.

Next to the proton-proton collisions, first heavy-ion Pb-Pb collisions took place in 2010 at a center-of-mass energy per pair of colliding nucleons $\sqrt{s} = 2.76 \text{ TeV}$. Proton-Pb collisions at $\sqrt{s} = 5.02 \text{ TeV}$, occurring on LHC during 3 weeks of 2013, successfully demonstrated the LHC capability to provide asymmetric collisions.

The first running period of the LHC, Run I, was very successful and resulted in the discovery of the Higgs boson on July 4, 2012 [4]. The accelerator complex, including its experiments, has been upgraded for two years and the Run II is expected to start in early summer 2015 [35, 36]. In Run II, the center-of-mass energy of proton-proton collisions will be raised to $\sqrt{s} = 13 \text{ TeV}$, and the beam crossing time is expected to be reduced from the current 50 ns to 25 ns. The integrated luminosity should be $\sim 100 \text{ fb}^{-1}$ after three years of data collecting.

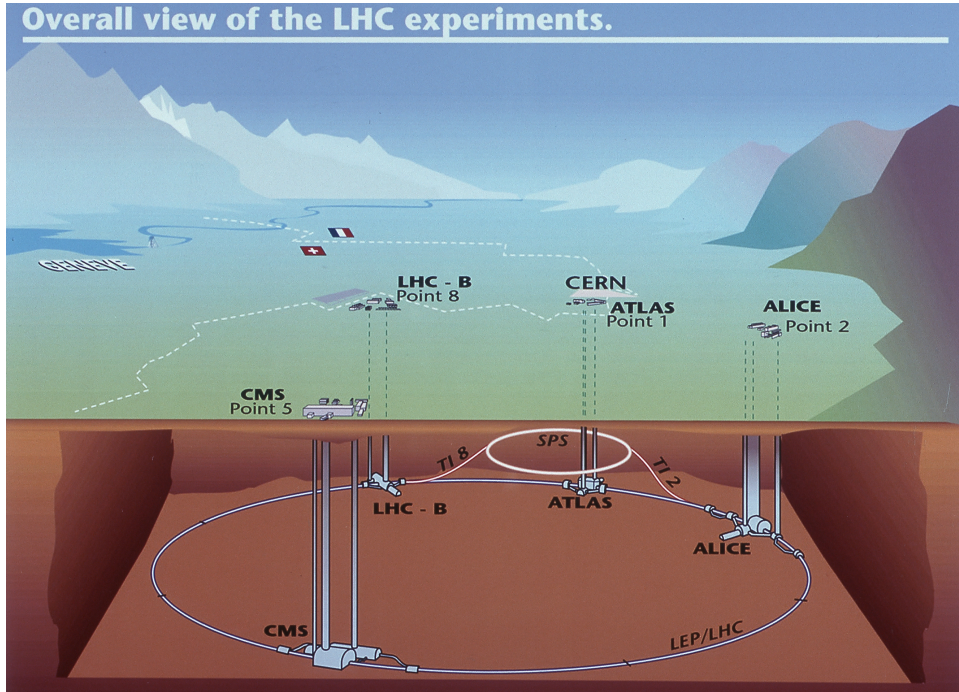
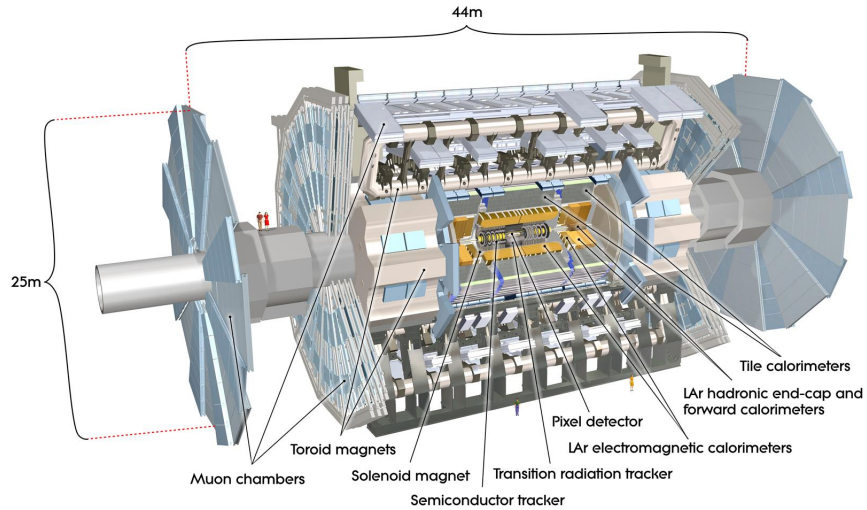


Figure 2.1: Diagram showing the locations of the four main experiments (ALICE, ATLAS, CMS and LHCb) that take place at the LHC. Located between 50 m and 150 m underground, huge caverns have been excavated to house the giant detectors. The Super Proton Synchotron (SPS), the final link in the pre-acceleration chain, and its connection tunnels to the LHC, are also shown. Figure taken from [34].

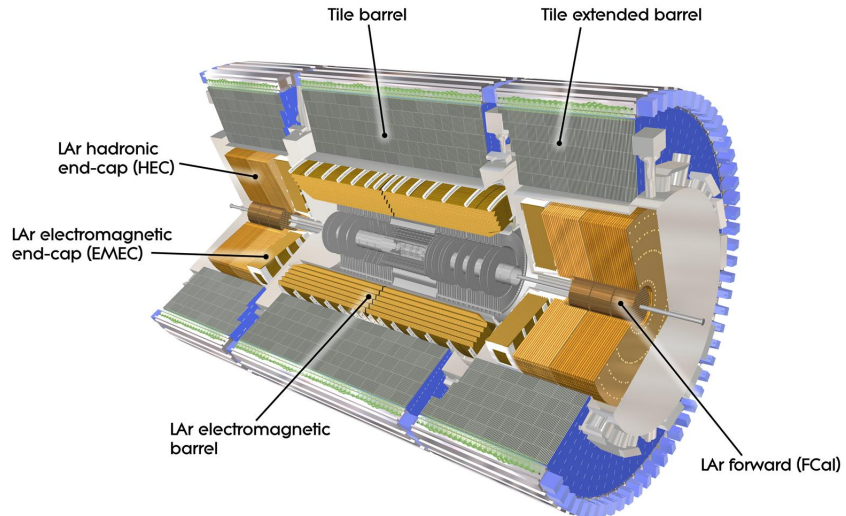
2.1.2 The ATLAS Detector

The ATLAS detector [37] is a general-purpose detector surrounding one of the interaction points of the LHC and, with ~ 100 million of individual electronic channels, it is the most complicated instrument ever created. The purpose of the ATLAS detector is to record particle collisions, up to the center-of-mass energy per pair of colliding nucleons $\sqrt{s} = 14$ TeV. A detector overview is shown in Figure 2.2a, where the main sub-detector systems can be seen: the inner detector, used to reconstruct charged-particle tracks, the electromagnetic calorimeters, the hadronic calorimeters, and the muon spectrometer.

ATLAS uses a right-handed coordinate system with its origin at the interaction point in the center of the detector and the z axis along the beam



(a) ATLAS detector.



(b) Inner detector and calorimeter systems.

Figure 2.2: (a) An overview of the ATLAS detector (b) Detail on the inner detector and the calorimeters - the dominant sub-detector systems used in this thesis. Figures taken from [38].

pipe. The x axis points from the interaction point to the center of the LHC ring, and the y axis points upward. Cylindrical coordinates (r, ϕ) are used in the transverse plane, ϕ being the azimuthal angle around the beam pipe. Instead of polar angle θ , pseudorapidity η and rapidity y are used in this thesis. In the following definitions of pseudorapidity η and rapidity y , E stands for the total energy and p for size of total momentum:

$$\eta = -\frac{1}{2} \ln \left(\frac{p + p_z}{p - p_z} \right) = -\ln \left[\tan \left(\frac{\theta}{2} \right) \right], \quad (2.1)$$

$$y = -\frac{1}{2} \ln \left(\frac{E + p_z}{E - p_z} \right). \quad (2.2)$$

The transverse momentum $p_T = \sqrt{p_x^2 + p_y^2}$ presents the component of a momentum perpendicular to the beam line.

The main detector system, relevant to this thesis, is the ATLAS calorimeter system, which is emphasized in Figure 2.2b. The calorimeter is divided into sub-detectors, providing an overall coverage up to $|\eta| < 4.9$. The electromagnetic calorimeter, covering region $|\eta| < 3.2$, is a high-granularity sampling detector, in which the liquid argon (LAr) active medium is interspaced with layers of lead absorber. The hadronic calorimeters are divided into three sections: a tile scintillator/steel calorimeter is used in both the barrel ($|\eta| < 1.0$) and extended barrel cylinders ($0.8 < |\eta| < 1.7$), while the hadronic endcap ($1.5 < |\eta| < 3.2$) consists of LAr/copper calorimeter modules. The forward calorimeter measures both electromagnetic and hadronic energy in the range $3.2 < |\eta| < 4.9$ using LAr/copper and LAr/tungsten modules.

2.2 Hadron Collision at the LHC

Following the Reference about Monte Carlo event generators [23] and the picture in Figure 2.3, I discuss, in this Section, the phenomenology of inelastic proton-proton collisions.

Two incoming protons can be understood as two bags of partons. The inelastic proton-proton collision is dominated by the strong interaction between two partons, called incoming partons. Momentum transfer at their interaction is $Q \gg \Lambda$, so the perturbative QCD is used to describe the initial

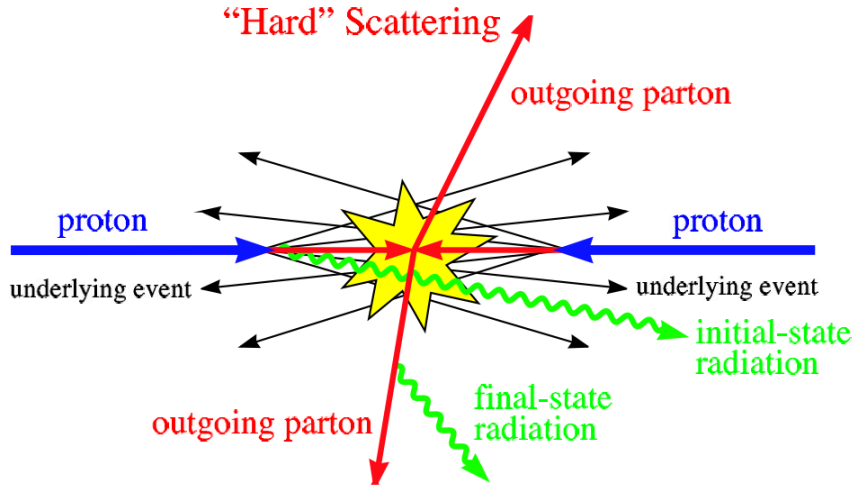


Figure 2.3: Schematic representation of an inelastic proton-proton collision.
Figure taken from [39].

process of a hard scattering. The remaining energy is carried out by the rest of the partons, which create the so called underlying event - particles, which do not come from the dominant QCD processes.

When the partons are sufficiently far from each other, the non-perturbative QCD is used to describe the process of hadronization, in which a set of colored partons is transformed into a set of colorless primary hadrons, which may then decay further.

During all the collision, the color charges of partons interact, resulting in a radiation of gluons $q \rightarrow qg$. This process is described by the perturbative QCD and leads to infrared and collinear divergences. However, infrared divergences are canceled by Kinoshita–Lee–Nauenberg theorem [40, 41], so only collinear divergences remain. There is no mechanism known up to date, which would solve the problem with collinear divergences. However, observables inclusive enough, to be insensitive to processes, that distinguish between different numbers of partons, are not affected by infrared divergences. There is no possibility, how to theoretically predict the energy of hardest outgoing particle, but it is possible to predict the energy flow in a cone from the point of scattering.

This is where the term jet comes to play. A jet can be naively seen as a group of collimated particles generated by the hadronization of a parton in

the scattering process, and it is the most important object used on hadron colliders for analysis of QCD processes.

2.3 Jet Algorithms

A jet algorithm is a generic "recipe", which takes a set of particles (or other objects with defined four-momenta) and returns jets created from them. The jet algorithm usually involves a set of parameters, which, together with the algorithm, fully specify the jet definition. According to the remarks at the end of the previous Section, jet algorithms should fulfill the following conditions

1. Infrared safety - the presence of an additional soft particle should not affect the recombination of particles into a jet.
2. Collinear safety - jet reconstruction should not depend on the fact, if the transverse momentum is carried by one particle, or if the particle is split into more collinear particles.

Two important steps must be defined in each jet algorithm

1. Clustering - description how the input objects are clustered into jets.
2. Recombination - determination of physical quantities of jets.

Additional steps may include the preclustering, which reduces the number of input objects for jet algorithm.

This Sections starts with the definition of two classes of jet algorithms. First of these are cone algorithms, which seems to me to be more illustrative, and k_t algorithms, which are used in ATLAS experiment. After a characterization of these algorithms, I introduce two possible recombination schemes, and, at the end of this Section, I give a short description, how the objects, defined by its four-momenta, are constructed from the signal observed on the ATLAS detector. Detailed description as well as other jet algorithms can be found in [42, 43].

2.3.1 Cone algorithms

The first step of these algorithms is to order all input objects (reconstructed detector objects with four-momentum representation) in decreasing order in transverse momentum p_T . If the object with the highest p_T is above a seed threshold, all objects within a cone in rapidity y and azimuth ϕ

with $\Delta R = \sqrt{\Delta y^2 + \Delta \phi^2} < R_{cone}$, where R_{cone} is the fixed cone radius, are recombined. A new cone is centered around a new direction and all the objects within the new cone are recombined and again, the direction is updated. This process continues, until the direction of the cone does not change anymore after recombination, at which point, the cone is considered stable and is called a proto-jet.

At this point, the next seed is taken from the input list and a new proto-jet is formed with the same iterative procedure. This continues until no more seeds are available.

The proto-jets found by this procedure can share some constituents. Constituents shared between two proto-jets are recombined into a new proto-jet and if the ratio $E_T^{shared}/\min(E_T^{neighbor}) > f$ is over the certain threshold, for example $f = 0.5$, the neighboring proto-jets are recombined into one proto-jet (shared constituents are taken only once). If this condition is not satisfied, the shared constituents are assigned to the nearest proto-jet. When a proto-jet does not share constituents it is recombined into the jet.

This algorithm is both not infrared safe (Figure 2.4a) and not collinear safe (Figure 2.4b). The infrared insensitivity can be improved by adding the midpoints between pairs of proto-jets fulfilling $R_{cone} < \Delta R < 2R_{cone}$ and repeating the iterative procedure with midpoints being new seeds. Since the collinear unsafety arises from the use of seed towers, Seedless cone algorithm was developed, which searches the entire detector to find all stable proto-jets.

Typical parameters used by the fixed cone algorithms are a seed threshold of $p_T > 1 \text{ GeV}$, and a narrow ($R_{cone} = 0.4$) or a wide cone jet ($R_{cone} = 0.7$) option.

2.3.2 k_t algorithms

In this class of algorithms, all pairs (i, j) of input objects are analyzed with respect to their relative transverse momentum squared, defined by

$$d_{ij} = \min(p_{T,i}^{2p}, p_{T,j}^{2p}) \frac{\Delta R_{ij}^2}{R^2}, \quad (2.3)$$

and the squared p_T of object i relative to the beam axis

$$d_i = p_{T,i}^{2p}. \quad (2.4)$$

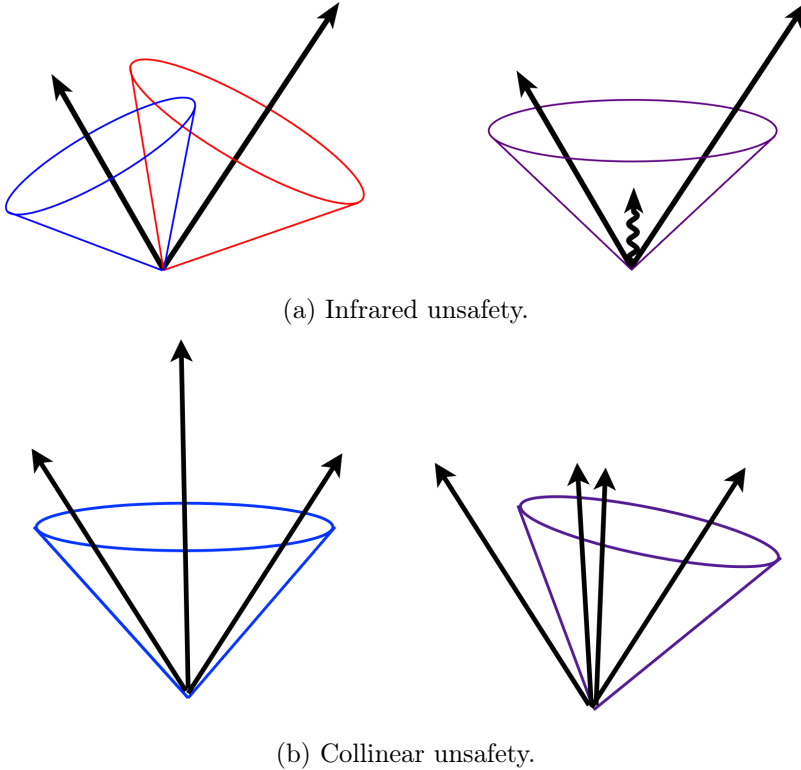


Figure 2.4: Illustration of (a) infrared unsafety and (b) collinear unsafety of fixed cone jet algorithm. Figures taken from [44].

Here $\Delta R_{ij}^2 = (y_i - y_j)^2 + (\phi_i - \phi_j)^2$ and $p_{T,i}$, y_i and ϕ_i are respectively the transverse momentum, rapidity and azimuth of particle i . In addition to the radius parameter R , a new parameter p was introduced, to split k_t algorithms into three categories.

- $p = 1$ k_t algorithm,
- $p = 0$ Cambridge/Aachen algorithm,
- $p = -1$ anti- k_t jet-clustering algorithm.

These algorithms first find the minimum d_{min} of all d_{ij} and d_i . If d_{min} is in d_{ij} 's, the corresponding objects i and j are recombined into a new object k using four-momentum recombination (see Section 2.3.3). Both objects i and j are removed from the list, and the new object k is added to it. If d_{min} is in d_i 's, the object i is considered to be a jet by itself and is removed from the list.

This means, that all original input objects end up to be either part of a jet, or to be a jet by themselves. Contrary to the cone algorithms, described earlier, no objects are shared between jets and the procedure is both infrared and collinear safe.

ATLAS uses anti- k_t jet algorithm with $R = 0.4$ for narrow and $R = 0.6$ for wide jets. Clustering of calorimeter signal towers (see Section 2.3.4) into jets is for k_t and anti- k_t algorithms shown in Figure 2.5. More information, about differences between k_t algorithms, can be found, for example, in Reference [45].

2.3.3 Recombination

Let J be the index set of the input objects with the defined four-momenta $(E^i, p_x^i, p_y^i, p_z^i)$, $i \in J$ which has to be recombined into the jet with new kinematic quantities E^J , \mathbf{p}^J , p_T^J , y^J , ... Possible recombination schemes are

- **Snowmass Scheme**

Used by fixed cone algorithm when finding proto-jets.

$$E_T^J = \sum_{i \in J} E_T^i \quad , \quad \eta^J = \frac{1}{E_T^J} \sum_{i \in J} E_T^i \eta^i \quad , \quad \phi^J = \frac{1}{E_T^J} \sum_{i \in J} E_T^i \phi^i. \quad (2.5)$$

- **Four-Momentum Recombination (E-Scheme)**

Used by k_t -algorithms and by fixed cone algorithm to final recombination of proto-jets into jets.

$$p^J = (E^J, \mathbf{p}^J) = \sum_{i \in J} (E^i, p_x^i, p_y^i, p_z^i), \quad (2.6)$$

$$p_T^J = \sqrt{(p_x^J)^2 + (p_y^J)^2} \quad , \quad y^J = \frac{1}{2} \ln \frac{E^J + p_z^J}{E^J - p_z^J} \quad , \quad \phi^J = \tan^{-1} \frac{p_y^J}{p_x^J}. \quad (2.7)$$

2.3.4 Calorimeter jets

The ATLAS calorimeter system, with $\sim 200,000$ individual cells, is the most important detector system for the jet reconstruction. Calorimeter cells differ in sizes, geometries, as well as in readout technologies, and for jet algorithms, these cells have to be firstly combined into larger objects, having physically

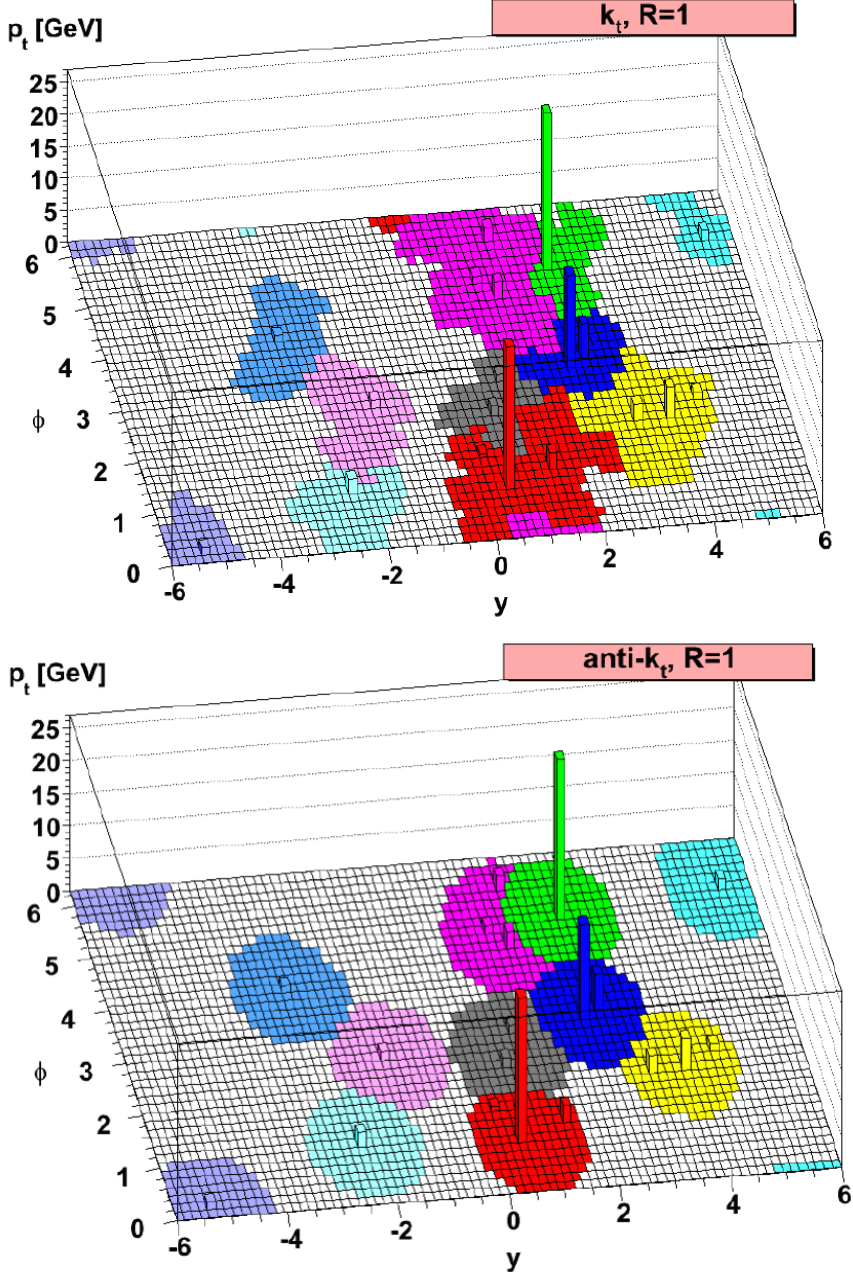


Figure 2.5: Illustration of k_t (top) and anti- k_t (bottom) jet algorithms with $R = 1$ for calorimeter signal towers in azimuthal angle ϕ and pseudorapidity y . Towers of the same color were clustered into one jet. Figures taken from [44].

meaningful four-momenta. The two concepts available are the calorimeter signal towers and the topological cell clusters, which I will describe shortly.

In the case of calorimeter signal towers, the cells are projected onto a fixed grid in pseudorapidity η and azimuth ϕ . The tower bin size is $\Delta\eta \times \Delta\phi = 0.1 \times 0.1$ in the whole acceptance region of the calorimeters, i.e. in $|\eta| < 5$ and $-\pi < \phi < \pi$ with approximately $100 \times 64 = 6400$ towers in total.

The second possibility, how to combine calorimeter cells into a larger objects, are the topological cell clusters, which are an attempt to reconstruct a three-dimensional "energy blobs" created by each of the particles entering the calorimeter. The clustering starts with a seed cells with a signal-to-noise ratio, or signal significance $\Gamma = E_{cell}/\sigma_{noise,cell}$, above a certain threshold S , for example $|\Gamma| > S = 4$. All directly neighboring cells of these seed cells, in all three dimensions, are collected into the cluster. Neighbors of neighbors are considered for those added cells which have Γ above a certain secondary threshold N , for example $|\Gamma| > N = 2$. Finally, a ring of guard cells with signal significances above a basic threshold $|\Gamma| > P$ is added to the cluster. After the initial clusters are formed, they are analyzed for local signal maxima by a splitting algorithm, and split between those maxima.

2.4 Jet corrections

Before jets can proceed to the data analysis, corrections have to be applied to minimize detector effects including calorimeter non-compensation, noise, losses in dead material and cracks, longitudinal leakage and particle deflection in the magnetic field. Indispensable tool for jet corrections are Monte Carlo event generators - PYTHIA8 [46] generating high-energy-physics events and GEANT4 [47] or ATLFastII [48] detector simulations for simulating the ALTAS detector response of PYTHIA8 generated events.

Using these tools, it is possible to reconstruct jets from Monte Carlo events on three different stages of collision indicated in Figure 2.6. Firstly, there are parton jets, which are reconstructed from the quarks, gluons and other elementary particles created just after the collision. Stable particles (with lifetime $c\tau \sim 10^{-15}$ m), created by hadronization, are recombined into the truth jets. When a collision reaches the detector, the detector simulation is used and the recorded signal is reconstructed into reco jets. The objective of the jet corrections is to find universal prescription, how to modify a reco

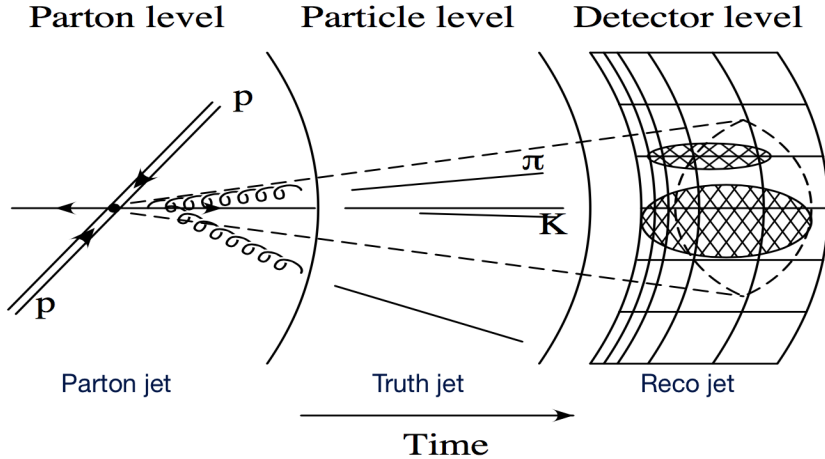


Figure 2.6: Three levels of jet reconstruction. Figure taken from [49]

jet properties, to observables derived from detector level, correspond to the observables on particle level.

Firstly, the reco jets are corrected to the truth jets leading to a modification of kinematic properties of the individual reco jet in the process called jet energy scale calibration. There are, however, some detector effects, which can not be fixed by this calibration. These effects include the limited detector resolution (detector cells have finite dimensions) and the limited acceptance (not all events are recorded). The former leads to the smearing of jet kinematic properties, whereas the later to decrease of observed cross section against the cross section theoretically expected. Both of these effects are negatively affecting the observables and can be partially removed by the unfolding procedure, which, unlike the jet calibration, is analysis dependent.

2.4.1 Jet Energy Scale Calibration

Energy E_{reco} of the jet measured by the detector may differ from the energy E_{truth} of the corresponding particle jet. The goal of the jet energy scale calibration is to remove some detector effects and correct E_{reco} to E_{truth} . The detector effects can be summarized by the formula

$$E_{truth} = \frac{E_{reco} - O}{R \cdot S}, \quad (2.8)$$

where the following corrections was defined

- **Offset O**

Represents the subtraction of additional energy, which is represented by the detector noise and pile-up with contributions from other proton-proton collisions, occurring during beam crossing.

- **Response R**

Describing a fraction of a truth energy, which was measured by the detector. Thanks to the hadronic character of jets observed at the LHC, this is the largest correction.

- **Showering S**

Characterizing particle flow out/from jet recombination cells.

More concise information about the parameters, just introduced, can be found in [49].

Because the calibration is persistently evolving, each jet analysis uses as an input the uncalibrated reco jets, which are then easily calibrated using standard APPLYJETCALIBRATION library [50].

2.4.2 Theory of Unfolding

In this analysis, the distribution $f(p_T)$ of inclusive jet p_T is measured for $p_T \in \langle a, b \rangle$. Due to the detector imperfections, instead of physical variable p_T , a new variable x and its distribution $g(x)$ are measured. The measured distribution can be expressed as

$$g(x) = \int_a^b A(x, p_T) f(p_T) dp_T, \quad (2.9)$$

with the function $A(x, p_T)$ describing the detector response, as it can be seen, when the detector is exposed to a particle beam with well known $p_T = p'_T$, meaning $f(p_T) = \delta(p_T - p'_T)$, leading to $g(x) = A(x, p'_T)$. The reconstruction of $f(p_T)$ from measured $g(x)$ is called unfolding.

For practical purposes, the equation (2.9) should be discretized, so, instead of continuous distribution $g(x)$, the discretized values $g_i = \int_{N(i)} g(x) dx$ of discretized observable $f_i = \int_{N(i)} f(p_T) dp_T$ are measured. Here, the integration is done over measurable $N(i) \subset \langle a, b \rangle$. For simplicity, assume $x \in \langle a, b \rangle$ is discretized in the same way as the physical p_T . Equation (2.9) then reads

$$g = Af, \quad (2.10)$$

with g and f being vectors of g_i 's and f_i 's respectively and A matrix derived from $A(x, p_T)$. This matrix is later, in Section 3.3, called the transfer matrix. If the limited acceptance would be the only detector problem, then A would be a diagonal matrix with some elements < 1 . When the limited resolution comes to play, the diagonal entries start to smear out of the diagonal and the matrix A starts to complicate.

The unfolding results which offers the solution of (2.10) by the inversion of matrix A , are mostly disappointing, as is illustrated e.g. in [51]. To improve results, different unfolding methods were developed. These include Iterative Bayesian Unfolding [52], Singular Value Decomposition [53], or Iterative, Dynamically Stabilized (IDS) method [54], which is the method, I have used in this thesis.

Chapter 3

Data Analysis

In physics, you don't have to go around making trouble for yourself - nature does it for you.

Frank Wilczek

QCD jets are the most common hard objects observed at inelastic collisions at hadron colliders, with their cross section exceeding any other physics process by orders of magnitude. Measurement of inclusive jet cross section provides the test for both QCD predictions and the detector performance up to the momentum transfers not reachable by any other physics processes.

In this Chapter, I will describe the details of the double differential inclusive jet cross section analysis, which I have done in this thesis. I will begin with the characteristics of the Monte Carlo data, I have used. These data together with the event selection criteria and matching procedure, which description will follow, fully specify the input for the unfolding procedure. Two approaches to the unfolding, which I have implemented in this thesis, will be described and compared with each other.

At the end of this Chapter, I will compare the results of my data analysis, with the next-to-leading order perturbative QCD prediction of my supervisor.

JZXW	p_T range (GeV)	Cross-section (fb)	Filter Efficiency	# events
JZ0W	0 - 20	7.8420e+13	9.7193e-01	3498000
JZ1W	20 - 80	7.8420e+13	2.7903e-04	2998000
JZ2W	80 - 200	5.7312e+10	5.2261e-03	500000
JZ3W	200 - 500	1.4478e+09	1.8068e-03	499500
JZ4W	500 - 1000	2.3093e+07	1.3276e-03	477000
JZ5W	1000 - 1500	2.3793e+05	5.0449e-03	499000
JZ6W	1500 - 2000	5.4279e+03	1.3886e-02	493500
JZ7W	2000 +	9.4172e+02	6.7141e-02	497000

Table 3.1: The cross-sections (XS), filter efficiency (FE) and number of events for the JZXW samples, which differ in the leading truth jet p_T range.

3.1 Data Characteristics

As the input, I have used Monte Carlo generated events of proton-proton collisions at the center-of-mass energy $\sqrt{s} = 13$ TeV with PYTHIA8 [46] event generator using CT10 Parton Distribution Functions [55] and ATLAS Underlying Event Tune AU2 [56]. QCD calculations are done only to the leading order in PYTHIA8, so the initial hard scattering is always simulated as $2 \rightarrow 2$ process. The response of the ATLAS detector on these events was simulated with GEANT4 [47] full detector simulation.

Particles were recombined into jets using anti- k_t jet algorithm with parameter $R = 0.4$. There are particle jets, reconstructed from the PYTHIA8 output, which, further in this thesis, are denoted truth jets, and, next to them, there are reco jets, reconstructed from the output of GEANT4 detector simulation from the ATLAS detector topological cell clusters.

The events were generated in slices according to the leading truth jet p_T . These samples differ in an event weight, which is for the whole event calculated as

$$\text{weight} = \frac{(\text{XS}) \cdot (\text{FE}) \cdot w_0}{(\# \text{ events})}, \quad (3.1)$$

with XS being cross-section, FE filter efficiency and w_0 additional weight factor stored in `EventInfoAux` container. Concrete values for datasets used in this theses are given in Table 3.1.

I have calibrated reco jets using the `APPLYJETCALIBRATION` [50] library v3.28 with configuration `JES_Prerecommendation2015_Feb2015.config` and

calibration sequence `JetArea_Residual_EtaJES`. In next, reco jets denote the reco calibrated jets.

In the analysis, I am using jets with transverse momentum $p_T > 15 \text{ GeV}$ and rapidity $|y| < 4$. Analysis is done in double binning in p_T and $|y|$, with the edges being the same as those in the analysis from 2011/2012 [57], which has chosen the binning in p_T to uncertainty in each bin was approximately one half of p_T resolution for jets within the bin.

$$\begin{aligned} p_T = & 15 - 20 - 25 - 35 - 45 - 55 - 70 - 85 - 100 - 116 - 134 - 152 - \\ & 172 - 194 - 216 - 240 - 264 - 290 - 318 - 346 - 376 - 408 - \\ & 442 - 478 - 516 - 556 - 598 - 642 - 688 - 736 - 786 - 838 - \\ & 894 - 952 - 1012 - 1076 - 1162 - 1310 - 1530 - 1992 - 2300 - \\ & 2800 - 3400 - 4100 - 5000 - 6000 - 7200 \text{ GeV}, \\ |y| = & 0.0 - 0.5 - 1.0 - 1.5 - 2.0 - 2.5 - 3.0 - 3.5 - 4.0. \end{aligned} \quad (3.2)$$

3.2 Event Selection

In this Section, I describe the selection and the matching criteria, I have used in my analysis. The former is needed to cut those jets (or those events) off, which were misinterpreted by the detector. By the later, the pairs, each containing one reco and one truth jet, are created. This provide the inputs for the unfolding procedure, which is the subject of the next Section.

More details, including graphical display and numerical results for procedures described in this Section, are given in Appendix A.

3.2.1 Jet Cuts

I have implemented four jet cuts, which description follows. First two of these cuts are needed to remove jets, with p_T or rapidity y out of used binning. The objective of the remaining cuts is to remove the events, which were badly reconstructed by the detector.

- **p_T Cut**

Reco and truth jets with $p_T > 15 \text{ GeV}$ were kept.

- **y Cut**

Reco and truth jets with $|y| < 4$ were kept.

- **Zero jet (0-jet) Cut**

Only those events which has at least one reco and one truth jet are considered.

- **Leading Ration (LR) Cut**

In this cut the reco and truth jets with the highest p_T were used. If there was only one reco jet left, the ratio $LR = p_{T,leading}^{reco}/p_{T,leading}^{truth}$ was calculated. If there were two reco jets, instead of $p_{T,leading}^{reco}$ the average p_T of two leading reco jets was calculated. If $0.6 < LR < 1.4$ the event is considered.

Numbers of reco and truth jets, removed in each step, are shown in Table A.1, where also the cut efficiencies for individual JZ samples are shown. The impact of each cut on jet p_T spectrum of reco and truth jets is displayed in Figure A.1.

It can be seen, that the most important cut is the 0-jet cut, which removes approximately 80 % of reco jets in JZ0W sample, whereas the truth jets remain intact. According to Table 3.1, the leading truth jet $p_T < 20$ GeV for event from the JZ0W sample, which has no longer to hold for reco jets, which were, in some cases, reconstructed with $p_T \sim 100$ GeV. Because of Monte Carlo event weight for events from JZ0W sample is dominant over event weights of other JZ samples by several orders, the misreconstructed reco jets from JZ0W sample were negatively influencing the observed p_T spectrum of reco jets, as can be seen from top of the Figure A.1.

3.2.2 Jet Matching

To find, how the truth jets are reconstructed by the detector, the jet matching has to be done, i.e. for each truth jet it is needed to find corresponding reco jet. In this thesis, I have used the matching based on minimal angular distance between matched jets, and its description follows in this Section.

For each pair (i, j) of reco and truth jets, the quantity $dR_{ij} = \sqrt{d\phi_{ij}^2 + dy_{ij}^2}$ was calculated, with $d\phi_{ij}$ being the angle between ϕ_i^{reco} and ϕ_j^{truth} and $dy_{ij} = y_i^{reco} - y_j^{truth}$. The minimum was found between all of dR_{ij} 's. If this was smaller than the defined cutoff $\min(dR_{ij}) = dR_{pq} < dR^{cutoff} = 0.2$,

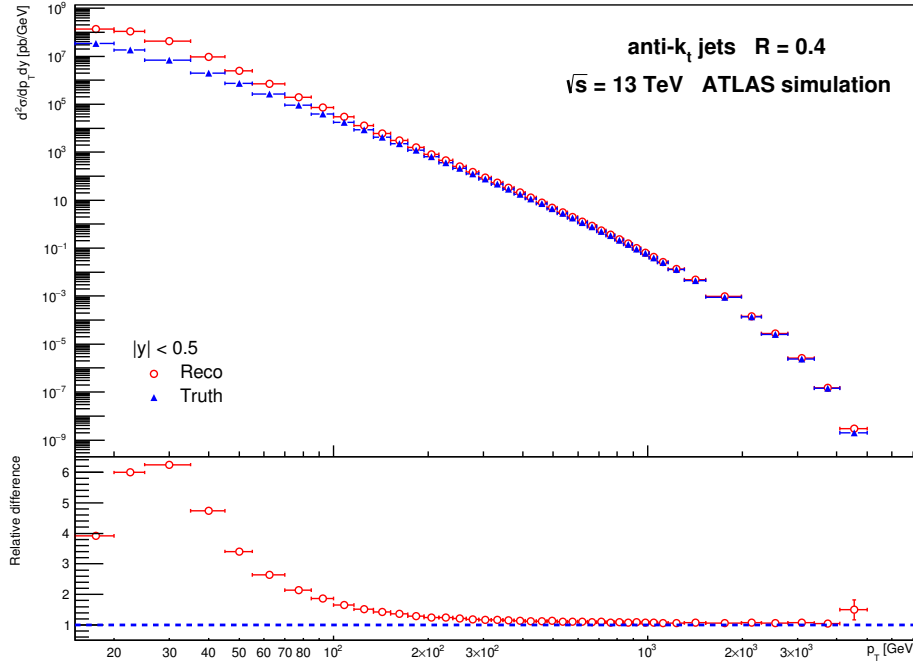


Figure 3.1: Comparison of p_T spectra of reco and truth jets, after event selection, for selected $|y| < 0.5$ rapidity bin. Each p_T bin was divided by its width, so y -axis has physical meaning of double differential cross section in p_T and y . Bottom graph contains the relative difference between reco and truth spectra.

the jets (p, q) were matched and further not assumed in the matching procedure. This continued until condition $\min(dR_{ij}) < dR^{cutoff}$ was not satisfied or all of the reco or truth jets were matched.

Numbers of reco and truth jets, both matched and unmatched, are shown in Table A.1, where also the matching efficiencies for individual JZ samples are shown. Figure A.2 shows the p_T spectra of truth and reco jets after event selection, which are composed from p_T spectra of matched and unmatched jets, which are in the Figure A.2 shown also. p_T spectra of truth and reco jets are for all rapidity bins, assumed in this thesis, shown in Figure A.3.

3.3 Unfolding

After the four cuts from the Section 3.2.1, the sets of jets, denoted reco and truth jets, were obtained. Matching procedure, described in the Sec-

tion 3.2.2, divided both reco and truth jets into two categories, depending on successful matching - there is correspondence 1 : 1 between matched reco and matched truth jets. Reco jets, which were not matched, formed the unmatched reco jets, and, similarly, a set of unmatched truth jets was created. All these 6 sets of jets are needed by the unfolding procedure, which I describe in this Section.

From the Figure 3.1, showing the p_T spectra of reco and truth jets, it can be seen, that observed p_T spectrum, represented by the reco jets, differs from the p_T spectrum theoretically expected, which is represented by the p_T spectrum of truth jets. Unfolding should transform the observed p_T spectrum to the spectrum theoretically expected. If this transformation would be done on real data, it should, ideally, preserve additional structures, which are presented in data, but not included by the theory.

The main ingredient for the unfolding procedure is the transfer matrix A_{ij} , which contains the number of reco jets in bin i with a matched truth jets, which was generated in bin j , and describes thus the smearing effects of the detector. In this thesis, I use the double binning (3.2), which complicates the situation, because the matched reco jet can simply migrate of the transfer matrix from Figure 3.2, when, for example, its rapidity $|y| > 0.5$ and when it was matched with a truth jet with $|y| < 0.5$ or vice versa. In this thesis, I test two unfolding approaches, which offer the dealing with double binning.

1. Simple unfolding

In this case, only those reco and truth jets are used in the transfer matrix, which were matched within the same rapidity bin. Remaining matched jets are added to the unmatched jets. Eight transfer matrices 46×46 are filled (one for each rapidity bin, $46 = \text{number of } p_T \text{ bins}$) and unfolding is done for each of these matrices separately. One of these matrices, for $|y| < 0.5$ rapidity bin, is shown in Figure 3.2.

2. 2D unfolding

In this case, the unfolding matrix is redefined, to encapsulate the matching of jets between different rapidity bins. In this case, only one transfer matrix 368×368 is created ($368 = 46 \times 8$), with unfolding being done only for this matrix, shown at Figure 3.3, from which the way, how the transfer matrix was redefined from the simple unfolding approach, should follow.

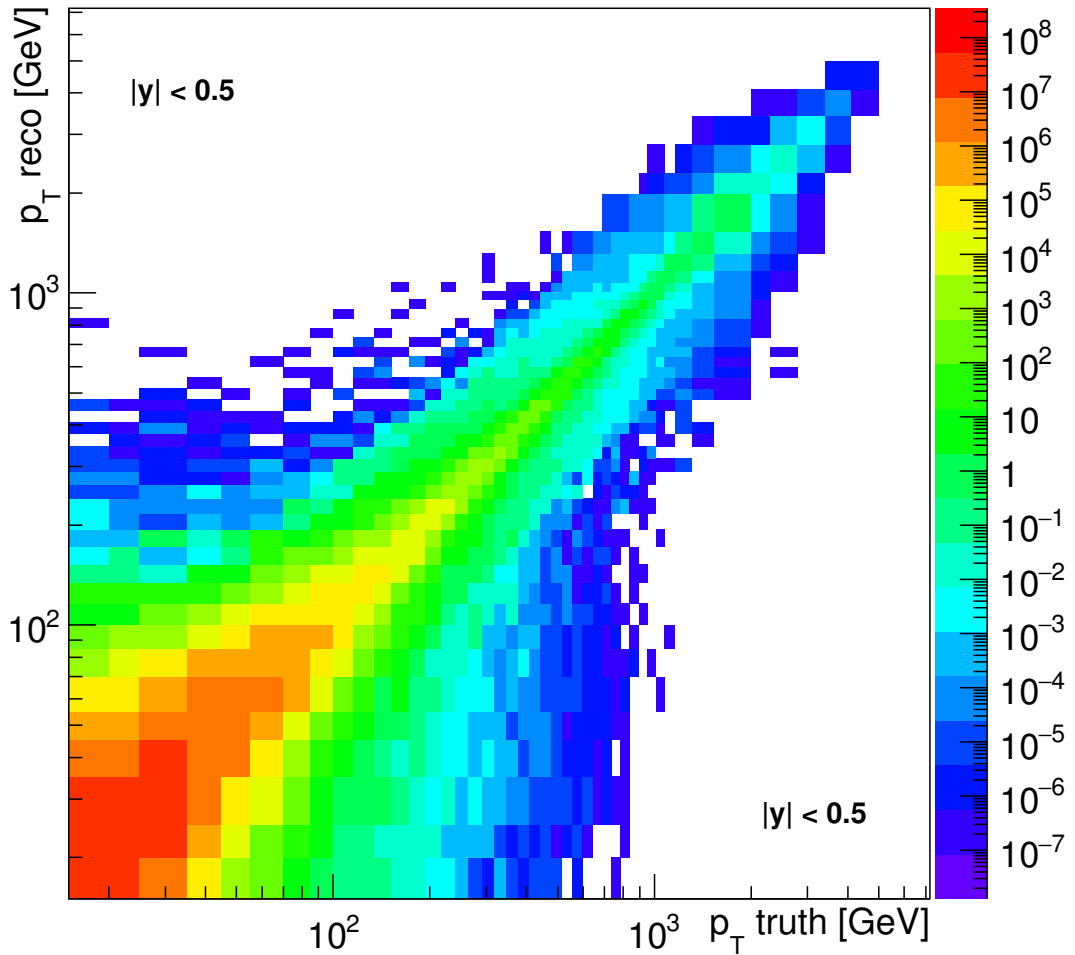


Figure 3.2: Unfolding matrix for matched reco and truth jets with rapidity $|y| < 0.5$, corresponding to one of eight transfer matrices used by the simple unfolding approach. Each cell is proportional to the number of jets with truth p_T in range determined by the x -axis, which were reconstructed to the reco jets with p_T determined by the y -axis. White space signalize no input.

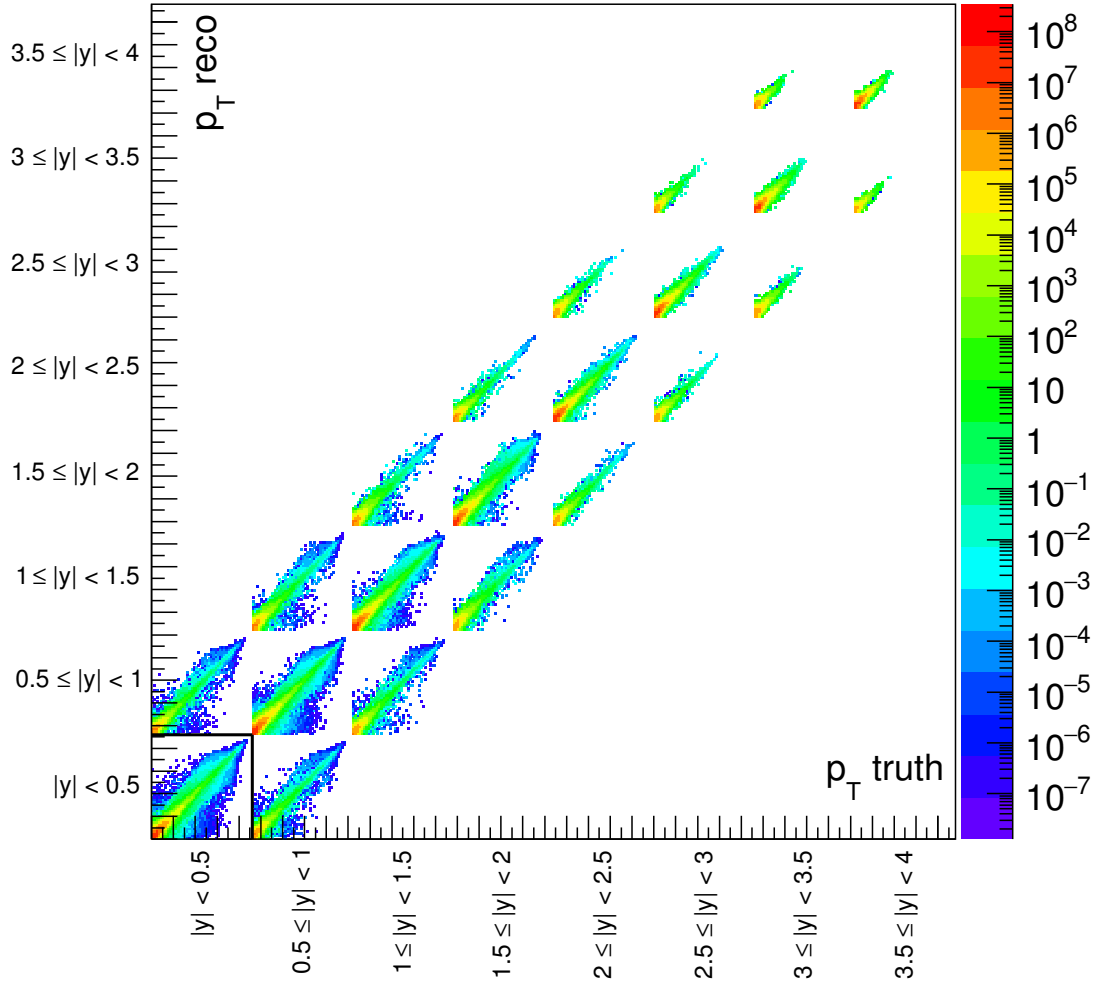


Figure 3.3: Transfer matrix used by the 2D unfolding approach. Each cell is proportional to the number of jets with truth p_T and rapidity y determined by the x -axis, which were reconstructed to the reco jets with p_T and y determined by the y -axis. Marked square in $|y| < 0.5$ region is the matrix shown in Figure 3.2. Projection of this matrix on the x and y -axis corresponds to the p_T spectrum of matched truth and reco jets for corresponding rapidity bin respectively. For better understanding of structure of this matrix, I have created some slices, which are shown in Appendix B.2.

Transfer matrix from Figure 3.3, used by the 2D unfolding approach, contains 8 submatrices at the diagonal, which are the transfer matrices used by the simple unfolding approach. Next to these submatrices, transfer matrix of 2D unfolding approach contains 14 additional submatrices beside the diagonal. These correspond to the matched jets with migration in rapidity bins, and in case of simple unfolding approach, these jets are assumed to be unmatched. To better understand the structure of transfer matrix of 2D unfolding approach, I have created slices through it, which are shown in Appendix B.2.

It can be seen, from the slices, that the dominant elements of each of the submatrices are on the main diagonal, which correspond to the fact, there is no significant bias in p_T reconstruction. The finite p_T resolution causes the smearing of the diagonal and a finite rapidity resolution is the cause of the presence of 14 minor submatrices. Next, it can be seen, that the elements of the minor submatrices are approximately two orders in magnitude smaller, than the corresponding submatrix on the main diagonal. This means, that the migration of matched jets in rapidity is much smaller, than the migration in p_T .

Next to the transfer matrix, numbers of matched and unmatched reco and truth jets are needed, for each (y, p_T) bin, by unfolding procedure. These serve for calculation of matching efficiencies, which are the key ingredient in the first and in the last step of the unfolding procedure. Matching efficiencies, for $|y| < 0.5$ rapidity bin, are for both simple and 2D unfolding shown in Figure 3.4 and for other rapidity bins, they are shown in Appendix B.1.

Unfolding procedure can be divided into three main steps

1. Input data are multiplied by the matching efficiencies of reco jets.
2. Transfer matrix is used to correct data spectrum for detector effects. For this purpose, the Iterative Dynamical Stabilized (IDS) [54] unfolding method was implemented, which uses the series of iterations to improve unfolding results. In this thesis, I have iterated once.
3. The spectrum obtained by the step 2 is divided by the matching efficiencies of truth jets, in order to correct resulting spectrum for the unmatched truth jets.

Figure 3.5 shows the comparison of p_T spectra of reco jets and unfolded

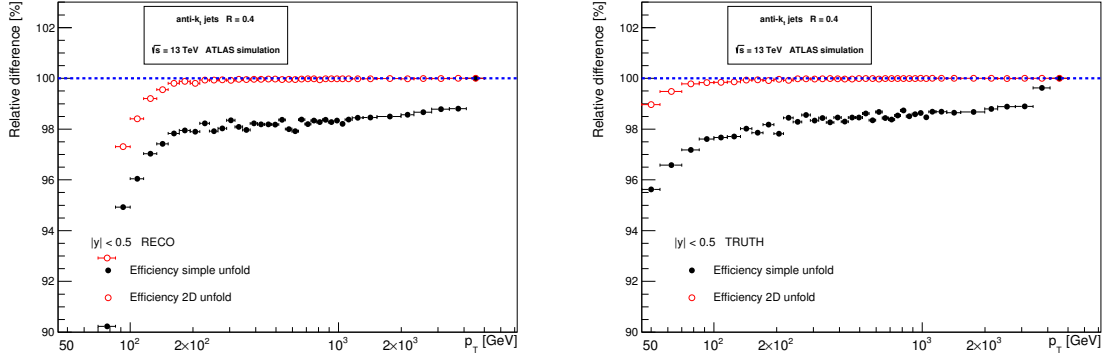


Figure 3.4: Comparison of matching efficiencies of simple and 2D unfolding approaches for $|y| < 0.5$ rapidity bin. Matching efficiencies are compared for both reco jets (left) and truth jets (right). Matching efficiencies for all rapidity bins are shown in Appendix B.1.

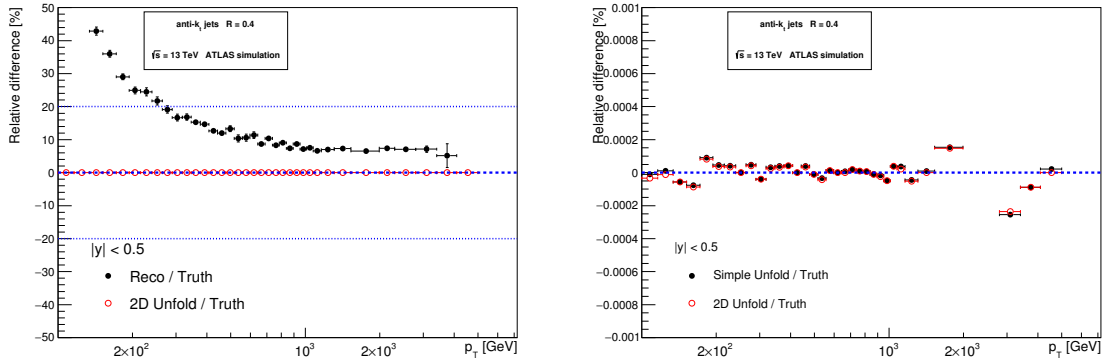


Figure 3.5: Comparison of p_T spectra of reco jets and the unfolded p_T spectra (2D unfolding approach) with the p_T spectra of truth jets on the left. The graph on the right shows the comparison of unfolded spectra, obtained by the 2D and simple unfolding approaches, with the p_T spectra of truth jets. Both graphs are for $|y| < 0.5$ rapidity regions. Results for all rapidity bins are shown in Appendices B.3, B.4.

spectrum (by 2D unfolding approach) with the p_T spectrum of truth jets on the left. The right part of the Figure 3.5 contains the comparison of simple and 2D unfolded spectra with the spectrum of truth jets for $|y| < 0.5$ rapidity bin. Results for all rapidity bins are shown in Appendix B.3.

From figures it follows, the unfolding procedure corrects the p_T spectrum of reco jets to p_T spectrum of truth jets up to the systematic error $< 10^{-3}\%$ and that the differences between results from simple and 2D unfolding approaches are even smaller.

3.4 Comparison with NLO Prediction

In the previous Sections, I have described the jet calibration and the unfolding procedure. These serve to remove the detector imperfections and correct the p_T spectrum of reco jets to the p_T spectrum of truth jets. This was done using the events generated by PYTHIA8, which uses the leading order QCD calculations to simulate the initial proton-proton collision. Nowadays the QCD predictions are tested up to next-to-leading order and for LHC Run II, new calculations, assuming next-to-next-to-leading order QCD processes, are preparing [58, 59].

My supervisor has determined the theoretical prediction of p_T spectra of parton jets using NLOJET++ program v4.1.2 [60]. This program computes the QCD processes up to next-to-leading order with CT10 parton distribution functions [55, 61]. In this thesis, I have used his computations for center-of-mass energies $\sqrt{s} = 8\text{ TeV}$ and $\sqrt{s} = 13\text{ TeV}$, the first corresponding to the LHC Run I and the second to the LHC Run II.

In this Section, I compare the truth jet p_T spectrum from PYTHIA8 with the theoretical prediction of parton jet p_T spectrum from next-to-leading order QCD predictions of my supervisor.

Firstly, I have compared the next-to-leading order predictions for two different center-of-mass energies of proton-proton collisions. The comparison is shown, for $|y| < 0.5$ rapidity region, in Figure 3.6, where next to the double differential cross section, the expected numbers of jets, observed in the LHC Run I and II, are shown. The numbers were obtained by multiplying each bin by its width and by the luminosities of Run I (20 fb^{-1}) and expected luminosity for Run II (100 fb^{-1}) respectively. Comparisons for other rapidity bins are shown in Appendix C.1.

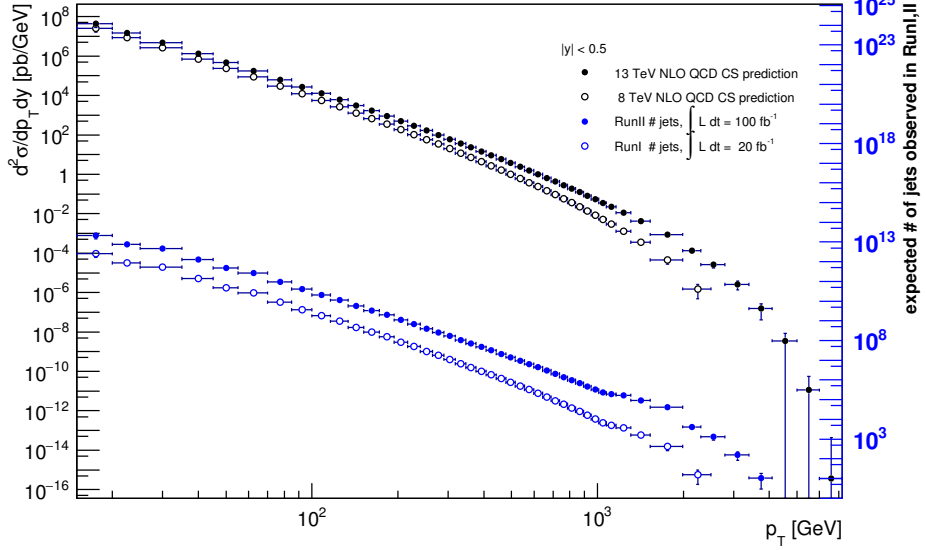


Figure 3.6: Comparison of next-to-leading order QCD predictions of double differential inclusive jet cross section (black) for proton-proton collisions at $\sqrt{s} = 13$ TeV (filled circles), corresponding to the LHC Run II, and $\sqrt{s} = 8$ TeV (empty circles), corresponding to the LHC Run I. The cross section is multiplied by integrated luminosities and bin width in p_T , to obtain the expected numbers of jets observed in each p_T bin (blue). Figure shows only $|y| < 0.5$ rapidity bin, remaining rapidity bins are shown in Appendix C.1.

It can be seen, that the increase in the center-of-mass energy is the most significant for jets with high p_T .

In the next-to-leading theoretical computations, several uncertainties are taken into account. In this thesis, I assume the following uncertainties

- **Scale uncertainty**

Coming from the choice of renormalization and factorization scales, including neglecting the higher order terms beyond next-to-leading order

- **α_S uncertainty**

Because α_S is experimentally determined with uncertainty.

- **PDF uncertainty**

Prediction depends on the concrete choice of a Parton Distribution Function.

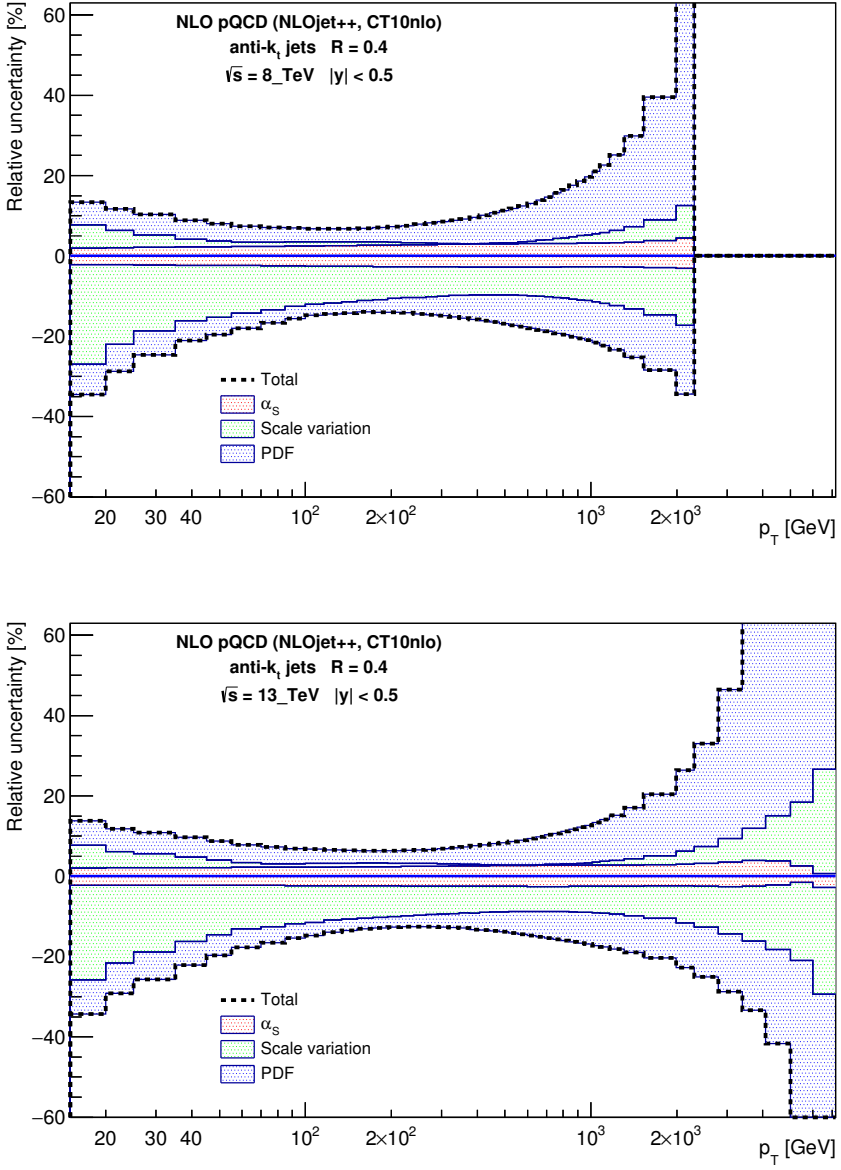


Figure 3.7: Theoretical uncertainties for next-to-leading order QCD predictions of inclusive jet double differential cross section for proton-proton collisions at $\sqrt{s} = 8\text{ TeV}$ (top) and $\sqrt{s} = 13\text{ TeV}$ (bottom) for $|y| < 0.5$ rapidity bin. Uncertainties for other rapidity bins are shown in Appendix C.2.

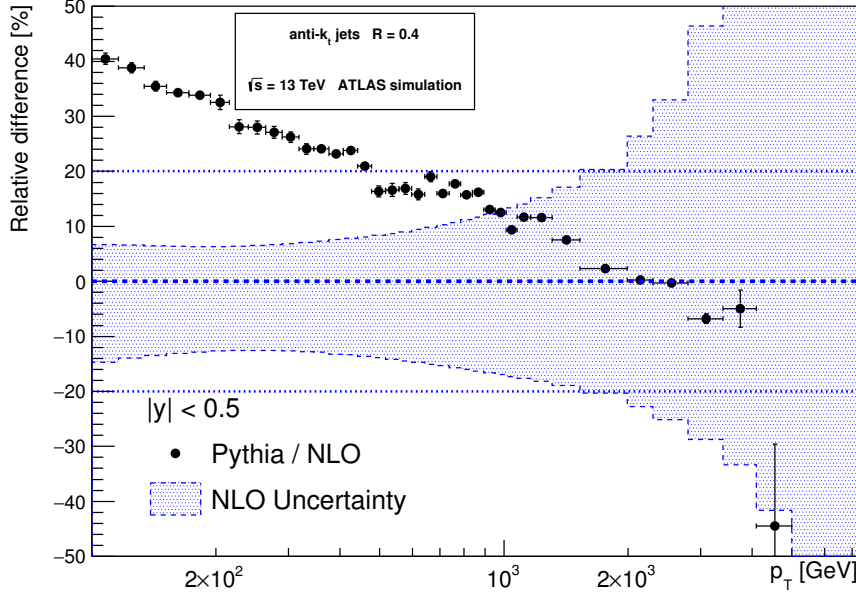


Figure 3.8: Comparison of PYTHIA8 prediction with next-to-leading order QCD prediction of inclusive jet double differential cross section for $|y| < 0.5$ rapidity bin, with uncertainties of next-to-leading order QCD predictions symbolized by the blue area. Comparisons for other rapidity bins are shown in Appendix C.3.

There are, at least, two other uncertainties, which should be assumed, but according to the analysis from 2013 [57], the corrections coming from these uncertainties are not as significant as the three corrections mentioned already.

- **Nonperturbative corrections uncertainty**

Hadronization and Underlying Event corrections

- **Electroweak corrections uncertainty**

Next to the QCD processes, the electroweak processes has to be assumed.

These processes becomes more important, as the momentum transfer increases.

The corrections were extracted from the files with next-to-leading order QCD predictions, where each correction is represented by the set of equally

likely histograms, expressing the deviation from the default prediction. Corrections are, for $|y| < 0.5$ rapidity bin, shown in Figure 3.7, other rapidity bins are shown in Appendix C.2.

Comparison of p_T spectra of truth jets with next-to-leading order QCD prediction is, for $|y| < 0.5$ rapidity bin, shown in Figure 3.8, for other rapidity bins see Appendix C.3. It can be seen, that the truth p_T spectrum is for jets with low p_T greater, then the next-to-leading order QCD prediction, and that for a few p_T bins with the highest p_T , the situation is reversed.

Generally, there is a significant difference between leading order QCD prediction, which I have extracted from the p_T spectra of truth jets in PYTHIA8 generated events, and next-to-leading order QCD prediction, which my supervisor has calculated using the NLOJET++ program. The differences are greater then the theoretical uncertainties, successfully demonstrating the influence of next-to-leading order QCD processes, on observables.

Conclusion

This thesis deals with the measurement of the inclusive jet double differential cross section in p_T and rapidity in the ATLAS experiment. Inclusive jets are the prevailing objects created in the inelastic collisions at the Large Hadron Collider (LHC) with p_T covering range from a few GeV to a few TeV. Nowhere is the increase in the center-of-mass energy appreciated, as is in the case of inclusive jets, which can be seen from Figure 3.6. According to the preliminary analysis, the proton-proton collision in the LHC Run II with the center-of-mass energy $\sqrt{s} = 13$ TeV, could create thousands of jets with p_T in the interval $1 \text{ TeV} < p_T < 4 \text{ TeV}$.

Inclusive jets are theoretically straightforward and hence powerful test of perturbative Quantum Chromodynamics (QCD) and with wide range of momentum transfers, the inclusive jet cross section is sensitive to the properties of the running coupling constant α_S . Momentum transfers in orders of $\sim 1 \text{ TeV}$ will probe the structure of proton at small distance scales $\lambda \sim 1/p_T \sim \text{TeV}^{-1} \sim 10^{-19} \text{ m}$ and will contribute to our understanding of the proton structure (Parton Distribution Functions). If there is a new physics at these scales (such as the structure of quark), the inclusive jets may reveal it.

This thesis begins with a brief description of the QCD as one of the components of the Standard Model. My intention was to connect historical development of the QCD with definitions of its key concepts, which I am using later in this thesis. These concepts include the Parton Distribution Functions, running coupling constant α_S and Asymptotic Freedom and Color Confinement Phenomena. The first Chapter ends with the splitting of QCD into perturbative and non-perturbative regions.

The second Chapter starts with the description of the LHC with the ATLAS detector, and introduces the most important concept of this thesis

- a jet. Using the QCD, I am trying to explain the necessity of the jet on hadron colliders, and to define the jet itself. This is done by the definition of jet algorithms, which I am formulating with the emphasis on possible jet definition at three different stages of collision: at parton, particle and detector level. The second Chapter ends with the description of jet energy scale calibration and unfolding procedures, which objective is to reduce negative detector effects, to lower differences between jets at detector and particle levels.

The last Chapter of my thesis describes the analysis of the double differential inclusive jet cross section in p_T and rapidity. As the Run II data are not yet available, I have used, as the input, the PYTHIA8 generated events of proton-proton collisions with the center-of-mass energy $\sqrt{s} = 13$ TeV using CT10 Parton Distribution Functions and ATLAS Underlying Event Tune AU2. These data contains the jets reconstructed on particle and detector levels and as a jet algorithm, the anti- k_t jet algorithm with parameter $R = 0.4$, is used.

As the first step of my analysis, I describe the jet energy scale calibration, which is followed by the description of event selection criteria and jet matching procedure. To correct the reconstructed p_T spectrum on detector level, I implement two different approaches of data unfolding. A simple unfolding, the first of unfolding approaches, allows jet matching only within the same rapidity bins. In addition to the simple unfolding, I introduce a 2D unfolding, which allows matching between different rapidity bins. These approaches differ in definitions of transfer matrices and in matching efficiencies which are shown in Appendix B.1. It can be seen, the matching efficiencies, in case of simple unfolding approach, are $\sim 2 - 5\%$ worse than the matching efficiencies in 2D unfolding approach. This should cause the unfolded spectrum from 2D unfolding approach will be more precise than that of simple unfolding approach.

The results from both of the unfolding approaches are compared with the p_T spectrum of particle level jets in Appendix B.4. It can be seen, that in both cases, the unfolded p_T spectrum is in agreement with the p_T spectrum of particle level jets up to systematic error $< 10^{-3}\%$ and that the relative difference between two unfolding approaches is even smaller.

The second input, for my analysis, are the next-to-leading order perturbative QCD predictions of double differential inclusive jet cross section in

p_T and rapidity for center-of-mass energies $\sqrt{s} = 8 \text{ TeV}$ (corresponding to LHC Run I) and $\sqrt{s} = 13 \text{ TeV}$ (Run II). This predictions was calculated by my supervisor, using NLOJET++ program and the same parton distribution functions as PYTHIA8. The predictions include uncertainties in coupling constant α_S , Parton Distribution Functions and factorization and normalization scales. These uncertainties are shown in Appendix C.2.

Cross section predictions for $\sqrt{s} = 8 \text{ TeV}$ and $\sqrt{s} = 13 \text{ TeV}$ are compared in Appendix C.1, where the integrated luminosities $L = 20 \text{ fb}^{-1}$ (Run I) and $L = 100 \text{ fb}^{-1}$ (Run II expected) are used to calculate the expected numbers of jets observed in each p_T bin. It can be seen, that according to this prediction, in Run II we will observe ~ 1000 times more jets with $p_T > 1 \text{ TeV}$ than it was in Run I. In addition, the LHC Run II could create a few jets with $p_T \sim 4 \text{ TeV}$.

Next, I have compared the p_T spectrum of particle jets, obtained from PYTHIA8 generated events, which corresponds to the leading order QCD predictions, with p_T spectrum of parton jets from next-to-leading order QCD prediction in Appendix C.3. Only for few highest p_T bins the cross section predicted by the next-to-leading order QCD is bigger than that of PYTHIA8. The differences, which are greater than the theoretical uncertainties, successfully demonstrate the impact of next-to-leading order QCD processes on physical observables.

There are several ways to extend this analysis. Although this analysis is only preparation for the analysis of real data, which will be collected in the LHC Run II, the developed implementations of the IDS unfolding method could serve for unfolding of the real p_T spectra, measured by the ATLAS detector in Run II. The unfolding results could be further improved by the running on a new datasets generated by the PYTHIA8 with the usage of newer parton density functions.

The unfolding approaches introduced in this thesis could be probed further. One of the possibility is the event reweighting and checking, if the unfolding is not dependent on the shape of the p_T spectra. Next possibility is to compare, how the simple and 2D unfolding will deal with a new structure in data.

Appendices

Appendix A

Cut and Match Results

A.1 Cut Results

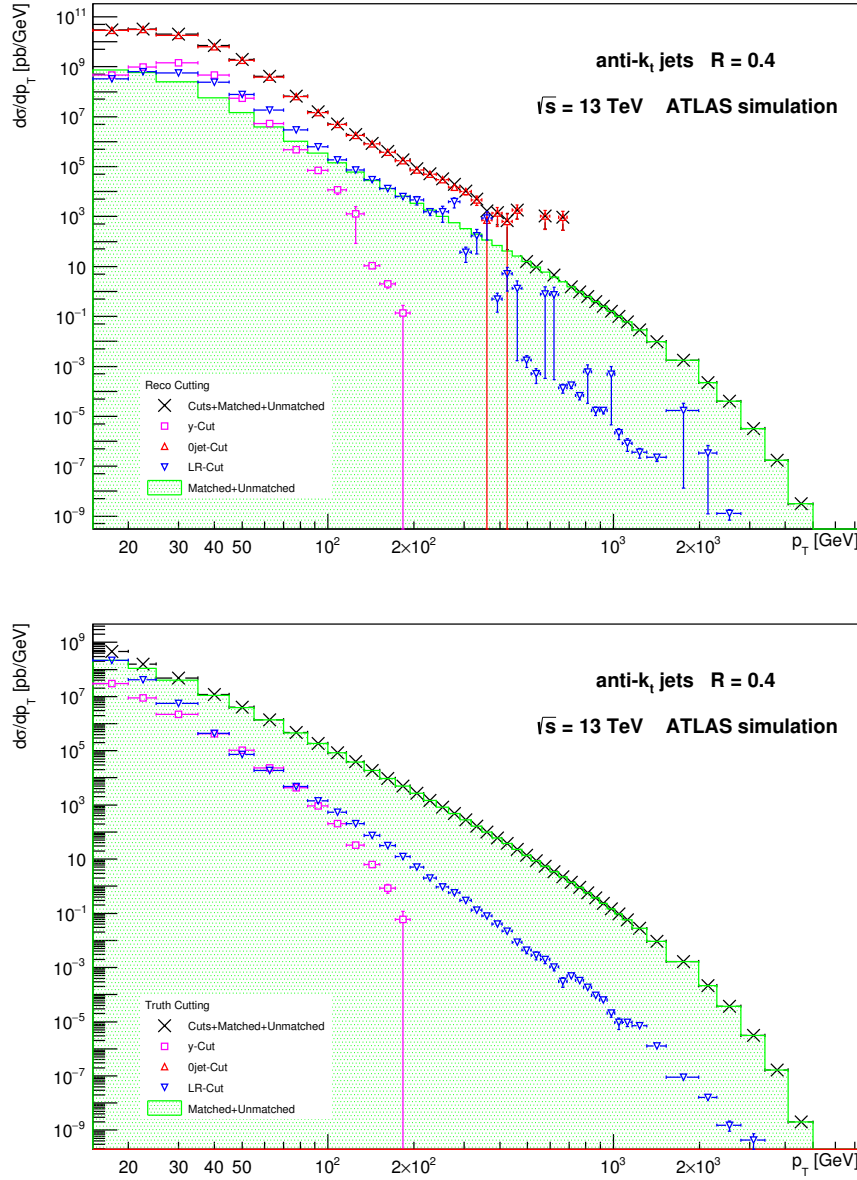


Figure A.1: Impact of 4 cuts, defined in Section 3.2.1, on differential cross section in p_T of reco jets (top) and truth jets (bottom). Black crosses represent the original uncutted spectrum, green area then p_T spectra after event selection. Jets were identified with ant- k_t jet algorithm with $R = 0.4$.

A.2 Match Results

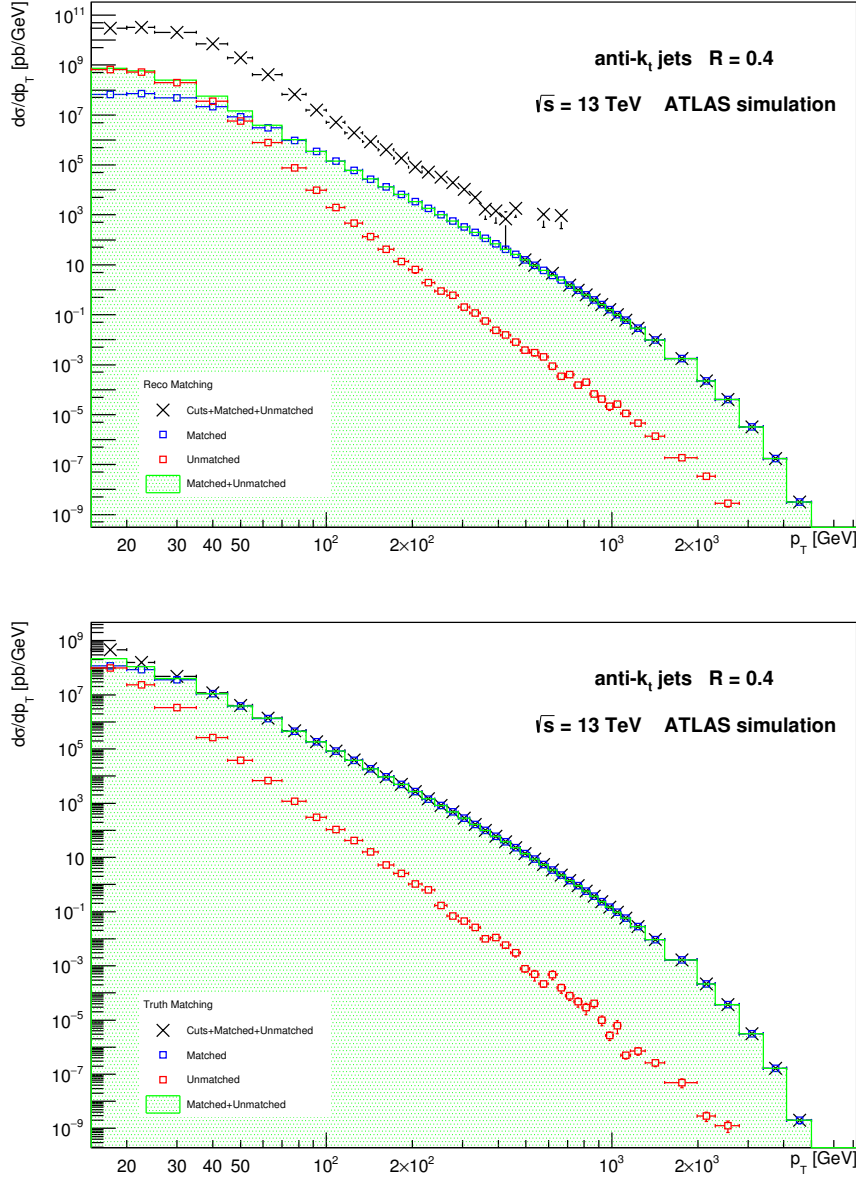


Figure A.2: Results of matching procedure described in Section 3.2.2 demonstrated on differential cross section in p_T of reco (top) and truth (bottom) jets. Black crosses represent the original p_T spectrum before event selection. The contribution of matched and unmatched jets to green area is shown. Jets were identified with anti- k_t jet algorithm with $R = 0.4$

A.3 Truth and Reco p_T Spectra

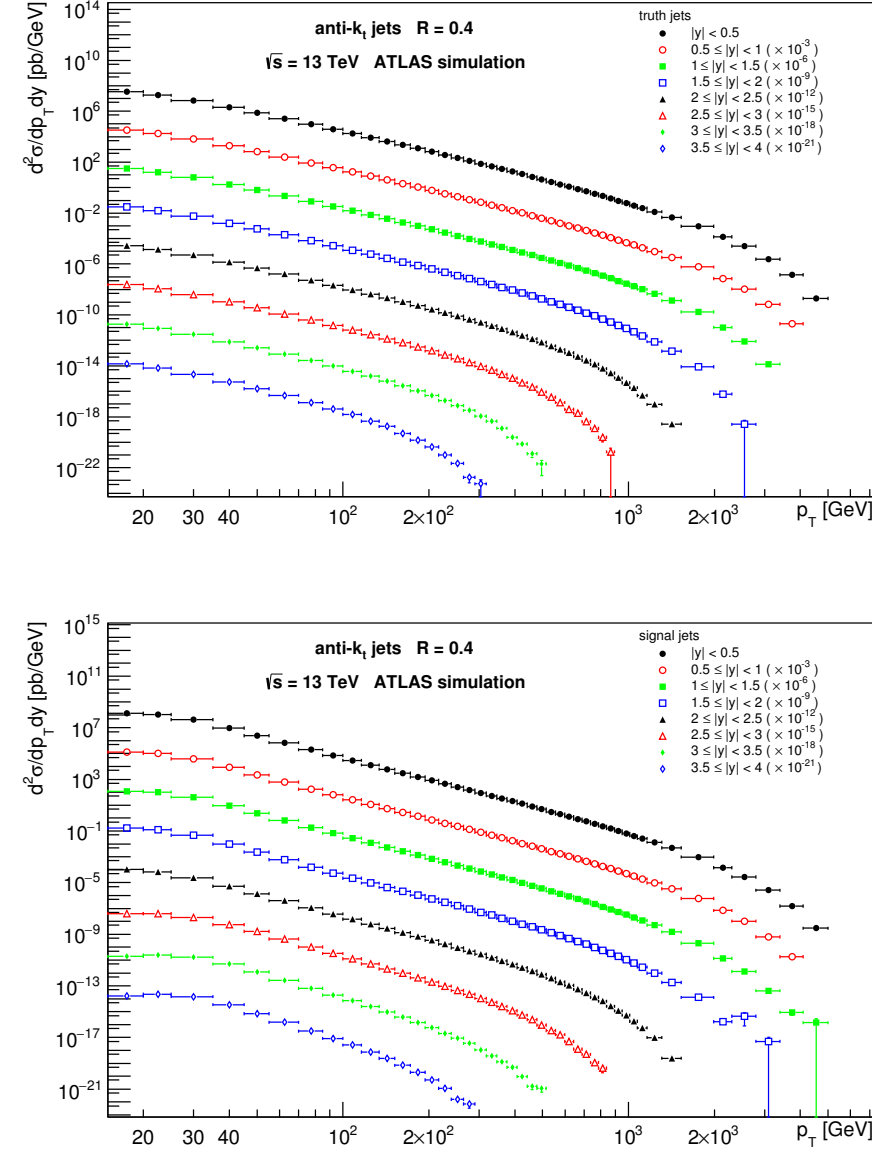


Figure A.3: Double differential inclusive jet cross section of truth (top) and reco (bottom) jets in p_T and rapidity y . For the convenience the cross sections for different rapidity bins are multiplied by the factor indicated in the legend. Jets were identified with anti- k_t jet algorithm with $R = 0.4$.

# jets	ALL	JZ0W	JZ1W	JZ2W	JZ3W	JZ4W	JZ5W	JZ6W	JZ7W
Reco	1.09e+08	3.11e+07	3.59e+07	6.67e+06	7.07e+06	6.28e+06	7.29e+06	7.13e+06	7.11e+06
Truth	7.28e+07	3.04e+06	3.00e+07	6.17e+06	6.91e+06	6.20e+06	6.98e+06	6.53e+06	6.25e+06
CutPt	Reco 9.36e+06 8.6 %	3.74e+06 12.0 %	3.13e+06 8.7 %	6.50e+05 9.7 %	5.87e+05 8.3 %	4.76e+05 7.6 %	5.48e+05 7.5 %	5.52e+05 7.7 %	5.63e+05 7.9 %
	Truth 4.70e+07 64.6 %	3.00e+06 98.7 %	2.20e+07 73.1 %	3.86e+06 62.6 %	4.00e+06 57.8 %	3.42e+06 55.1 %	3.74e+06 53.6 %	3.43e+06 52.5 %	3.23e+06 51.6 %
Cuty	Reco 3.43e+06 3.1 %	1.19e+06 3.8 %	1.29e+06 3.6 %	1.42e+05 2.1 %	1.28e+05 1.8 %	1.03e+05 1.6 %	1.16e+05 1.6 %	1.10e+05 1.5 %	1.08e+05 1.5 %
	Truth 5.06e+05 0.7 %	3.04e+03 0.1 %	3.19e+05 1.1 %	4.54e+04 0.7 %	3.79e+04 0.5 %	2.88e+04 0.5 %	2.78e+04 0.4 %	2.22e+04 0.3 %	1.83e+04 0.3 %
Cut0jet	Reco 2.64e+07 24.2 %	2.59e+07 83.2 %	5.70e+05 1.6 %	0.00e+00 0.0 %					
	Truth 0.00e+00 0.0 %	0.00e+00 0.0 %							
CutLR	Reco 4.09e+06 3.7 %	2.38e+05 0.8 %	3.82e+06 10.6 %	2.99e+04 0.4 %	7.07e+03 0.1 %	2.33e+03 0.0 %	1.63e+03 0.0 %	7.14e+02 0.0 %	6.31e+02 0.0 %
	Truth 5.40e+05 0.7 %	2.19e+04 0.7 %	4.96e+05 1.7 %	1.82e+04 0.3 %	4.45e+03 0.1 %	1.33e+03 0.0 %	9.03e+02 0.0 %	4.37e+02 0.0 %	2.78e+02 0.0 %
Matched	Reco 2.17e+07 19.8 %	7.62e+03 0.0 %	6.03e+06 16.8 %	1.95e+06 29.3 %	2.54e+06 36.0 %	2.46e+06 39.1 %	2.88e+06 39.5 %	2.78e+06 38.9 %	2.72e+06 38.2 %
	Truth 2.17e+07 29.8 %	7.62e+03 0.3 %	6.03e+06 20.1 %	1.95e+06 31.7 %	2.54e+06 36.8 %	2.46e+06 39.6 %	2.88e+06 41.3 %	2.78e+06 42.5 %	2.72e+06 43.5 %
Unmatched	Reco 4.42e+07 40.5 %	5.36e+04 0.2 %	2.10e+07 58.6 %	3.89e+06 58.4 %	3.81e+06 53.8 %	3.24e+06 51.6 %	3.75e+06 51.4 %	3.69e+06 51.8 %	3.72e+06 52.3 %
	Truth 3.07e+06 4.2 %	6.18e+03 0.2 %	1.25e+06 4.2 %	2.89e+05 4.7 %	3.20e+05 4.8 %	2.95e+05 4.8 %	3.29e+05 4.7 %	3.03e+05 4.6 %	2.88e+05 4.6 %

Table A.1: Statistics for matching and cutting procedures described in Sections 3.2.1 and 3.2.2 displayed for all jets as well as for individual JZ samples, which are defined in Table 3.1. At the top, the numbers of initial reco and truth jets are shown respectively. For each cut, the number of jets removed by it, is shown, including a relative number according to the original number of reco or truth jets respectively. The last two lines show the statistics for matching procedure including number of jets, which were (un)matched.

Appendix B

Unfolding Results

B.1 Matching Efficiencies

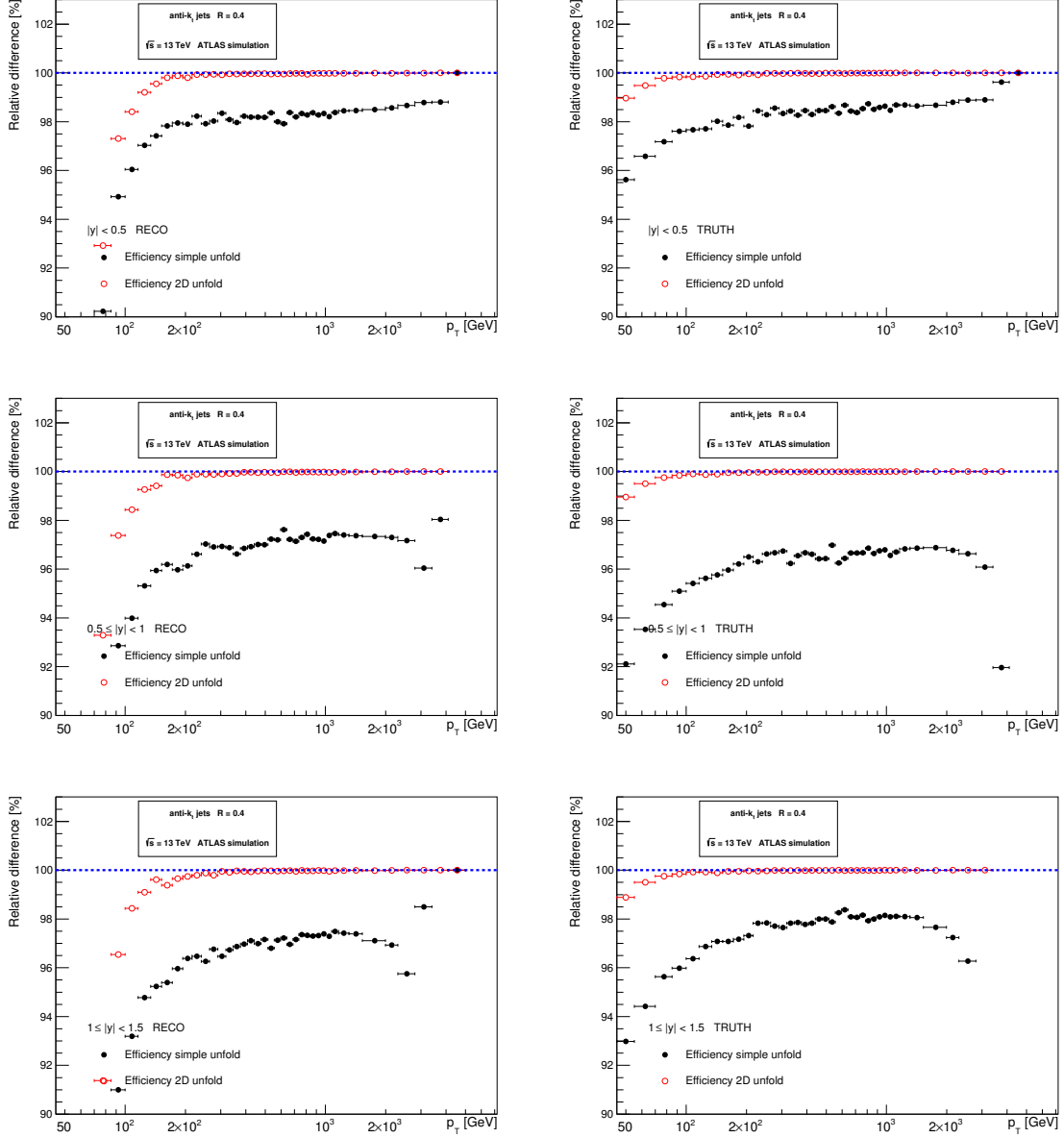


Figure B.1: Comparison of matching efficiencies of simple and 2D unfolding approaches for $|y| < 0.5$ (top), $0.5 \leq |y| < 1$ (middle) and $1 \leq |y| < 1.5$ (bottom) rapidity bins. Matching efficiencies are shown for reco (left) and truth jets (right) respectively.

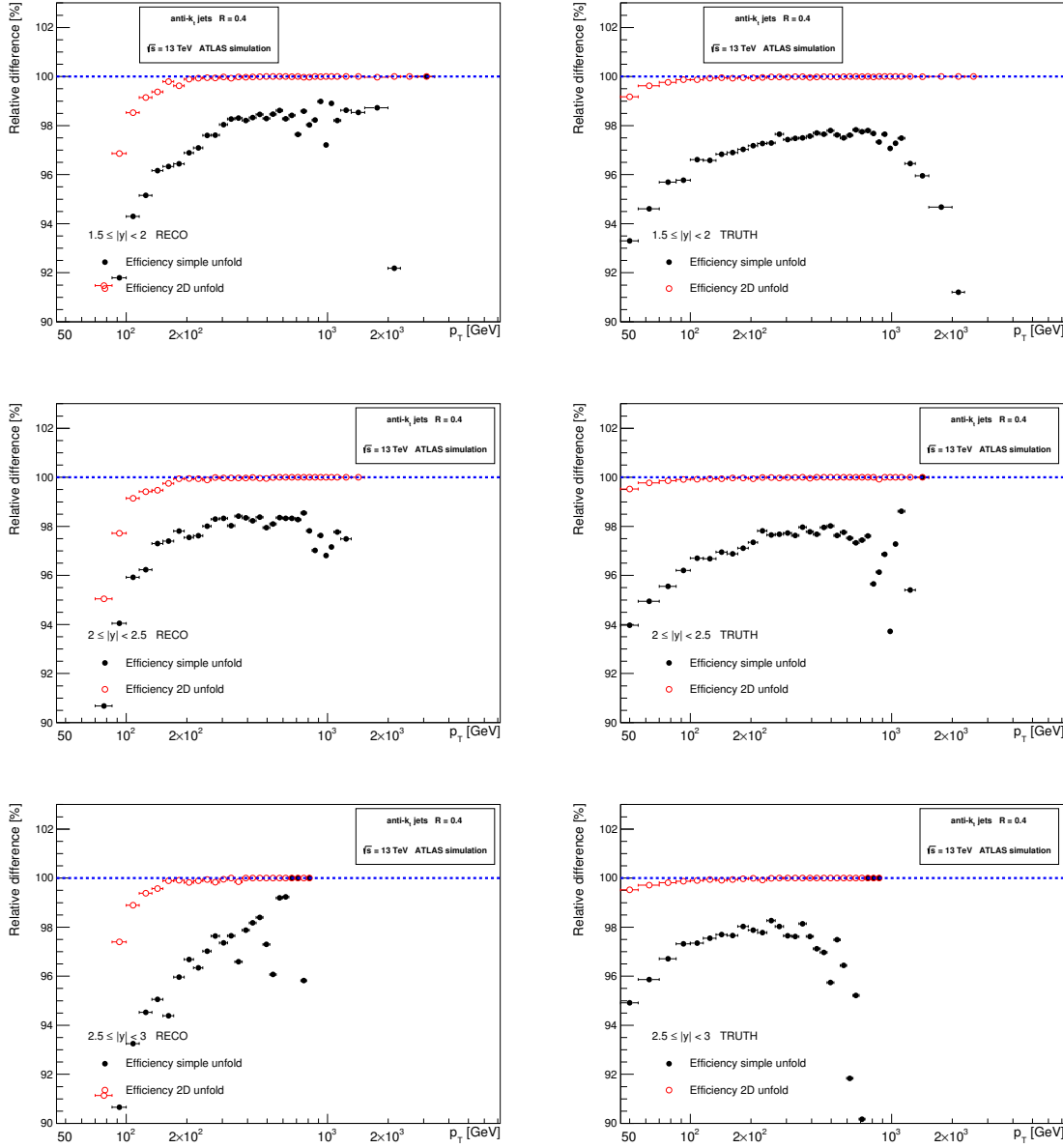


Figure B.2: Comparison of matching efficiencies of simple and 2D unfolding approaches for $1.5 \leq |y| < 2$ (top), $2 \leq |y| < 2.5$ (midle) and $2.5 \leq |y| < 3$ (bottom) rapidity bins. Matching efficiencies are shown for reco (left) and truth jets (right) respectively.

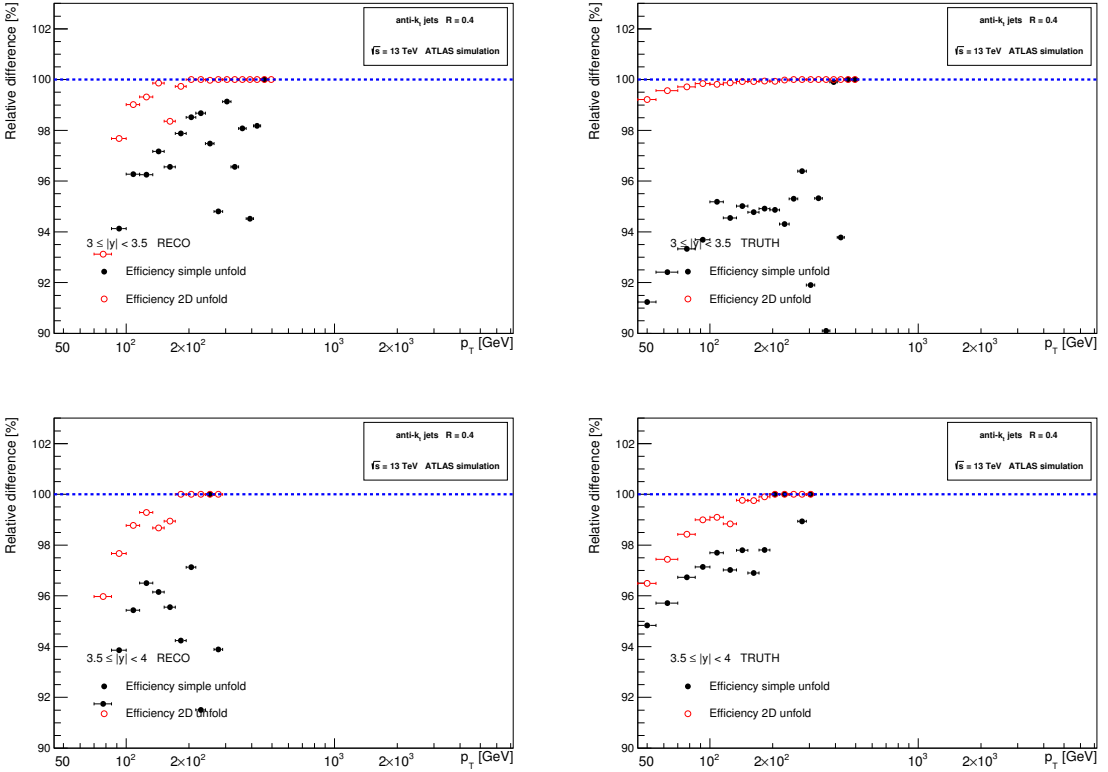


Figure B.3: Comparison of matching efficiencies of simple and 2D unfolding approaches for $3 \leq |y| < 3.5$ (top) and $3.5 \leq |y| < 4$ (bottom) rapidity bins. Matching efficiencies are shown for reco (left) and truth jets (right) respectively.

B.2 Slices in Unfolding Matrix

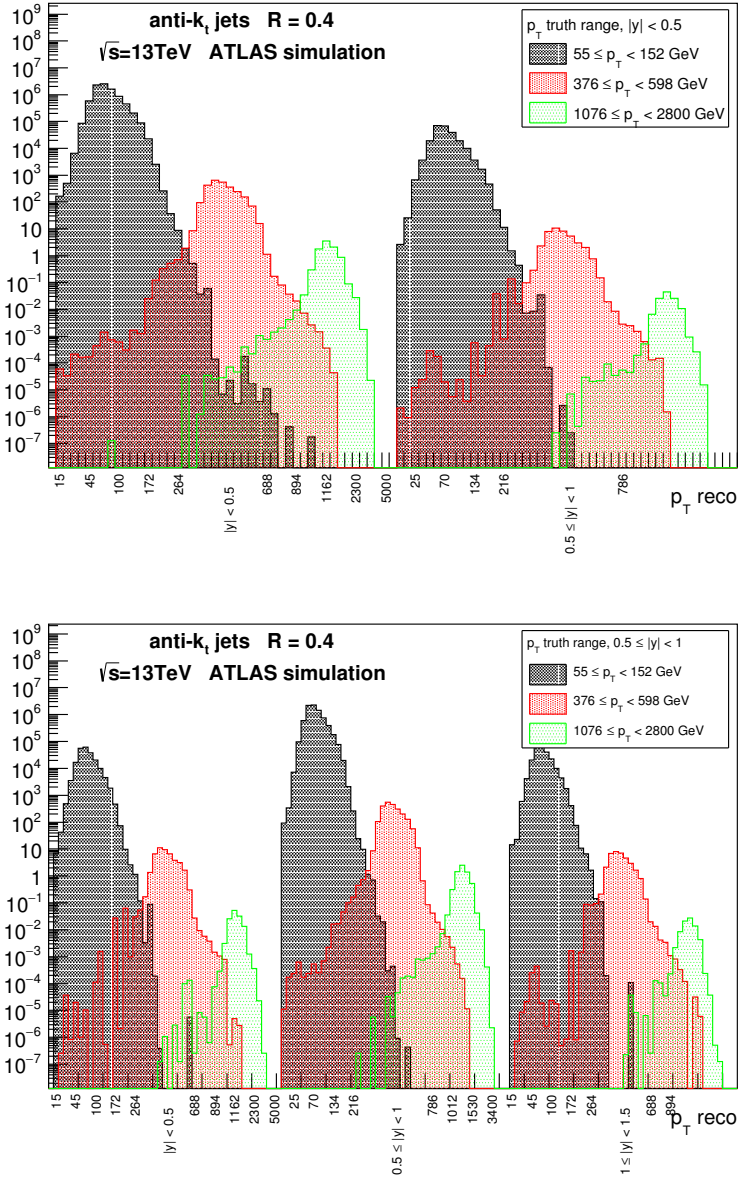


Figure B.4: Slices in the transfer matrix of 2D unfolding approach from Figure 3.3. Each histogram corresponds to the p_T spectrum of reco jets, which were matched with a truth jet with p_T and rapidity shown in the legend.

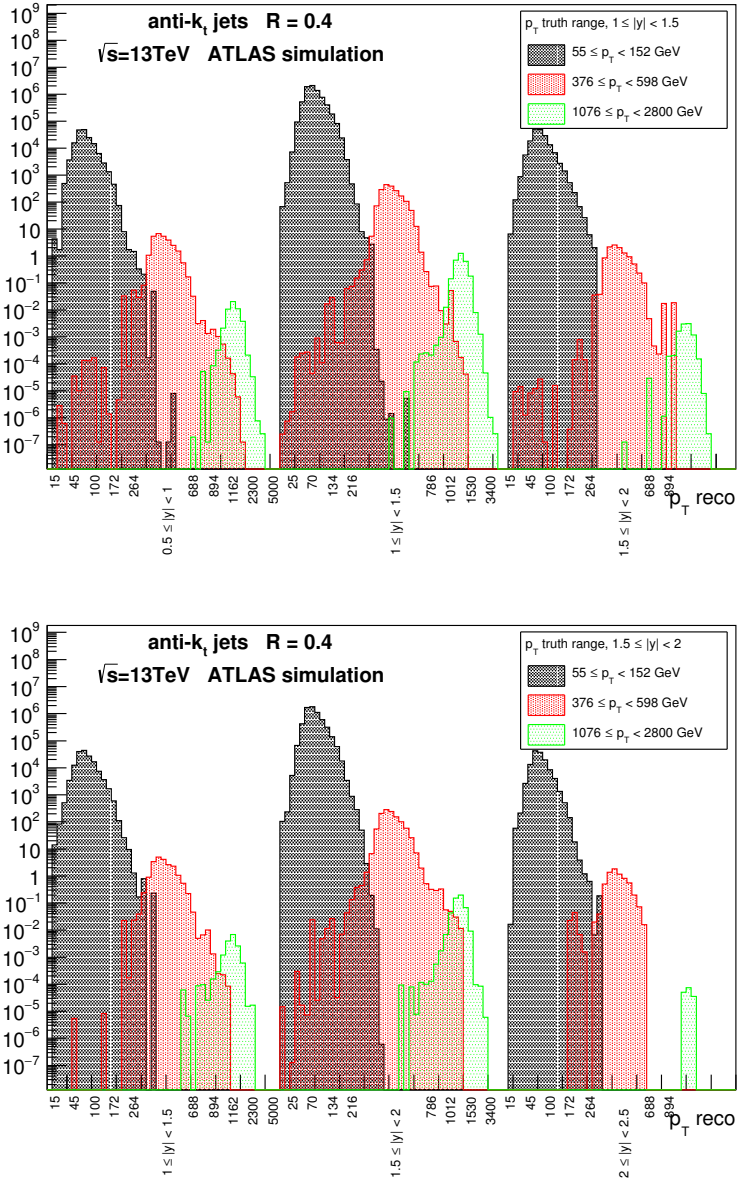


Figure B.5: Slices in the transfer matrix of 2D unfolding approach from Figure 3.3. Each histogram corresponds to the p_T spectrum of reco jets, which were matched with a truth jet with p_T and rapidity shown in the legend.

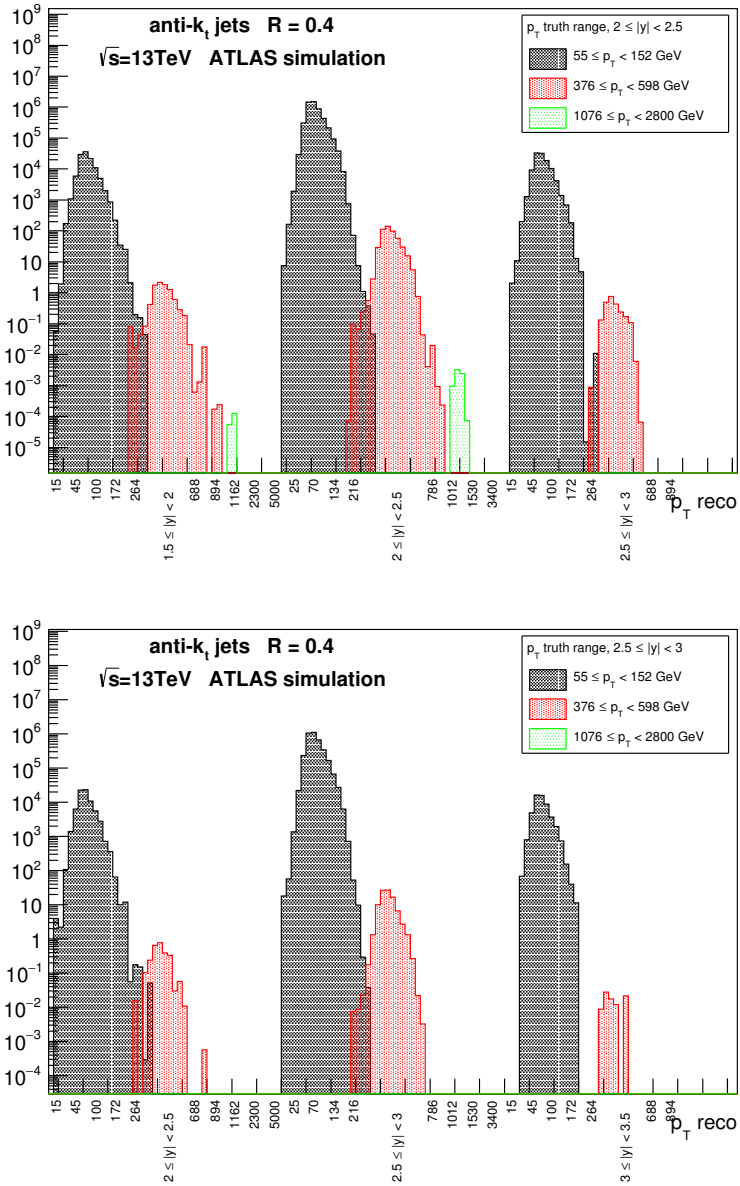


Figure B.6: Slices in the transfer matrix of 2D unfolding approach from Figure 3.3. Each histogram corresponds to the p_T spectrum of reco jets, which were matched with a truth jet with p_T and rapidity shown in the legend.

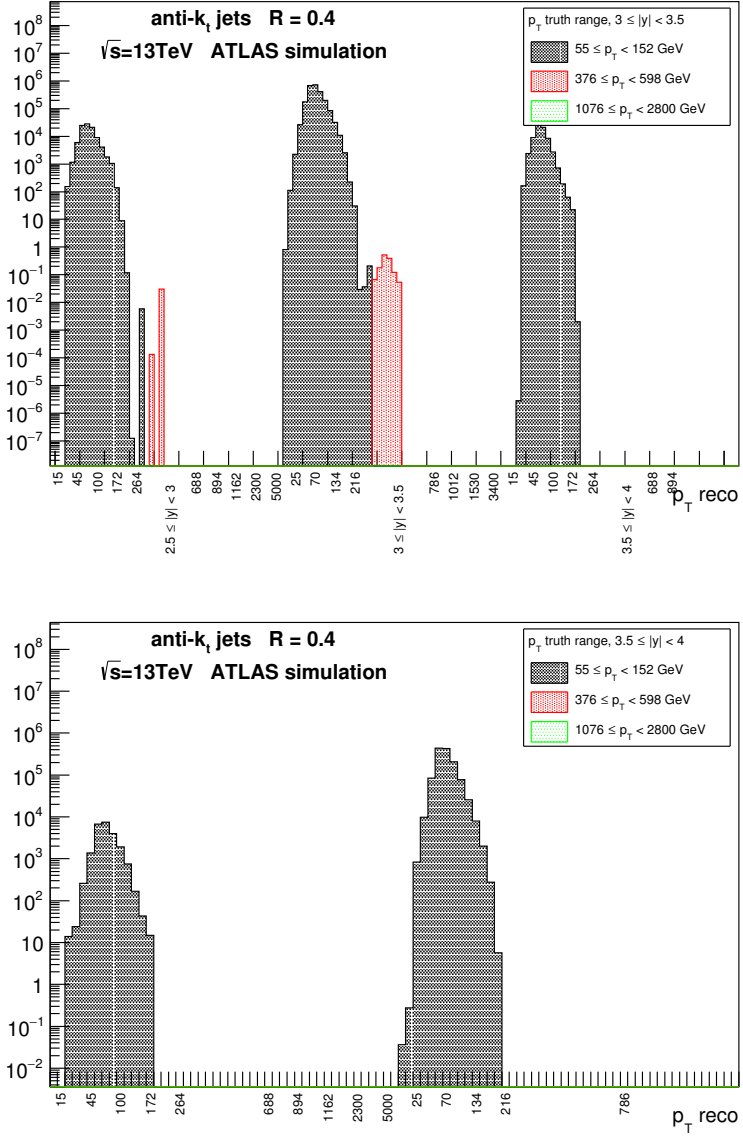


Figure B.7: Slices in the transfer matrix of 2D unfolding approach from Figure 3.3. Each histogram corresponds to the p_T spectrum of reco jets, which were matched with a truth jet with p_T and rapidity shown in the legend.

B.3 Unfolding of p_T Spectra

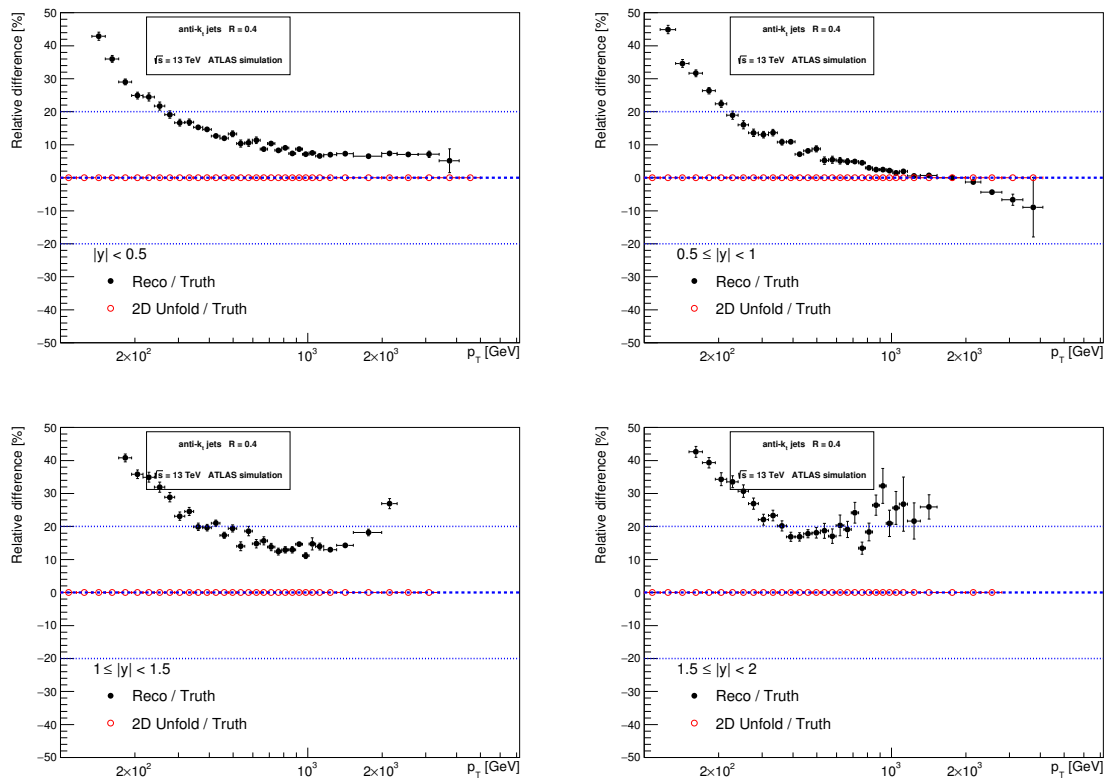


Figure B.8: Comparison of p_T spectra of reco jets (black) and the unfolded p_T spectra (using 2D unfolding approach, red) with the p_T spectra of the truth jets for the first four rapidity bins.

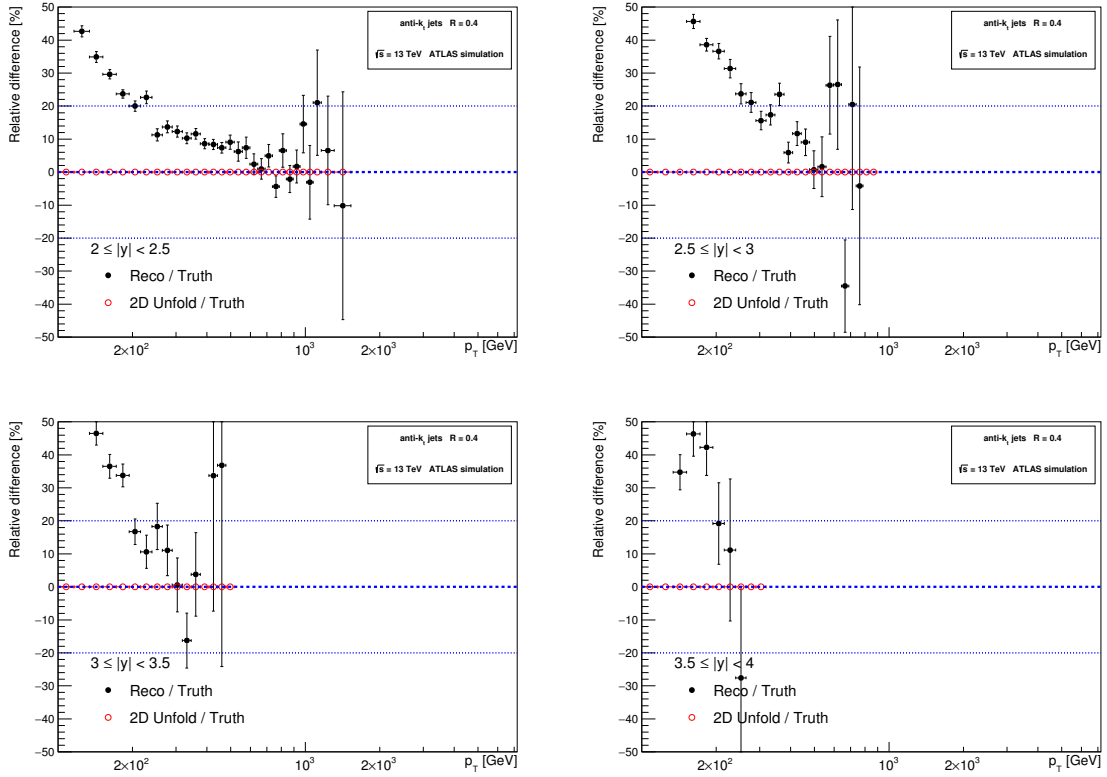


Figure B.9: Comparison of p_T spectra of reco jets (black) and the unfolded p_T spectra (2D unfolding approach, red) with the p_T spectra of the truth jets for the last four rapidity bins.

B.4 Simple and 2D Unfolding

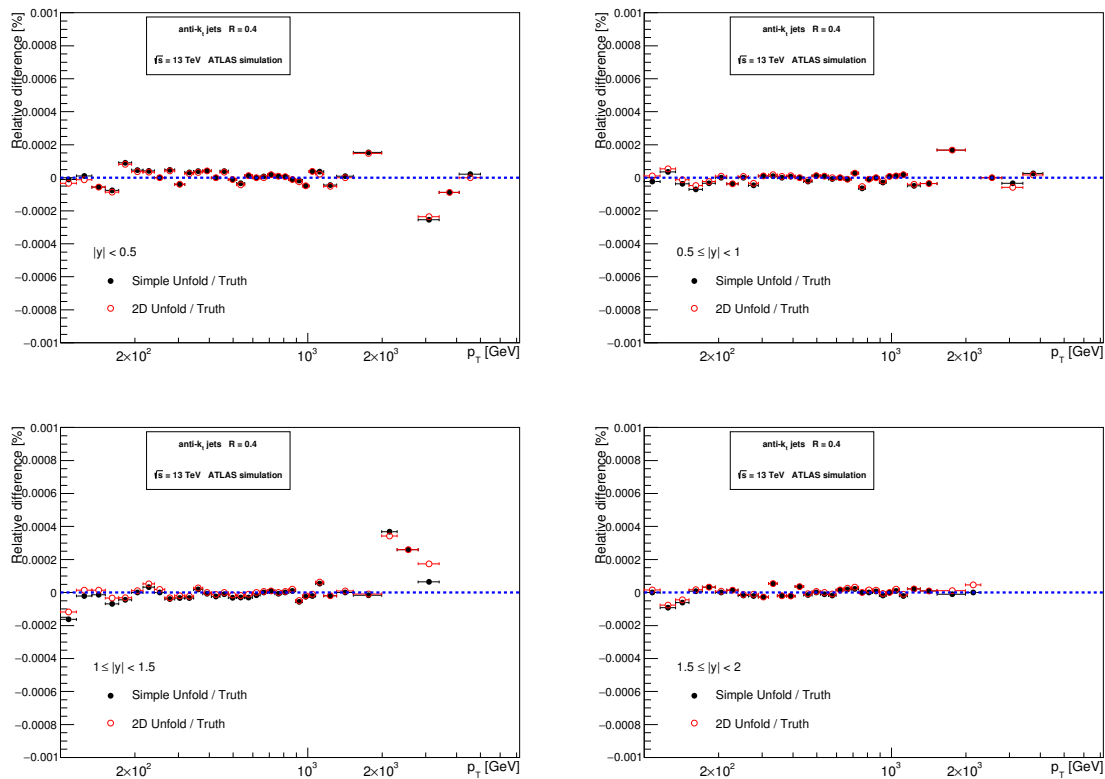


Figure B.10: Comparison of results obtained by two unfolding approaches, denoted as the simple and 2D unfold, with the p_T spectra of truth jets for the first four rapidity bins.

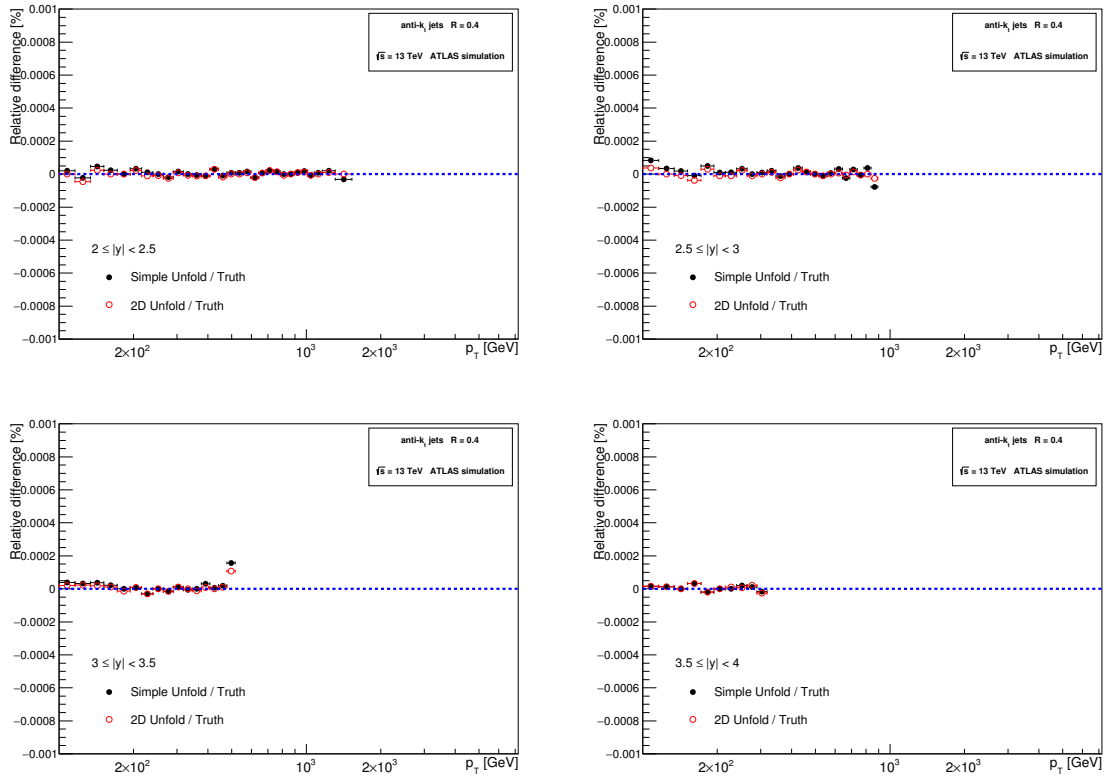


Figure B.11: Comparison of results obtained by two unfolding approaches, denoted as the simple and 2D unfold, with the p_T spectra of truth jets for the last four rapidity bins.

Appendix C

Next-to-Leading Order QCD Predictions

C.1 Predictions for Run I and Run II

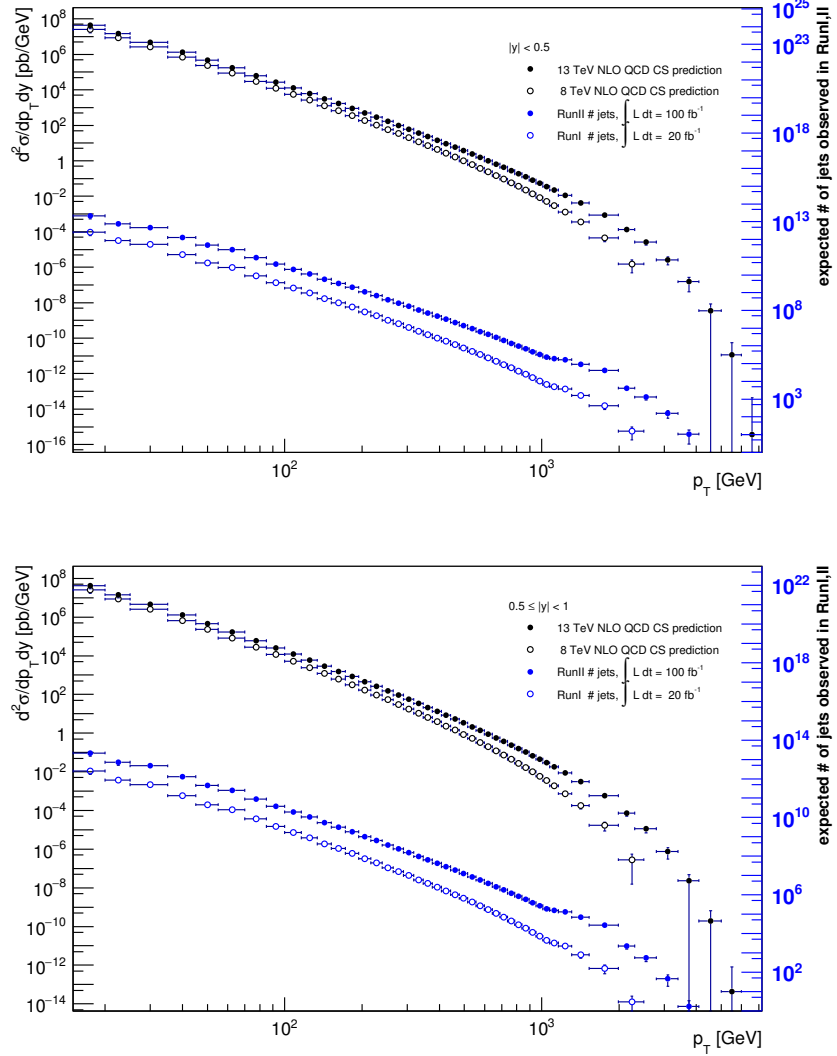


Figure C.1: Comparison of next-to-leading order QCD predictions of double differential inclusive jet cross section (black) in p_T and rapidity of proton-proton collisions at $\sqrt{s} = 13$ TeV (filled circles), corresponding to the LHC Run II, and $\sqrt{s} = 8$ TeV (empty circles), corresponding to the LHC Run I. The cross section is multiplied by integrated luminosities and p_T bin width to obtain expected number of jets observed in each p_T bin (blue). Figures show the comparison for $0.5 < |y|$ (top) and $0.5 \leq |y| < 1$ (bottom) rapidity bins.

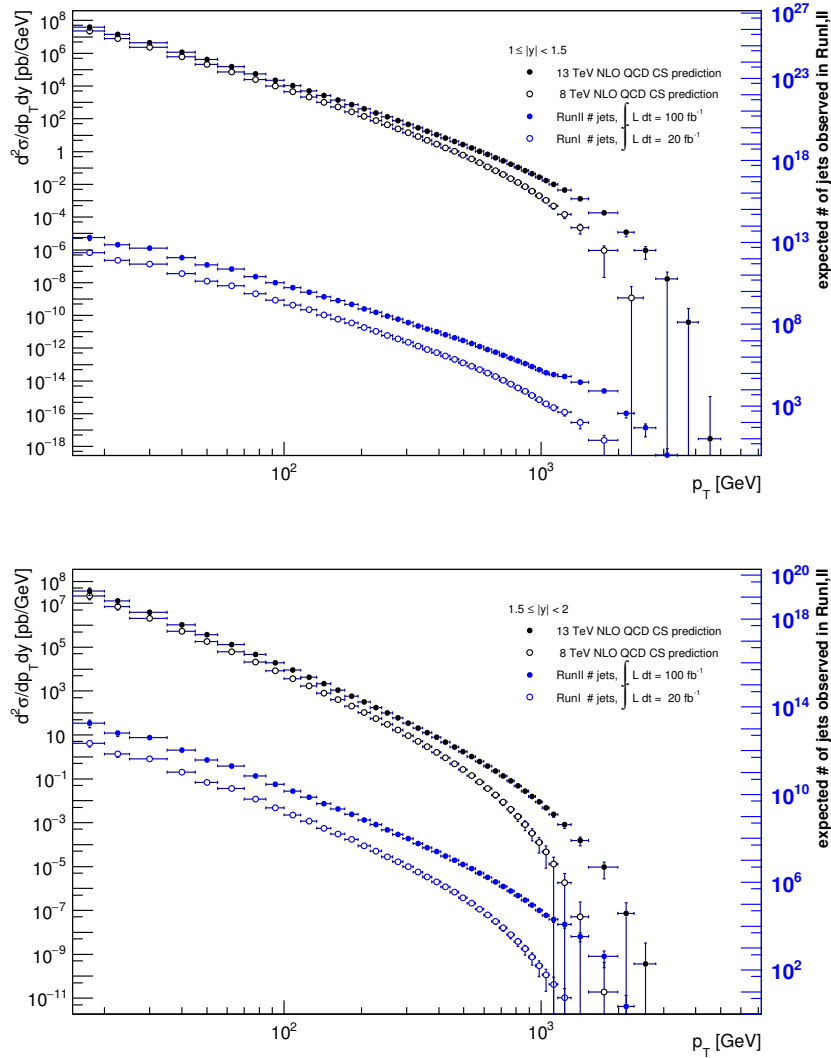


Figure C.2: Comparison of next-to-leading order QCD prediction of double differential inclusive jet cross section (black) in p_T and rapidity of proton-proton collisions at $\sqrt{s} = 13$ TeV (filled circles), corresponding to the LHC Run II and $\sqrt{s} = 8$ TeV (empty circles), corresponding to the LHC Run I. The cross section is multiplied by integrated luminosities and p_T bin width to obtain expected number of jets observed in each p_T bin (blue). Figures show the comparison for $1 \leq |y| < 1.5$ (top) and $1.5 \leq |y| < 2$ (bottom) rapidity bins.

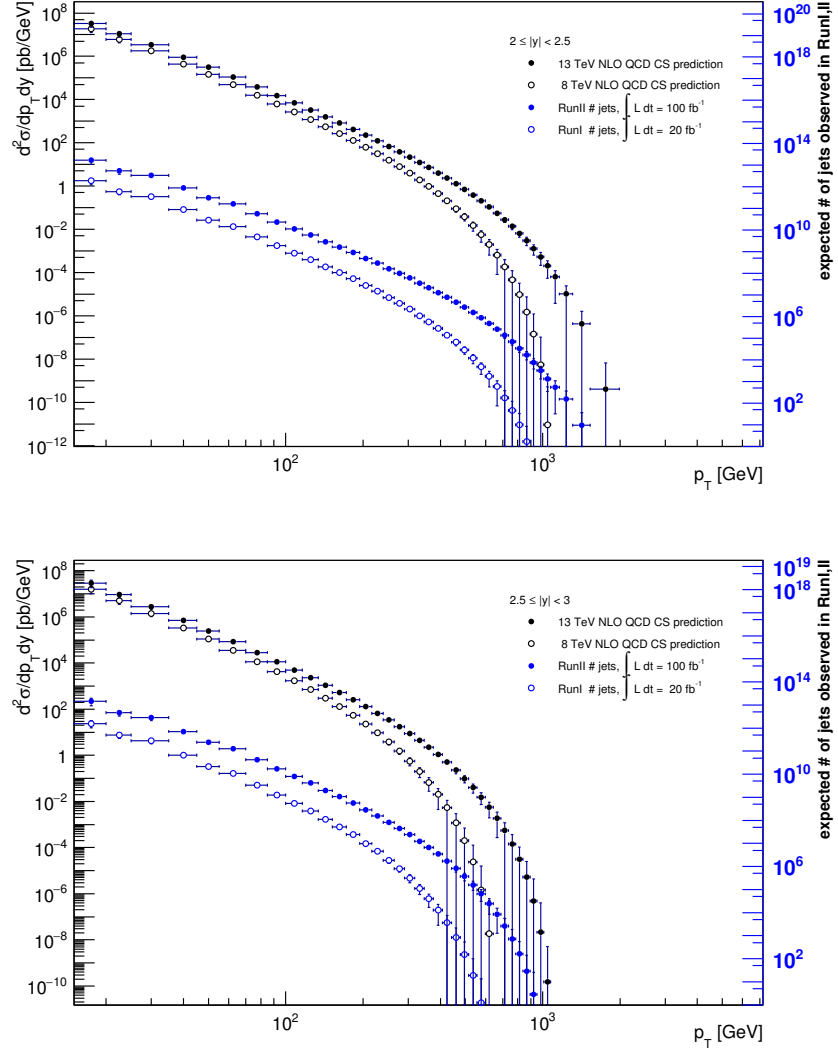


Figure C.3: Comparison of next-to-leading order QCD prediction of double differential inclusive jet cross section (black) in p_T and rapidity of proton-proton collisions at $\sqrt{s} = 13$ TeV (filled circles), corresponding to the LHC Run II and $\sqrt{s} = 8$ TeV (empty circles), corresponding to the LHC Run I. The cross section is multiplied by integrated luminosities and p_T bin width to obtain expected number of jets observed in each p_T bin (blue). Figures show the comparison for $2 \leq |y| < 2.5$ (top) and $2.5 \leq |y| < 3$ (bottom) rapidity bins.

C.2 Prediction Uncertainties

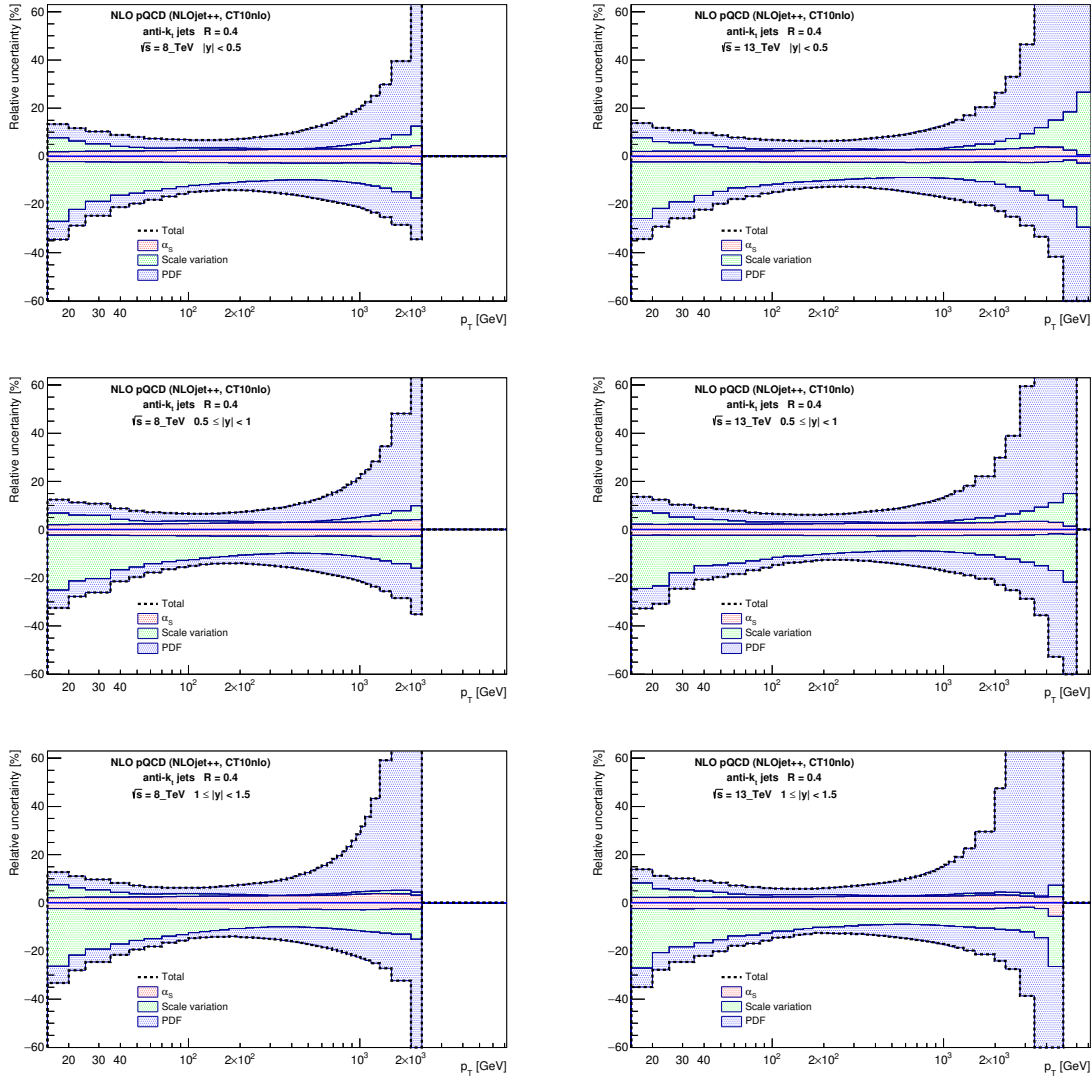


Figure C.4: Theoretical uncertainties for next-to-leading order QCD predictions of inclusive jet double differential cross section of proton-proton collisions at $\sqrt{s} = 8\text{ TeV}$ (left) and $\sqrt{s} = 13\text{ TeV}$ (right) for $|y| < 0.5$ (top), $0.5 \leq |y| < 1$ (middle) and $1 \leq |y| < 1.5$ (bottom) rapidity bins.

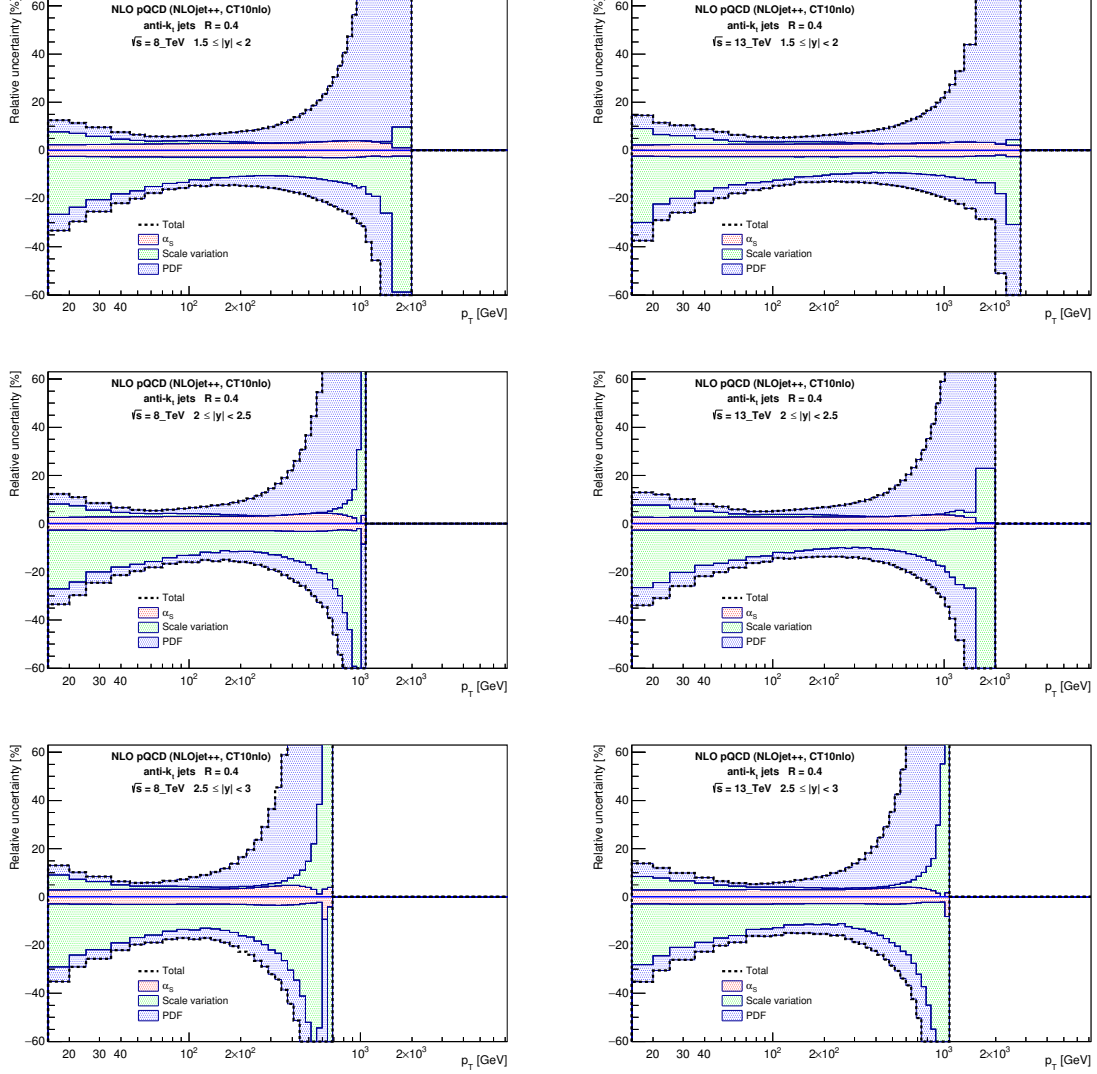


Figure C.5: Theoretical uncertainties for next-to-leading order QCD predictions of inclusive jet double differential cross section of proton-proton collisions at $\sqrt{s} = 8 \text{ TeV}$ (left) and $\sqrt{s} = 13 \text{ TeV}$ (right) for $1.5 \leq |y| < 2$ (top), $2 \leq |y| < 2.5$ (middle) and $2.5 \leq |y| < 3$ (bottom) rapidity bins.

C.3 Pythia and Next-to-Leading Order

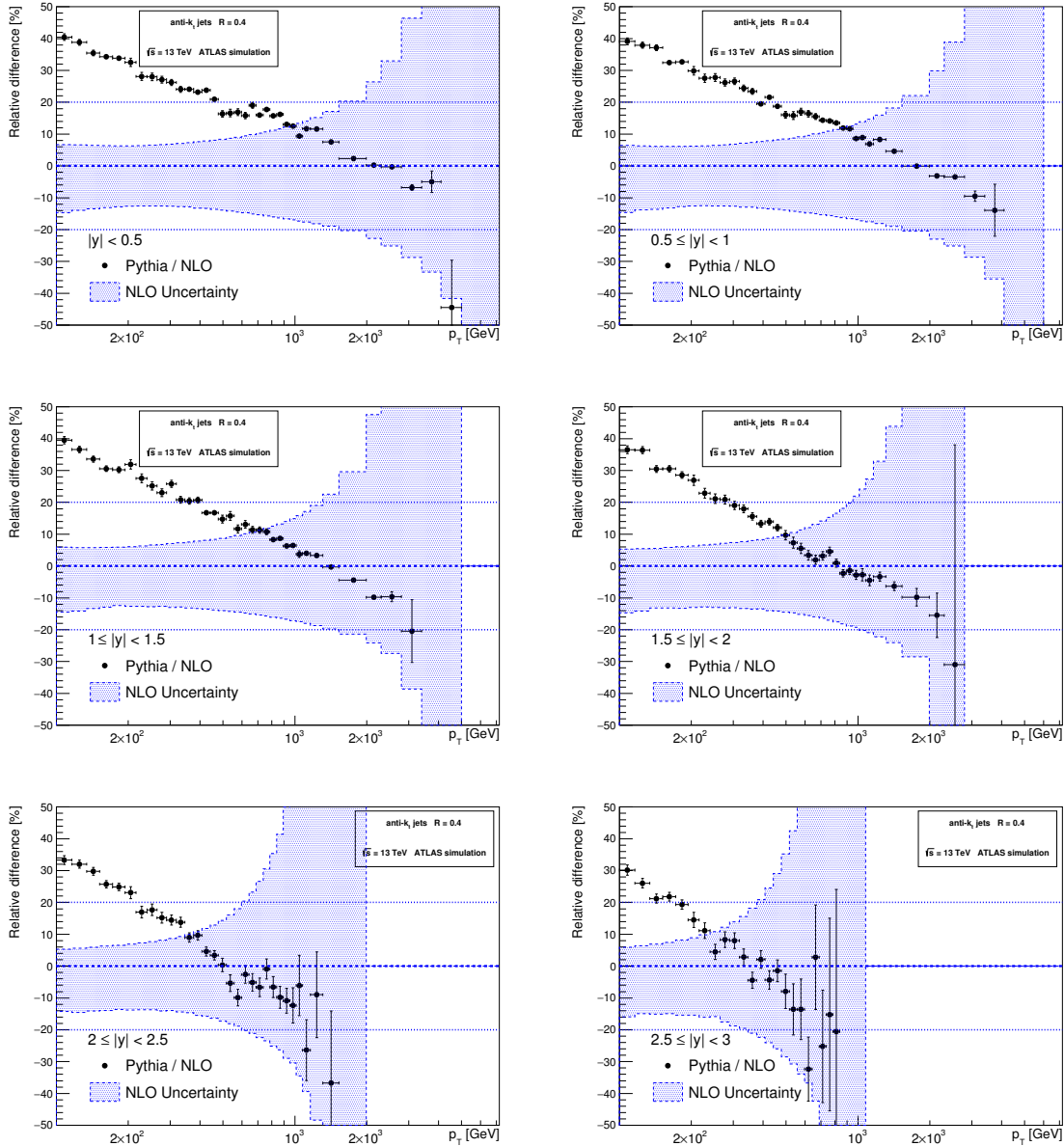


Figure C.6: Comparison of PYTHIA8 prediction with next-to-leading order QCD prediction of inclusive jet double differential cross section in p_T and rapidity for six different rapidity bins. Blue area represents the uncertainties of next-to-leading order QCD predictions, which are depicted in Appendix C.2 in detail.

Bibliography

- [1] S. Durr, “Lattice qcd for pedestrians.” http://www.physi.uni-heidelberg.de/Forschung/he/LHCb/documents/WorkshopNeckarzFeb13/durr_neckarzimmern.pdf, 2015. [Online; accessed 16-April-2015].
- [2] C. Colaboration, “Observation of top quark production in $\bar{p}p$ collisions with the collider detector at fermilab,” *Phys. Rev. Lett.*, vol. 74, pp. 2626–2631, Apr 1995.
- [3] D. Colaboration, “Search for high mass top quark production in $p\bar{p}$ collisions at $\sqrt{s} = 1.8$ tev,” *Phys. Rev. Lett.*, vol. 74, pp. 2422–2426, Mar 1995.
- [4] G. Aad *et al.*, “Observation of a new particle in the search for the Standard Model Higgs boson with the ATLAS detector at the LHC,” *Phys.Lett.*, vol. B716, pp. 1–29, 2012.
- [5] “Physics at run 2 the ultimate search engine: Lhc.” <http://indico.cern.ch/event/251191/session/0/material/slides/0?contribId=1>, 2015. [Online; accessed 14-April-2015].
- [6] “Standard model — Wikipedia, the free encyclopedia.” http://en.wikipedia.org/wiki/Standard_Model, 2015.
- [7] K. Olive *et al.*, “Review of Particle Physics,” *Chin.Phys.*, vol. C38, p. 090001, 2014.
- [8] W. Greiner, D. Bromley, S. Schramm, and E. Stein, *Quantum Chromodynamics*. Springer, 2007.
- [9] J. Horejsi, *Fundamentals of Electroweak Theory*. Karolinum Press, 2002.

- [10] D. Griffiths, *Introduction to Elementary Particles*. Physics textbook, Wiley, 2008.
- [11] W. Cottingham and D. Greenwood, *An Introduction to the Standard Model of Particle Physics*. Cambridge University Press, 2007.
- [12] T. Nakano and K. Nishijima, “Charge independence for v-particles,” *Progress of Theoretical Physics*, vol. 10, no. 5, pp. 581–582, 1953.
- [13] M. Gell-Mann, “The interpretation of the new particles as displaced charge multiplets,” *Il Nuovo Cimento*, vol. 4, no. 2, pp. 848–866, 1956.
- [14] M. Gell-Mann and Y. Ne’eman, *The eightfold way*. Frontiers in Physics, New York, NY: Benjamin, 1964.
- [15] G. Zweig, “An SU₃ model for strong interaction symmetry and its breaking; Version 2,” p. 80 p, Feb 1964.
- [16] H. Georgi, *Lie Algebras in Particle Physics: From Isospin to Unified Theories*. Frontiers in Physics Series, Westview Press, 1999.
- [17] “Eightfold way — Wikipedia, the free encyclopedia.” http://de.wikipedia.org/wiki/Eightfold_Way, 2015.
- [18] M. Gell-Mann and H. Fritzsch, *Murray Gell-Mann: selected papers*. World Scientific series in 20th century physics, Singapore: World Scientific, 2010.
- [19] S. Okubo, “Note on unitary symmetry in strong interactions,” *Progress of Theoretical Physics*, vol. 27, no. 5, pp. 949–966, 1962.
- [20] S. L. Glashow, J. Iliopoulos, and L. Maiani, “Weak interactions with lepton-hadron symmetry,” *Phys. Rev. D*, vol. 2, pp. 1285–1292, Oct 1970.
- [21] M. Kobayashi and T. Maskawa, “Cp-violation in the renormalizable theory of weak interaction,” *Progress of Theoretical Physics*, vol. 49, no. 2, pp. 652–657, 1973.
- [22] E. D. Bloom, D. H. Coward, H. DeStaebler, J. Drees, G. Miller, L. W. Mo, R. E. Taylor, M. Breidenbach, J. I. Friedman, G. C. Hartmann, and H. W. Kendall, “High-energy inelastic $e - p$ scattering at 6° and 10°,” *Phys. Rev. Lett.*, vol. 23, pp. 930–934, Oct 1969.

- [23] K. Olive *et al.*, “Review of Particle Physics,” *Chin.Phys.*, vol. C38, p. 090001, 2014.
- [24] C. N. Yang and R. L. Mills, “Conservation of isotopic spin and isotopic gauge invariance,” *Phys. Rev.*, vol. 96, pp. 191–195, 1954.
- [25] P. W. Higgs, “Broken symmetries and the masses of gauge bosons,” *Phys. Rev. Lett.*, vol. 13, pp. 508–509, Oct 1964.
- [26] L. Faddeev and V. Popov, “Feynman diagrams for the yang-mills field,” *Physics Letters B*, vol. 25, no. 1, pp. 29 – 30, 1967.
- [27] D. J. Gross and F. Wilczek, “Ultraviolet behavior of non-abelian gauge theories,” *Phys. Rev. Lett.*, vol. 30, pp. 1343–1346, Jun 1973.
- [28] M. Dordevic, “Standard Model physics results from ATLAS and CMS,” Tech. Rep. CMS-CR-2014-251, CERN, Geneva, Oct 2014.
- [29] “The history of qcd — cern courier.” <http://cerncourier.com/cws/article/cern/50796>, 2015.
- [30] R. Gupta, “Introduction to lattice QCD: Course,” pp. 83–219, 1997.
- [31] A. Ukawa, “Kenneth Wilson and lattice QCD,” 2015.
- [32] L. Evans and P. Bryant, “Lhc machine,” *Journal of Instrumentation*, vol. 3, no. 08, p. S08001, 2008.
- [33] G. Landsberg, “LHC: Past, Present, and Future,” 2013.
- [34] “Atlas experiment@2015 cern.” <http://www.atlas.ch/photos/index.html>, 2015.
- [35] R. Bruce, G. Arduini, S. Fartoukh, M. Giovannozzi, M. Lamont, *et al.*, “Baseline LHC machine parameters and configuration of the 2015 proton run,” 2014.
- [36] “Future prospects for higgs measurements at lhc run 2+3.” http://www.nikhef.nl/pub/BND2014/projects/ILC-vs-LHC-HL/LHC_Aspen_2014_Kroha.pdf, 2014.
- [37] T. A. Collaboration, “The atlas experiment at the cern large hadron collider,” *Journal of Instrumentation*, vol. 3, no. 08, p. S08003, 2008.

- [38] *Expected performance of the ATLAS experiment: detector, trigger and physics.* Geneva: CERN, 2009.
- [39] E. Halkiadakis, “Proceedings for TASI 2009 Summer School on ‘Physics of the Large and the Small’: Introduction to the LHC experiments,” 2010.
- [40] T. D. Lee and M. Nauenberg, “Degenerate systems and mass singularities,” *Phys. Rev.*, vol. 133, pp. B1549–B1562, Mar 1964.
- [41] T. Kinoshita, “Mass singularities of feynman amplitudes,” *Journal of Mathematical Physics*, vol. 3, no. 4, 1962.
- [42] G. Aad *et al.*, “Expected Performance of the ATLAS Experiment - Detector, Trigger and Physics,” 2009.
- [43] G. C. Blazey, J. R. Dittmann, S. D. Ellis, V. D. Elvira, K. Frame, *et al.*, “Run II jet physics,” pp. 47–77, 2000.
- [44] B. Isildak, “Measurement of the differential dijet production cross section in proton-proton collisions at $\sqrt{s} = 7$ tev,” 2013.
- [45] M. Cacciari, G. P. Salam, and G. Soyez, “The Anti-k(t) jet clustering algorithm,” *JHEP*, vol. 0804, p. 063, 2008.
- [46] T. Sjostrand, S. Mrenna, and P. Z. Skands, “A Brief Introduction to PYTHIA 8.1,” *Comput.Phys.Commun.*, vol. 178, pp. 852–867, 2008.
- [47] S. Agostinelli *et al.*, “GEANT4: A Simulation toolkit,” *Nucl.Instrum.Meth.*, vol. A506, pp. 250–303, 2003.
- [48] W. Lukas, “Fast Simulation for ATLAS: Atlfast-II and ISF,” 2012.
- [49] Z. Hubacek, “Measurement of the Three-jet Mass Cross Section in $p\bar{p}$ Collisions at $\sqrt{s} = 1.96$ TeV,” 2010.
- [50] J. Bossio, “Applyjetcalibration2014.” <https://twiki.cern.ch/twiki/bin/viewauth/AtlasProtected/ApplyJetCalibration2014>, 2015. [Online; accessed 16-April-2015].
- [51] V. Blobel, “Unfolding methods in high-energy physics experiments,” p. 40 p, Dec 1984.

- [52] G. D'Agostini, "Improved iterative Bayesian unfolding," *Phys.Rev.*, p. 31, 2010.
- [53] A. Hocker and V. Kartvelishvili, "SVD approach to data unfolding," *Nucl.Instrum.Meth.*, vol. A372, pp. 469–481, 1996.
- [54] B. Malaescu, "An Iterative, Dynamically Stabilized(IDS) Method of Data Unfolding," 2011.
- [55] H.-L. Lai, M. Guzzi, J. Huston, Z. Li, P. M. Nadolsky, *et al.*, "New parton distributions for collider physics," *Phys.Rev.*, vol. D82, p. 074024, 2010.
- [56] S. Wahrmund, "Atlas tunes for mpi." <http://indico.cern.ch/event/184925/session/4/contribution/19/material/slides/0.pdf>, 2015. [Online; accessed 16-April-2015].
- [57] T. Carli, E. Ertel, E. Fullana Torregrosa, A. Hrynevich, Z. Hubacek, B. Malaescu, N. Meric, C. Meyer, V. Pleskot, S. Shimizu, P. Starovoitov, G. Vardanyan, and S. Yanush, "Measurement of inclusive jet production in pp collisions at $\sqrt{s} = 7$ TeV using the ATLAS detector (Supporting Documentation)," Tech. Rep. ATL-COM-PHYS-2013-1390, CERN, Geneva, Oct 2013.
- [58] L. Harland-Lang, A. Martin, P. Motylinski, and R. Thorne, "Parton distributions in the LHC era: MMHT 2014 PDFs," 2014.
- [59] R. D. Ball *et al.*, "Parton distributions for the LHC Run II," 2014.
- [60] Z. Nagy, "Next-to-leading order calculation of three jet observables in hadron hadron collision," *Phys.Rev.*, vol. D68, p. 094002, 2003.
- [61] Z. Hubacek, "Atlas standard model workshop - lessons from run 1 and preparation for run 2." <https://indico.cern.ch/event/345914/session/2/contribution/26/material/slides/0.pdf>, 2015. [Online; accessed 22-April-2015].

